

IMPACTS OF Mn(II) ON Mn-OXIDE MINERALOGY AND TRACE METAL
SOLUBILITY AND SPECIATION IN REACTION SYSTEMS CONTAINING
BIRNESSITE

By

JOSHUA LEFKOWITZ

A Dissertation submitted to the Graduate School –Newark

Rutgers, The State University of New Jersey

in partial fulfillment of the requirements

for the degree of

Doctor of Philosophy

Graduate Program in

Environmental Science

Written under the direction of

DR. EVERT ELZINGA

and approved by

Newark, New Jersey

MAY 2016

ABSTRACT OF THE DISSERTATION

Impacts of Mn(II) on Mn-oxide mineralogy and trace metal solubility and
speciation in reaction systems containing birnessite

by

JOSHUA LEFKOWITZ

Dissertation Director

Dr. Evert Elzinga

This dissertation examines Mn(II)-birnessite interactions to improve understanding of the geochemical cycling of manganese, their influence on other elemental cycles, and the fate and solubility of trace metals through three studies that determined: (1) the influence of pH on Mn(II)-birnessite interactions under oxic and anoxic conditions, (2) how Zn(II) impacts Mn(II)-birnessite interactions, and (3) how Ni(II) impacts Mn(II)-birnessite interactions. UV-Vis spectroscopy and flame AAS were used in conjunction with XRD, XAS, ATR-FTIR and SEM to determine changes in solution chemistry concomitant with the reaction substrate in batch sorption experiments. Birnessite reacted at $\text{pH} < 7.0$ exhibited no bulk mineralogical transformation products. At $\text{pH} 7.0\text{-}8.5$, reaction with Mn(II) under anoxic conditions caused reductive transformation of birnessite into different end products contingent upon pH, the concentration of Mn(II) and/or the

presence of either Zn(II) or Ni(II). For binary Mn(II)-birnessite systems, formation of feitknechtite (β -MnOOH) and manganite (γ -MnOOH) were observed at pH 7-8. At pH 8.0-8.5, Mn(II)-birnessite interactions produced hausmannite (Mn_3O_4). In oxic systems, reductive transformation of birnessite is complemented by surface catalyzed oxidation of Mn(II) by O_2 .

Mn(II) was found to compete for sorption sites with Zn(II) at pH 6.5. At pH 7.5, Zn(II) and Mn(II) sorption were observed to be enhanced relative to the corresponding experiments where only one aqueous divalent metal was present. The speciation of Zn(II) was different than at pH 6.5 and XAS results in combination with XRD data demonstrate formation of spinel $\text{Zn(II)}_{1-x}\text{Mn(II)}_x\text{Mn(III)}_2\text{O}_4$.

When Mn(II) is present in systems containing Ni(II)-birnessite at pH 6.5, Ni(II) edge-sharing surface complexes form. At pH 7.5, Mn(II) has a distinct impact on Ni(II) speciation. Transformation of Ni(II)-birnessite, following introduction of Mn(II), to a feitknechtite-like phase containing Ni(II) was evident by XRD and ATR-FTIR analyses; further conversion to manganite was inhibited. XAS, FTIR, and XRD analyses suggest that Ni(II) is incorporated into the feitknechtite-like structure.

The results of this dissertation suggest that aqueous Mn(II) is an important control on the mineralogy and reactivity of natural Mn-oxides, as well as the fate and solubility of trace metals, particularly in aqueous geochemical environments with neutral to alkaline pH values.

Acknowledgments

I would like to thank the support of my thesis advisor, Dr. Evert Elzinga, as well as my dissertation committee members, Dr. Lisa Axe, Dr. Kristina Keating, and Dr. Dimitrios Ntarlagiannis. I would also like to thank other supportive faculty, including Drs. Alexander Gates, Lee Slater, Yuan Gao, Andreas Vassiliou, and Karina Schafer, as well as staff members, including Liz Morrin, Lucille Foster and Sweeta Chauhun. Thank you to my fellow (past and present) students and colleagues at Rutgers University and in the Department of Earth and Environmental Sciences. Special thanks to Ying Zhu, my labmate, colleague and friend. Special thanks to Ashley New, my labmate, colleague and friend, who knows all too well the struggles we faced.

I am thankful for all of the people who helped me along on this long journey, especially to all of my family whose support was an integral part of my perseverance. To that end, I would like to especially thank Cameron for her dedication, love, patience and for being so Californian rad. Thank you to our awesome, wonderful, beautiful, handsome, whimsical, mischievous, and delightful son, Dune, whose smiles, laughter, nuzzles and snuggles kept me, and us, going. Thank you to Dune's godmother, Lara Haddad, for her tireless enthusiasm and wild gesticulations. Thank you to my parents, Alan and Beverly for their intrepid encouragement. Thank you to my brothers Jon, James, Ken and Abdul, and my sisters Jill and Camille for their enduring backing and humor. Thank you to my amazingly imaginative, brilliant and fun-loving nephews Kailen, Elijah, Cassiel, Idris and Ihsan. Thank you to all of my cousins, Susan, Danny, Eve, Bruce, Doria, Rebecca, David and Kristen Bachenheimer for their continuous support throughout my life. Thank you to my cousin Dr. Paul Lefcourt whose advice to skip grad school and become a beach bum I

probably should have followed. Thank you Dr. Yolande Marlow, who reminded me that it's not the number of times you get knocked down that matters, but that you pick yourself up every time. Without the support of all of these people, I would not have completed this degree. I would also like to thank my friends and colleagues who helped me persevere over all these years. A very special and heartfelt thanks to Dr. Ksenija Grcacs, a stalwart friend, colleague and champion who never let me quit. A very special and heartfelt thanks to Dr. Andrej Grubisic for his steady support and level-headed advice. Thank you to my dear friends, Victor De La Paz, Carlos Varas and Mathew Fury who have always supported me without question. And a final, special thanks to Isabelle Lassez, international citizen, champion of peace and human rights and survivor of The Great Bug Infestation of 2013.

While the road to a PhD is one less travelled upon by the general population, the individuals who make the journey know it to be one that is comprised of Sisyphean footsteps which seem to tread endlessly across a bridge to nowhere with numerous Goblin toll collectors and Kafkaesque tasks to divert your direction towards other digressions until you one day find yourself somewhere.

Chapter 1:

This work was supported by start-up funds from Rutgers University to E.J.E as well as the National Science Foundation GK-12 Fellowship. We thank Kumi Pandya (beamline X11A, NSLS) for support during EXAFS data acquisition, and three anonymous reviewers whose comments helped improve this paper.

Chapter 2:

Funding for this work was provided by the New Jersey Water Resources Research Institute. Use of the Bruker D8 Advance X- ray diffractometer at Rutgers-Newark was supported by the NSF through award EAR-1337450. We thank the beamline scientists at NSLS beamline X11A and APS beamline 12BMB-B for assistance during XAS data acquisition. The comments from five anonymous reviewers helped improve this paper.

TABLE OF CONTENTS

Chapter 1: Introduction	1
1.1 Background and overview	1
1.1.1 Significance of microbially mediated oxidation of Mn(II) in redox cycling	1
1.1.2 Birnessite as a primary manganese oxide, natural sorbent and oxidant	3
1.1.3 Role of Mn(II) in secondary transformation pathways	6
1.2 Hypotheses	9
1.3 Organization of the Thesis.....	9
1.4 Acknowledgment of Previous Publications	9
Chapter 2: Influence of pH on the reductive transformation of birnessite by Mn(II)	11
Abstract.....	11
2.1 Introduction.....	11
2.2 Materials and Methods	14
2.2.1 Mn-Oxide Substrates	14
2.2.2 Mn(II)–Birnessite Isotherm Experiments.	14
2.2.3 Spectroscopic Analyses of Mn-Oxide Sorption Products	15
2.3 Results and Discussion	16
2.3.1 Mn(II)–Birnessite Sorption Isotherms.....	16
2.3.2 XRD, XAS, and IR Results of Mn-Oxide Sorption Products.....	17
2.4 Environmental Implications.....	27
2.5 Figures	29
Chapter 3: Impacts of aqueous Mn(II) on the sorption of Zn(II) by hexagonal birnessite...35	
Abstract.....	35
3.1 Introduction.....	36
3.2 Materials and Methods	38
3.2.1. Mn-oxide substrates.....	38
3.2.2. Batch sorption experiments.....	38
3.2.3. Solids analyses	40
3.3. Results and Discussion	42
3.3.1. Sorption isotherms	42
3.3.2. Sorption kinetics.....	43

3.3.3. EXAFS and powder XRD data	45
3.4. Environmental Implications	51
3.5. Figures	53
Chapter 4: Impact of Mn(II)-driven transformation of Ni(II) sorbed birnessite	58
Abstract	58
4.1 Introduction	59
4.2 Materials and Methods	61
4.2.1 Experimental Conditions	61
4.2.2 Experimental protocols to ensure anoxic conditions	61
4.2.3 Synthesis of Mn-oxide substrates	61
4.2.4 Batch sorption experiments	62
4.2.5 Analysis of solid materials	65
4.3 Results and Discussion	68
4.3.1 Batch kinetic studies	68
4.3.2 XRD and ATR-FTIR results	70
4.4 Environmental Implications	78
Chapter 5: Conclusions	85
5.1. General Conclusions	85
5.1. Environmental Significance	87
5.2. Future Research	89
References	91
Appendices	106
Appendix 1: Supporting Information for Chapter 2	106
A1.1 Synthesis and characterization of Mn-oxide substrates	106
A1.2 Spectroscopic analyses of Mn-oxide sorption products	106
A1.3 Protocols to ensure anoxic conditions during the experiments Anoxic	108
A1.4 ATR-FTIR results of anoxic Mn(II)-birnessite isotherm samples	108
A1.5. Scanning electron microscopy (SEM) images of reacted Mn-oxide solids	108
A1.6. Results from linear combination fits of k^3 -weighted χ data of Mn-oxide solids	109
A1.7. Mn(II)-birnessite kinetic sorption experiments	110
A1.8 Supporting Information Figures	112

A1.9 Tables for Chapter 2	117
Appendix 2: Supporting Information for Chapter 3.....	118
A2.1. Synthesis of Mn-oxide substrates.....	118
A2.2. Experimental protocols to ensure anoxic conditions	119
A2.3. XAS data analyses.....	119
A2.4. Shell-by-shell fits of Zn K-edge EXAFS data	120
A2.5. Single-shell fits.....	121
A2.6. Two-shell fits.....	123
A2.7. Linear combination fits.....	125
A2.8. Linear combination fits for the pH 7.5 ternary kinetic experiment	125
A2.9 XAS data of samples reacted at various values of pH, [Mn(II)] and [Zn(II)]	126
A2.10. Supporting Information Figures.....	130
Table A2.S2. Numerical results of LC fits from Figure 3.4.....	137
Appendix 3	139
A3.1 Powder XRD of samples obtained from binary and ternary experiments	139
A3.2. Time dependent formation of Ni(II) substituted feitknechtite by XAS.....	140
A3.3 Supporting Information Figures.....	144
A3.4 Supporting Information Tables	149

LIST OF TABLES

Table A1.S1: Summary of the quantitative LC fit results of the k^3 -weighted χ data.	117
Table A2.S1: Shell-by-shell fits of Zn XAS data.	136
Table A2.S2. Numerical results of LC fits from Figure 3.3.	138
Table A2.S3: Numerical results from LC fits presented in Figure A2.S2.....	149
Table A3.S1: Shell fit results of Ni XAS data from sorption products and references. .	149

LIST OF FIGURES

Figure 2.1. Macroscopic results of Mn(II)-birnessite isotherm experiments.....	29
Figure 2.2. XRD results for sorption samples from pH 5.5-8.5.	30
Figure 2.3. Results from linear combination fits.	31
Figure 2.4. Thermodynamic stability plot: feitknechtite, manganite and hausmannite....	32
Figure 2.5. Macroscopic results for anoxic and oxic sorption isotherms at pH 6-8.	33
Figure 2.6. ATR-FTIR results.....	34
Figure 3.1. Macroscopic results from anoxic metal(II)-birnessite isotherms at pH 7.5. ..	53
Figure 3.2. Time dependent removal of Mn(II) in binary and ternary experiments.	54
Figure 3.3. Time dependent removal of Ni(II) in binary and ternary experiments.	55
Figure 3.4. Zn K-edge data of Zn(II)-Mn(II)-birnessite sorption samples.	56
Figure 3.5. X-ray powder diffraction: Mn ₃ O ₄ , ZnMn ₂ O ₄ and ternary sorption product...	57
Figure 4.1 Time dependent removal of Mn(II) in binary and ternary experiments.....	80
Figure 4.2 Time dependent removal of Ni(II) in binary and ternary experiments.	81
Figure 4.3 XRD patterns of sorption samples from binary and ternary experiments.	82
Figure 4.4 ATR-FTIR spectra of samples from binary and ternary experiments.....	83
Figure 4.5 Ni K edge EXAFS data from samples from binary and ternary experiments..	84
Figure A1.S1. ATR-FTIR spectra of anoxic Mn(II)-birnessite samples at pH 7.0-8.5. .	112
Figure A1.S2. SEM images of selected sorption samples and Mn oxides.	113
Figure A1.S3. Extended X-ray Absorption Fine Structure data of samples at pH 7-8...	114
Figure A1.S4. Time-dependent removal of Mn(II) at pH 8.5.....	115
Figure A1.S5. ATR-FTIR data of pH 8.5 sorption samples	116
Figure A2.S1 Linear combination fit results.....	130

Figure A2.S2. Zn <i>K</i> edge EXAFS data.	131
Figure A2.S3. Linear combination fit estimates	132
Figure A2.S4. Linear combination fit results.....	133
Figure A2.S5. ATR-FTIR data	134
Figure A2.S6. X-ray diffraction data of sorption samples.....	135
Figure A3.S1. Mn(II)-birnessite ATR-FTIR data at pH 7.5.	145
Figure A3.S2. XRD patterns from ternary sorption samples as a function of time.	145
Figure A3.S3. XRD comparison of feitknechtite and Ni(II) substituted feitknechtite. ..	146
Figure A3.S4. EXAFS data showing evolution of Ni(II) substituted feitknechtite.	147
Figure A3.S5. EXAFS data showing impact of buffer in these systems.	148

Chapter 1: Introduction

1.1 Background and overview

1.1.1 Significance of microbially mediated oxidation of Mn(II) in redox cycling

The manganese (Mn) redox cycle is of major geochemical and environmental significance due to its strong influence on other elemental cycles and the complexity of the reaction pathways involved. In general, this cycle may be understood as the reversible interconversion between different Mn oxidation states driven by thermodynamically favorable electron exchange reactions with major elements such as oxygen, carbon, sulfur and nitrogen¹⁻⁵ as well as those of trace elements including As,⁶⁻⁸ Cr,⁸ and Se.^{9,10} Manganese redox cycling has a major impact on Mn solubility; the Mn(II) form, which dominates under acidic and reducing conditions, is relatively soluble; the Mn(III) and Mn(IV) forms, favored at both high Eh and pH, are highly insoluble and form a wide variety of Mn(III,IV)-(oxyhydr)oxide phases (referred to as MnO_x), with more than 30 such minerals currently identified.¹¹

A classic example of a geochemical system where Mn redox cycling occurs is represented by the redoxclines in stratified lake and marine environments, where aqueous Mn(II) is produced from the reduction of Mn(III, IV)-oxides in the anoxic zone of the environmental milieu.¹² Mn(II) diffuses into the water column until it reaches the oxic zone where re-oxidation occurs and, consequently, insoluble colloidal Mn(IV)O₂ forms and settles back into the anoxic zone to complete the loop. While the general redox framework of Mn is well described, the pathways of Mn oxidation and reduction require further research. These pathways include complex interconversion between the various

mineral and aqueous forms, modulated by environmental factors (pH, complexing ligands, etc.) and microbial activity.

In the “oxidative arm” of the Mn cycle, Mn(II) is oxidized to insoluble Mn(III) and Mn(IV). Oxidation of Mn(II) by molecular oxygen (O_2) is thermodynamically favorable but kinetically very slow, with a reported rate of 6-7 years for homogeneous solutions.¹³ In natural systems, the rate of oxidation may be significantly increased by physicochemical and biologically mediated processes. Adsorption of Mn(II) at mineral surfaces, including Mn(III,IV)-oxide colloids, facilitates autocatalytic oxidation of Mn(II) by O_2 , enhancing the rate by nearly one order of magnitude above pH 8.¹⁴

It is now generally accepted, particularly based on research performed over the past two decades, that oxidation of Mn(II) in natural systems is driven primarily by biological activity.^{15–24} Microbes and fungi catalyze the oxidation of Mn(II) by O_2 , using the energy yield (resulting from the favorable thermodynamics) to power their metabolic systems. Microbes have been shown to catalyze Mn(II) oxidation 5-6 orders of magnitude faster than the calculated value for autocatalytic oxidation on the surface of colloidal MnO_2 .^{20,21} Accordingly, natural Mn(II) oxidation primarily involves a bio-redox pathway wherein Mn(II) is oxidized to insoluble Mn(IV) without appreciable accumulation of intermediate Mn(III).²⁰ This finding establishes the critical notion that the majority of MnO_x are of biological origin, produced either directly via microbial oxidation of Mn(II) or by subsequent alteration of biogenic Mn(III, IV)-oxides.²² While biological oxidation of Mn(II) had been recognized for some time^{15,17,25}, it has only relatively recently been recognized as the primary driving force of Mn(II) oxidation in natural systems (including marine and terrestrial environments). Prior to this consensus

view, much of the older work focused on the abiotic oxidation of Mn(II) by O₂.^{13,26–29} The novel recognition of biogenic Mn-oxides as the primary source of oxidized Mn(III) and Mn(IV) has led to new consideration of the pathways and mineral products involved in natural Mn redox cycling.

The predominance of biogenic hexagonal birnessite-type minerals in marine and terrestrial environments makes these minerals an important starting point for understanding the “reductive arm” of biogeochemical Mn redox cycling, where high valence Mn(IV) is reduced to lower valence Mn(III) and Mn(II) forms through a variety of pathways. In aqueous environments, structural Mn(IV) in MnO_x can oxidize ferrous iron (Fe(II)), producing lower valence Mn forms.^{30,31} Additional reductants of MnO_x in marine environments include ammonium (NH₄⁺) and sulfide (HS⁻), which may reduce Mn(IV)-oxides in oxygen-depleted waters.^{2–4,32} Natural organic matter (NOM), such as humic and fulvic acids, may also cause reductive dissolution of MnO_x,³³ and may further enhance Mn mobility via ligand-assisted dissolution.^{34–38} The reductive dissolution of birnessite by NOM diminishes the sorptive capacity of the mineral by decreasing the number of sites directly, and via the generation of Mn(II) which may subsequently sorb to the surface.³⁹ Light and pH can also influence reactions involving Mn(IV)⁴⁰ as observed for the reductive dissolution of colloidal Mn by fulvic acid.³³ In the euphotic zone of natural waters photoreductive dissolution is a principal process where Mn(IV) cation vacancies enhance the photochemical reactivity.⁴¹

1.1.2 Birnessite as a primary manganese oxide, natural sorbent and oxidant

Hexagonal birnessite is a major manganese oxide in natural aquatic systems.⁴² This phyllomanganate is characterized by variable unit cell symmetry, poorly ordered sheet

stacking, and low crystallinity.⁴³ Recent studies have demonstrated that phylogenetically diverse microbes form birnessite-type minerals as the dominant product of the biologically mediated oxidation of Mn(II)^{18,20,23}. This biogenic form of the mineral is similar to its synthetic analog and composed of poorly crystalline hexagonal Mn(IV)-oxide sheets arranged in relatively a few randomly stacked layers^{43,44}. The Mn(IV)-oxide octahedral sheets are negatively charged, arising from cation vacancy sites, and, substitution of Mn(III) for Mn(IV). The average Mn oxidation state of these biogenic minerals is 3.7-4.0.^{18,45} Hexagonal birnessites are further characterized by high surface area⁴⁶, relatively large redox potential⁴⁷, and low point of zero charge.⁴⁸

The physical and chemical characteristics of hexagonal birnessite type bio-oxides provide these minerals with high sorption capacity and chemical reactivity, explaining their critical role in determining the speciation and distribution of many trace element and pollutant species (both inorganic and organic compounds) in the environment.^{1,45} The Mn(IV) vacancies of hexagonal birnessites, reported to be 16.7%⁴⁹ are highly reactive sites capable of adsorbing divalent metals, such as Pb(II), Cu(II), Ni(II), and Zn(II), via multidentate inner-sphere coordination above and below the sites.⁵⁰⁻⁵⁹ Structural incorporation into the octahedral sheets (by substitution for Mn(IV)) has been observed for Ni(II)⁵⁶⁻⁵⁸, and Cu(II)⁶⁰. Additionally, oxyanionic species such as selenite¹⁰ and arsenite⁶ have also been shown to coordinate to vacancy sites. Other investigators have examined the sorptive and redox properties of birnessite with respect to the treatment of various radionuclides in nuclear power plants⁶¹ as well as their role in the mobility and toxicity of uranium in environmental settings^{23,62}.

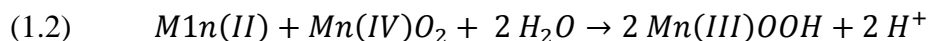
Birnessites are also major natural oxidants, capable of oxidizing As(III) to As(V) within the pH range 4-8^{7,63-66} Cr(III) to Cr(VI),^{8,67-71} and Se(IV) to Se(VI)^{10,72} in aquatic systems. These redox processes are of major importance to the environmental fate of the pollutant species involved, as oxidation state strongly impacts their toxicity and mobility; for instance, Cr(VI) and As(III) are much more mobile and toxic than Cr(III) and As(V), respectively. Therefore birnessite induced oxidation of Cr(III) to Cr(VI) will promote greater toxicity and mobility. On the other hand, conversion of As(III) into As(V) will show the opposite trend. Redox reactivity of birnessite towards inorganic pollutant species is therefore a critical factor in determining the environmental impact of redox-active contaminants.

Interactions of birnessite with organic compounds in soil remediation are of interest as well. Birnessite is being examined for its role in catalyzing the oxidation of polychlorinated biphenyls (PCBs)⁷³ and polycyclic aromatic hydrocarbons (PAHs), a widespread class of carcinogenic pollutants in soil and aquatic environments.⁷⁴⁻⁷⁹ Birnessite is an important component in natural humification processes, such as the Maillard reaction,⁸⁰ and the degradation of organic matter (OM) and related organic compounds (e.g. phenols) via direct oxidation,⁸¹ abiotic catalysis,⁴⁷ and promotion of ring cleavage.⁸² Additionally, the latter process is an important consideration in the cycling of nitrogen⁸³ and carbon (CO₂ generation).⁸² Birnessite has been shown to catalyze the oxidative coupling reaction of soil OM with aromatic compounds and model PAHs.⁷⁴⁻

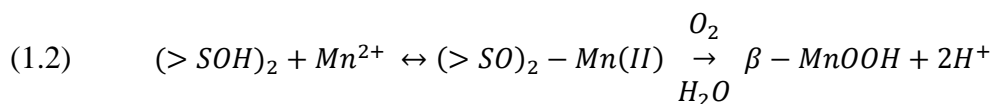
1.1.3 Role of Mn(II) in secondary transformation pathways

In view of the high reactivity and predominance of birnessite in natural settings, it is important to understand not only the interactions of these minerals with trace elements and pollutants, but also the structural and mineralogical transformations they may undergo in the environment. The initial birnessite-type Mn(IV)-oxides produced by microbial and fungal oxidation of Mn(II) readily undergo secondary reactions (redox and/or sorption) that may modify their structure and reactivity. The research described here focuses on the reaction of birnessite with aqueous Mn(II); based on results from recent studies, Mn(II) may exert major control on MnO_x structure. Early studies on this subject reported strong impacts on MnO_x mineralogy resulting from the reaction of birnessite with aqueous Mn(II). In early work, Mn(II) sorption to birnessite was shown to result in formation of various Mn(III,IV) phases, including nsutite (γ -Mn(IV, III)(O,OH)₂), ramsdellite (Mn(IV)O₂), cryptomelane (K_{1.3-1.5}Mn(IV, III)₈O₁₆), groutite (α -MnOOH), and manganite (γ -MnOOH) at pH 2.4, 4, 5, 6, and 8, respectively.⁸⁵ Later work involving oxidation of Mn(II) by bacterial spores of *Bacillus* (strain SG-1) in the temperature range 0-80°C, at pH 7.4-8.0, showed formation of hausmannite (Mn₃O₄), feitknechtite (β -MnOOH), and manganite (γ -MnOOH).¹⁵ In this early work, it was assumed that formation of Mn(III)-oxide phases resulted from the structural incorporation of sorbed Mn(II) by birnessite, changing the Mn-O bond length and causing a charge imbalance⁸⁵. Consequently, this unstable mineral structure was theorized to undergo spontaneous transformation to other Mn phases.⁸⁵ Additionally, Mandernack et al.¹⁵ and Tu et al.⁸⁵ also suggested that (under oxic conditions) surface-catalyzed oxidation of Mn(II) by O₂ contributed to structural change.^{15,85}

Recent studies addressing Mn(II) reactivity with birnessite have proposed another reaction that may be involved in the interaction of Mn(II) with birnessite leading to formation of new Mn-oxide phases. This pathway involves reduction of structural Mn(IV) atoms by aqueous Mn(II), where adsorption of Mn(II) at the birnessite surface leads to injection of electrons into the oxide structure and transformation into reduced Mn phases, a mechanism that has been proposed by more than several investigators.^{18,86–88} More recent work⁸⁶ investigated in detail the mineralogical impacts of Mn(II) reaction with birnessite, and reported that the reaction of Mn(II) with birnessite (nominally Mn(IV)O₂) at pH 7.5, under anaerobic conditions leads to reductive transformation of birnessite according to:



This reaction between Mn(II) and Mn(IV) is a comproportionation reaction that yields Mn(III)OOH through a two-step process. In the initial step, the metastable reaction intermediate feitknechtite (β -Mn(III)OOH) is formed. This precursor phase reacts further with Mn(II) and is catalytically converted to the final more stable polymorph, manganite (γ -MnOOH). This latter reaction is consistent with interfacial electron exchange between soluble Mn(II) and insoluble (structural) Mn(III) in feitknechtite catalyzing transformation to manganite. Under oxic conditions, the reaction summarized by chemical equation (1.1) is complemented by surface-catalyzed oxidation of Mn(II) by O₂ leading to increased Mn(II) removal from solution through additional formation of feitknechtite, according to chemical equation (1.2) (where **S** represents surface Mn).



An important recent finding⁸⁶ is that thermodynamic predictions of occurring reactions and transformations have limited merit in these systems; as shown by isotherm experiments conducted at pH 7.5, the onset of birnessite transformation into feitknechtite according to chemical equation (1.1) occurred at Mn concentrations 2 orders of magnitude lower than thermodynamically predicted. This discrepancy between thermodynamic and experimental results is likely due to uncertainty in thermodynamic data of the MnO_x involved (due to size and composition effects), and necessitates experimental work to assess the importance and occurrence of specific transformation pathways.

Secondary transformation pathways involving birnessite and trace metals, such as Zn(II) and Ni(II) are important to consider when examining such Mn(II) induced reactions. Due to its high sorption capacity, hexagonal birnessite is an important sink of trace metals which coordinate to vacancy and edge sites via multidentate inner-sphere bonds.^{23,54,56,58,86,87,89–94} Mn(II)-driven structural modification of birnessite may affect aqueous metal sorption; in these systems, competition between Mn(II) and other aqueous metals present in solution for adsorption sites on the birnessite surface may impact Mn mineralogy. Ternary sorption systems involving Mn(II) and birnessite remain largely unexplored, although recent studies have begun to address operational mechanisms. Formation of hetaerolite (ZnMn_2O_4) and hydrohetaerolite during treatment of biogenic birnessite with mixed Zn(II)/Mn(II) solutions at pH 7, attributing formation of these phases to Zn(II) which triggered comproportionation of Mn(II) and Mn(IV) was more recently reported.⁹⁵ In other relatively recent work⁸⁷ low Mn(III) content was observed in the layer structure of biogenic birnessite grown in the presence of Ni(II); this was

attributed to inhibition of the comproportionation reaction between Mn(II) and Mn(IV) via competition between aqueous Ni(II) and Mn(II) for adsorption sites on the birnessite substrate.

1.2 Hypotheses

1. Reductive transformation of birnessite by aqueous Mn(II) is dependent on pH which can influence the extent of reaction as well as the available chemical pathways.
2. The extent of reaction and available chemical pathways of birnessite for $\text{pH} \geq 7$ depends on the concentration of Mn(II).
3. Mn(II)-induced transformation of birnessite affects the speciation and solubility of competing metals in multi-sorbate systems (Ni(II) and Zn(II)).

The work in this thesis addresses these hypotheses by combining laboratory wet chemical macroscopic studies of Mn(II) and trace metal sorption onto birnessite with an array of microscopic (SEM) and spectroscopic methods (XAS, XRD, ATR-FTIR, UV-Vis, AAS) to monitor birnessite phase transformation concurrent with changes in solution chemistry.

1.3 Organization of the Thesis

In Chapter 2, a detailed study on Mn(II) interactions with birnessite identified key variables in the transformation of birnessite. In Chapter 3, a multi-sorbate system involving Zn(II), Mn(II), and birnessite was examined in detail. In Chapter 4, reaction systems containing Ni(II), Mn(II) and birnessite were examined.

1.4 Acknowledgment of Previous Publications

- (1) The contents of Chapter 1 were previously published in the article *Influence of pH on the reductive transformation of birnessite by aqueous Mn(II)*, in volume 47,

issue 18 of Environmental Science and Technology (2013). The full citation is included in the References. The contents were reformatted to meet the requirements of the thesis and dissertation style guidelines of Rutgers University.

- (2) The contents of Chapter 2 were previously published in the article *Impacts of aqueous Mn(II) on the sorption of Zn(II) by hexagonal birnessite*, in volume 49, issue 8 of Environmental Science and Technology (2015). The full citation is included in the References. The contents were reformatted to meet the requirements of the thesis and dissertation style guidelines of Rutgers University.

Chapter 2: Influence of pH on the reductive transformation of birnessite by Mn(II)

Abstract

We investigated the effect of pH (5.5–8.5) on the mineralogical transformation of hexagonal birnessite induced by reaction with aqueous Mn(II) (50–2200 μM), using batch sorption experiments, X-ray diffraction analyses, X-ray absorption and infrared spectroscopic measurements. Samples reacted at $\text{pH} < 7.0$ exhibited disrupted stacking of birnessite sheets, but no mineralogical transformation products were observed. At pH 7.0 and 7.5, reaction with Mn(II) under anoxic conditions caused reductive transformation of birnessite into manganite ($\gamma\text{-MnOOH}$), whereas at pH 8.0 and 8.5, conversion into hausmannite (Mn_3O_4) occurred. Feitknechtite ($\beta\text{-MnOOH}$) is a major transformation product at low Mn(II) inputs at pH 7.0–8.5, and represents a metastable reaction intermediate that is converted into manganite and possibly hausmannite during further reaction with Mn(II). Thermodynamic calculations suggest that conversion into hausmannite at alkaline pH reflects a kinetic effect where rapid hausmannite precipitation prevents formation of thermodynamically more favorable manganite. In oxic systems, feitknechtite formation due to surface catalyzed oxidation of Mn(II) by O_2 increases Mn(II) removal relative to anoxic systems at $\text{pH} \geq 7$. The results of this study suggest that aqueous Mn(II) is an important control on the mineralogy and reactivity of natural Mn-oxides, particularly in aqueous geochemical environments with neutral to alkaline pH values.

2.1 Introduction

Hexagonal birnessite type minerals have garnered much interest due to their natural ubiquity, unique structural and reactive properties, and for their potential impact on the

fate and transport of a diverse range of chemical species in the environment.^{20,22,42,96}

These phyllosulfates dominate Mn mineralogy in a variety of geochemical environments with reported occurrences in soils, marine Mn–Fe nodules, and desert varnishes.⁴² Hexagonal birnessites are the main product derived from the biologically catalyzed oxidation of Mn(II),^{18,20,23,96,97} and are structurally characterized by mineral sheets with hexagonal layer symmetry and a significant proportion of reactive anionic vacancy sites.⁴³ They are further noted for significant Mn(IV) content, with reported average Mn oxidation states of 3.7–4.0,^{18,43,96} as well as for large specific surface area⁴⁶, high redox potential⁴⁷, and low point of zero charge.⁴⁸ Their physical and chemical characteristics provide these minerals with high reactivity with respect to both sorption and redox reactions, explaining their critical role in determining the speciation and distribution of trace element and pollutant species in the environment.^{1,8,49,56,59,94,98,99}

Recent work has shown that hexagonal birnessites are subject to structural and mineralogical changes during reaction with aqueous Mn(II), which suggests that the dissolved Mn(II) concentration represents an important control on the structure and reactivity of Mn-oxides in aqueous geochemical environments. Early work on interactions between aqueous Mn(II) and hexagonal birnessite focused on the adsorption of the aqueous metal by the mineral substrate.^{55,100} Tu et al.⁸⁵ and Mandernack et al.¹⁵ demonstrated that under oxic conditions, reaction of Mn(II) with hexagonal birnessite yielded a variety of Mn-oxide mineral products dependent on pH, with formation of nsutite (γ -Mn(IV,III)(O,OH)₂) and ramsdellite (Mn(IV)-O₂) observed at pH 2.4, cryptomelane (K_{1.3–1.5}Mn(IV, III)₈O₁₆) and groutite (α -Mn(III)OOH) at pH 4.0 and 6.0, respectively, and feitknechtite (β -Mn(III)OOH) and manganite (γ -Mn(III)OOH) at pH >

7. Bargar et al.¹⁰¹ observed the formation of feitknechtite during reaction of aqueous Mn(II) with biogenic hexagonal birnessite in oxic systems at circumneutral pH, and attributed this to electron exchange between adsorbed Mn(II) and structural Mn(IV) yielding Mn(III). A recent study by Elzinga⁸⁶ demonstrated that reaction of aqueous Mn(II) with hexagonal birnessite under anoxic conditions at pH 7.5 leads to bulk transformation of the mineral into manganite through a reductive transformation process whereby the substrate is initially converted into feitknechtite (β -MnOOH) through interfacial electron exchange between adsorbed Mn(II) and structural Mn(IV), followed by Mn(II)-catalyzed conversion of β -MnOOH into the more stable manganite (γ -MnOOH) phase. Other studies have shown the importance of Mn(II) in inducing structural changes of hexagonal birnessite substrates through interfacial electron exchange reactions with bulk Mn(IV) as well.^{6,18,87,93,96,102}

The current study focused on the influence of pH on the reductive transformation of hexagonal birnessite by aqueous Mn(II). Solution pH affects both the extent and mechanisms of metal adsorption onto mineral surfaces,^{12,103–105} and may thus well influence the interaction of Mn(II) with the hexagonal birnessite surface and resulting impacts on Mn-oxide structure and mineralogy. Here, we investigated Mn(II) reactivity with hexagonal birnessite in the pH range 5.5–8.5 with a combination of batch experiments and spectroscopic measurements to assess sorption trends and Mn-oxide reaction products under oxic and anoxic conditions. Our results indicate that pH has a major impact on the pathways and products of the Mn(II)-induced conversion of hexagonal birnessite into lower valence Mn-oxide phases.

2.2 Materials and Methods

2.2.1 Mn-Oxide Substrates

Preparation of hexagonal birnessite (nominally MnO_2 ; approximate full chemical formula $\text{KMn}_5\text{O}_{10.5}$, and reference feitknechtite (β - MnOOH), manganite (γ - MnOOH) and hausmannite (Mn_3O_4) are described in Appendix 1.

2.2.2 Mn(II)–Birnessite Isotherm Experiments.

Birnessite-Mn(II) sorption isotherm experiments were performed at pH values in the range 5.5–8.5. Experiments were conducted mostly under anoxic conditions, using protocols to exclude O_2 described in Appendix 1. Anoxic aqueous suspensions of birnessite were prepared in 0.1M NaCl and maintained at the desired pH using 20 mM of 2-(N-morpholino)ethanesulfonic acid (MES; pH 5.5–6.5), 4-(2-hydroxyethyl)-1-piperazineethanesulfonic acid (HEPES; pH 7.0–8.0), or N-(2-hydroxyethyl)piperazine-N'-(3-propanesulfonic acid) (EPPS; pH 8.5) buffer dissolved in the reaction electrolyte. For each isotherm experiment, samples were prepared from a 250 mL volume of a 0.05 g L^{-1} birnessite suspension prepared in a polyethylene container. Twelve 20 mL aliquots were pipetted from the birnessite suspension into 30-mL opaque polyethylene tubes. The samples were spiked with aqueous Mn(II) from a 0.05 M MnCl_2 stock to achieve initial concentrations in the range 50–2200 μM , and then sealed and equilibrated inside the glovebox for 8 days. The initial aqueous Mn(II) concentrations in all samples were below saturation with respect to any Mn(II) precipitates including $\text{Mn}(\text{OH})_2$ as determined from speciation calculations in Visual MINTEQ employing the MINTEQA2 database.¹⁰⁶ Following reaction, the samples were syringe-filtered through 0.22 μm nitrocellulose membranes, and the filtered solids were syringe washed with 5 mL of anoxic DDI water,

and then dried inside the glovebox prior to IR analysis (see below). Filtered reaction solutes were analyzed for dissolved Mn(II) using the formaldoxime method¹⁰⁷ to determine Mn(II) sorption, calculated as the difference between the initial and final Mn(II) solution concentrations. Isotherm samples for XRD and EXAFS measurements (see below) were prepared using suspension volumes of 2 L to ensure sufficient Mn oxide product for analysis. Control samples were run in parallel to the sorption samples, and consisted of birnessite suspensions identical to those of the sorption experiments, except that no Mn(II) was added. Analysis of the control sample substrates showed no evidence for mineralogical transformation or modification of the birnessite substrate, confirming the sorbent to be stable in the absence of aqueous Mn(II) in the pH range considered.

To assess the influence of O₂ on the solid phase partitioning of Mn(II) in the pH range considered here, a series of oxic Mn(II)-adsorption isotherm experiments was performed as well. The oxic samples were prepared using the same experimental conditions and procedures as described above for the anoxic experiments, except that the experiments were conducted outside the glovebox under ambient conditions.

2.2.3 Spectroscopic Analyses of Mn-Oxide Sorption Products

Sample solids collected from the isotherm and kinetic sorption experiments described above were characterized by X-ray diffraction (XRD) analysis, attenuated total reflectance Fourier transform infrared (ATR-FTIR) spectroscopy, and X-ray absorption spectroscopy (XAS). Details of these analyses are described in Appendix 1

2.3 Results and Discussion

2.3.1 Mn(II)–Birnessite Sorption Isotherms

Figure 2.1 shows the results of the anoxic birnessite-Mn(II) isotherm experiments performed at pH 6.0–8.5. The isotherms report Mn(II) sorption (i.e., the y-axis values) as the difference between the initial and final aqueous Mn(II) concentrations, and thus quantify Mn(II) sorption as the reduction in the Mn(II) solution concentration resulting from Mn(II) interaction with birnessite. We do not normalize Mn(II) removal to the mass of birnessite sorbent, since, as will be shown below, reaction with Mn(II) causes bulk mineralogical transformation of the birnessite substrate and increases the mass of solid phase Mn-oxides present in the samples.

The isotherms presented in Figure 2.1 exhibit a clear pH trend, with generally higher Mn(II) removal observed at higher pH values across the Mn(II) concentration range. These findings are consistent with the notion that metal sorption onto mineral substrates increases with increasing pH.¹⁰⁸ In addition to the extent of Mn(II) sorption, the patterns of Mn(II) removal as defined by the sorption isotherms differ markedly with pH as well. At pH 7.5, the isotherm exhibits high affinity behavior with a sorption plateau of approximately 400 μM Mn(II) removed from solution (Figure 2.1), as previously reported by Elzinga⁸⁶. High affinity partitioning is also observed for the isotherms measured at pH 6.0 and pH 8.5, with sorption maxima of ~ 100 and ~ 800 μM , respectively; the pH 5.5 isotherm (not shown) is similar to the pH 6.0 isotherm with a sorption maximum near ~ 100 μM . The isotherms measured at pH 7.0 and pH 8.0 appear to exhibit two sorption plateaus in the aqueous Mn(II) concentration range considered. At pH 7.0, Mn(II) removal reaches an apparent plateau of 100 μM at dissolved Mn(II)

concentrations of 250–500 μM , but then distinctly increases at aqueous $[\text{Mn(II)}] > 500$ μM , approaching the same sorption maximum of ~ 400 μM observed at pH 7.5 (Figure 2.1). Similarly, at pH 8.0, Mn(II) removal appears to plateau at a level of ~ 400 μM (the same maximum as observed at pH 7.5) for aqueous Mn(II) concentrations up to ~ 450 μM , but then increases at higher Mn(II) solution concentrations toward a plateau of ~ 800 μM , which is similar to the sorption maximum observed at pH 8.5 (Figure 2.1).

The isotherm data presented in Figure 2.1 indicate that both solution pH and the aqueous Mn(II) concentration strongly impact Mn(II) sorption by birnessite. Elzinga⁸⁶ reported that birnessite reacts with Mn(II) to produce Mn(III)OOH phases at pH 7.5 at the aqueous Mn(II) concentrations employed in the current experiments. The strong pH dependence of Mn(II) sorption seen in Figure 2.1 suggests that different or additional Mn(II) removal processes may occur at the other pH values considered here. The spectroscopic analyses presented next address the mechanistic influence of pH and the aqueous Mn(II) concentration on the processes involved in the interaction between Mn(II) and birnessite.

2.3.2 XRD, XAS, and IR Results of Mn-Oxide Sorption Products.

The XRD patterns collected for Mn(II)–birnessite sorption samples reacted in the pH range 5.5–8.5 and at initial Mn(II) concentrations between 200 and 2200 μM are presented in Figure 2.2 (e–u), where they are compared to those of birnessite, feitknechtite, manganite and hausmannite (a–d). The sorption samples show distinct changes in mineralogy as a function of pH and the aqueous Mn(II) input. The XRD patterns of the samples reacted at pH 5.5 and 6.0 and the pH 7.0 sample reacted at low Mn(II) only contain the XRD reflections characteristic of hexagonal birnessite (Figure

2.2, e-g). However, the intensities of the two peaks at $12.3\ 2\theta$ ($7.2\ \text{\AA}$) and $24.8\ 2\theta$ ($3.6\ \text{\AA}$), which arise from 001 and 002 reflections respectively¹⁰⁹, are notably reduced in these samples relative to that of the birnessite starting material (a). This indicates that the ordering of birnessite sheet stacking has been disturbed in these samples, but that no bulk mineralogical transformation has occurred. In contrast, the XRD data of the samples reacted at $\text{pH} \geq 7.5$, and the pH 7.0 samples reacted at intermediate and high Mn(II) inputs (h–u) show the presence of Mn-oxide phases other than birnessite, which indicates that Mn(II) caused reductive transformation of birnessite into secondary Mn-oxide minerals in these samples.

Elzinga⁸⁶ studied Mn(II)–birnessite sorption at pH 7.5 and reported that birnessite converts into manganite ($\gamma\text{-MnOOH}$) through a metastable reaction intermediate (feitknechtite; $\beta\text{-MnOOH}$) during reaction with Mn(II) at this pH, with conversion of the metastable feitknechtite phase into manganite promoted by aqueous Mn(II). Consistent with these findings, the XRD data of the sorption samples reacted at pH 7.5 show the presence of both feitknechtite and manganite, with the proportion of manganite increasing for samples reacted at higher Mn(II) concentrations (Figure 2.2, patterns j–m), an observation further confirmed by IR analyses of the pH 7.5 isotherm samples (see Appendix 1, Figure A1.S1).

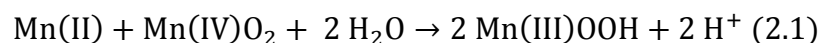
The XRD data of the samples reacted at Mn(II) concentrations levels $\geq 1000\ \mu\text{M}$ at pH 7.0, and $200\text{--}1000\ \mu\text{M}$ at pH 8.0 and pH 8.5 also show evidence for the presence of feitknechtite (Figure 2.2, patterns h, i, n–p, r and s) with additional formation of both manganite and hausmannite seen for the pH 8.0 and 8.5 samples reacted with a Mn(II) concentration of $1000\ \mu\text{M}$ (p, t). For the samples reacted at the highest Mn(II)

concentration (2200 μM), the XRD results indicate the presence of manganite in addition to feitknechtite at pH 7.0 and pH 7.5, and predominantly hausmannite at pH 8.0 and 8.5 (i, m, q, and u). The XRD results qualitatively point to a trend in the types of secondary Mn-oxide mineral products formed during Mn(II)-driven reductive transformation of birnessite as a function of both pH and the level of Mn(II) input in these experiments, where feitknechtite is formed at low and intermediate Mn(II) concentrations across the pH range, manganite is a major secondary phase in the near-neutral pH samples (7.0 and 7.5) reacted at intermediate and high aqueous Mn(II) levels, whereas hausmannite is the dominant secondary phase at alkaline pH and high Mn(II) concentrations. The mineralogical transformations evident from the XRD data are accompanied by significant modifications of the morphology of the Mn-oxide solids as observed with SEM microscopy (Appendix 1, Figure A1.S2).

Quantitative estimates of the mineralogical compositions of the sorption samples are provided by the results of the linear combination fits of the Mn K edge EXAFS data. The k^3 -weighted χ functions of the sorption samples show distinct changes with pH and Mn(II) concentration, and could be fitted as linear combinations (LCs) of the spectra of the birnessite, feitknechtite, manganite, and hausmannite endmembers, as shown by the match of the raw and fitted sorption χ spectra (Appendix 1, Figure A1.S3). The LC fit results are summarized in Appendix 1 Table S1, and graphed in Figure 2.3, which plots the contributions of the various Mn-oxide references determined from the fitting procedure. Consistent with the qualitative trends observed from the XRD data (Figure 2.2), the LC fit results show a progressive increase with [Mn(II)] in the amount of manganite formed at the expense of feitknechtite at pH 7.0 and 7.5, whereas hausmannite

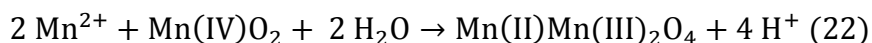
precipitation is observed at pH 8.0 and 8.5 and becomes increasingly important with increasing solution Mn(II) levels at these pH values (Figure 2.3). We note that we consider the LC fit results in Figures 2.2 and 2.3 to represent a semiquantitative estimate of the Mn speciation in the sorption samples, as fractional contributions summing to values <1 indicated that the set of reference spectra used for fitting was not fully representative of the Mn species present (see discussion in Appendix 1).

The mineralogical information obtained from the XRD and XAS analyses presented above can be used to explain the Mn(II) sorption patterns of the isotherm data shown in Figure 2.1. Reductive transformation of birnessite (nominally Mn(IV)O₂) into feitknechtite and manganite by aqueous Mn(II) can be summarized as follows:



Reaction 2.1 defines a 1:1 stoichiometry between aqueous Mn(II) and structural Mn(IV). The concentration of Mn(IV) in the 0.05 g L⁻¹ birnessite suspensions of the isotherm experiments is calculated to be 445 μM based on the Mn content of 48.9 wt. % of the birnessite starting substrate (see Appendix 1). This corresponds reasonably well with the sorption maximum of 400 μM Mn(II) removal observed for the isotherms measured at pH 7.5 and pH 7.0 (Figure 2.1), where feitknechtite and manganite are the dominant reductive transformation mineral products as determined from the XRD and XAS analyses (Figures 2.2 and 2.3). The macroscopic sorption isotherms measured at pH 7.0 and 7.5 are thus consistent with the 1:1 stoichiometry between aqueous Mn(II) and structural Mn(IV) predicted from reaction 2.1.

At pH 8.0 and pH 8.5, hausmannite is produced during reaction of Mn(II) with birnessite (Figures 2, 3). The conversion of birnessite into hausmannite during reaction with aqueous Mn(II) is described by



For this reaction, the stoichiometry of Mn(II) to Mn(IV) is 2:1, that is, double that of reaction 2.1. This agrees with the experimental adsorption isotherms presented in Figure 2.1, which show that the Mn(II) sorption plateau at pH 8.5 and 8.0 is 800 μM , double the amount observed for the pH 7.5 and 7.0 isotherms, and is thus consistent with the operation of reaction 2.2 at alkaline pH in the Mn(II) concentration range considered.

The observed effects of pH on the secondary Mn-oxide phases formed reflect both thermodynamic and kinetic controls on operational pathways of birnessite transformation by aqueous Mn(II). The equilibrium constants (K_{eq}) of reactions 1 and 2 can be calculated (assuming reversible thermodynamic equilibrium) from the standard Gibbs free energy of reaction (ΔG_{R}^0) using $\ln K_{\text{eq}} = -\Delta G_{\text{R}}^0 / RT$, where R is the gas constant and T is temperature, and ΔG_{R}^0 is calculated from the standard Gibbs free energies of formation of the reactant and product species involved ($\Delta G_{\text{R}}^0 = \sum(\Delta G_{\text{f}}^0)_{\text{products}} - \sum(\Delta G_{\text{f}}^0)_{\text{reactants}}$)^{15,86}. Elzinga⁸⁶ showed that application of these thermodynamic equilibrium constants to predict thresholds of Mn(II)-induced transformation of birnessite is limited by uncertainty in thermodynamic parameters of the nanoparticulate Mn-oxide minerals involved; nevertheless, they provide useful constraints on the relative stabilities of the various secondary Mn-oxide mineral products formed under the experimental conditions applied here. Using tabulated ΔG_{f}^0 values,^{13,110} the thermodynamic equilibrium constants are

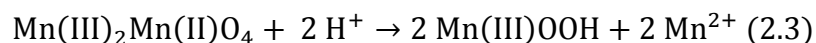
calculated as $K_{eq} = 10^{-12.14}$ for reaction 2.1 producing feitknechtite; $K_{eq} = 10^{-7.01}$ for reaction 2.1 producing manganite; and $K_{eq} = 10^{-17.94}$ for reaction 2.2, which produces hausmannite. Using these constants, the relation between the equilibrium Mn(II) solution activity ($a_{Mn(II)}$) and pH can be derived for each of the transformation reactions, yielding $\log(a_{Mn(II)}) = 2pH - 12.14$ for reaction 2.1 producing feitknechtite; $-\log(a_{Mn(II)}) = 2pH - 7.01$ for reaction 2.1 producing manganite; and $-\log(a_{Mn(II)}) = 2pH - 8.97$ for reaction 2.2, producing hausmannite; $-\log(a_{Mn(II)}) = 2pH - 8.97$ for reaction 2.2, producing hausmannite. Figure 2.4 plots these equilibria over the pH range of 5.0–9.0.

Comparison of the three thermodynamic equilibria shows that manganite is the expected transformation product of the reductive transformation of birnessite by Mn(II) as it maintains the lowest $a_{Mn(II)}$ across the pH range considered, while feitknechtite is the least stable (Figure 2.4). The presence of feitknechtite and hausmannite in our samples (Figures 2.2, 2.3, A1.S3) thus indicates that thermodynamic considerations alone cannot explain the experimental results. The pH dependence of the equilibria indicates that conversion of birnessite into lower- valence feitknechtite, manganite and hausmannite becomes less favorable (i.e., requires higher aqueous Mn(II) concentrations) with decreasing pH, which is due to the release of protons during transformation as defined in reactions 1 and 2. This is consistent with the experimental observation of MnOOH and Mn₃O₄ phases appearing in the samples reacted at $pH \geq 7.0$ but not at lower pH values (Figures 2.2, 2.3, A1.S3). Feitknechtite has been identified as a transient phase in the overall conversion of birnessite into manganite at pH 7.5, where transformation of metastable feitknechtite into stable manganite is accelerated by reaction with aqueous Mn(II).⁸⁶ We attribute the presence of substantial feitknechtite in the samples reacted at

pH 7.0 and pH 7.5 using low Mn(II) inputs to the relatively slow kinetics of feitknechtite conversion into manganite under these conditions, requiring reaction times longer than the 8 days allowed here to go to completion.

Kinetic factors are also likely in play for the pH 8.0 and 8.5 samples, where reaction of birnessite with Mn(II) produces hausmannite (Figures 2.1 through 2–3) despite the fact that conversion to manganite is predicted to be thermodynamically more favorable (Figure 2.4). This suggests that the kinetics of the transformation of birnessite to hausmannite at these high pH values are fast relative to those of the conversion to manganite, so that the reaction producing hausmannite (reaction 2.2) effectively outcompetes the formation of manganite (reaction 2.1). The absence of hausmannite in the pH 7.5 and 7.0 samples (Figures 2.2 and 2.3) indicates that hausmannite precipitation is either much slower (relative to manganite formation) than at pH 8.0 and 8.5, or not thermodynamically favorable under these conditions. Further thermodynamic and kinetic studies are needed to resolve in more detail the factors controlling transitioning from manganite to hausmannite precipitation as the major pathway of birnessite transformation by aqueous Mn(II) at $\text{pH} > 7.5$. The pathway of the conversion of birnessite into hausmannite is not entirely clear from our data, although some constraints can be defined. The presence of feitknechtite in the pH 8.0 and 8.5 isotherm samples reacted at low Mn(II) concentrations (Figures 2.2 and 2.3) suggests that the conversion of birnessite into hausmannite may proceed through a metastable feitknechtite intermediate, as in the conversion into manganite at pH 7.5⁸⁶. However, a kinetic experiment conducted at pH 8.5 and an initial Mn(II) concentration of 1000 μM (Appendix 1, Figures A1.S4 and A1.S5), does not show evidence for the presence of feitknechtite at any time point in the

10 day experimental time frame, although hausmannite forms within half an hour. This indicates either that hausmannite formed directly in this experiment without crystallization of a mineralogically distinct reaction intermediate, or that any intermediate feitknechtite was quickly converted into hausmannite and did not build up to a detectable extent. Resolving the role of feitknechtite in the conversion of birnessite to hausmannite at alkaline pH requires further study. Since manganite rather than hausmannite is the thermodynamically predicted endproduct of birnessite transformation, it is useful to consider the stability of hausmannite against conversion into manganite under the experimental conditions applied here. The thermodynamic equilibrium between hausmannite and manganite is described by

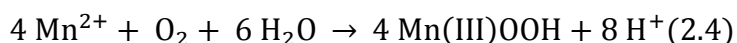


The equilibrium constant for this reaction is $K = 10^{10.92}$ as calculated from the ΔG_f^0 values of the reactant and product species involved using the procedure described above. At pH 8.5, the equilibrium Mn(II) solution activity maintained by this reaction is calculated as 0.83 μM , which is 2–3 orders of magnitude smaller than the equilibrium Mn(II) solution concentration of $\sim 300 \mu\text{M}$ where the sorption plateau is reached in the pH 8.5 isotherm (Figure 2.1). This suggests that, once formed, hausmannite is stable with respect to conversion to manganite under our experimental conditions, although, as noted above, the utility of thermodynamic calculations to accurately predict the behavior of the nanoparticulate experimental systems studied here may be limited. ATR-FTIR analysis of a 6 month anoxic Mn(II)–birnessite sorption sample reacted at pH 8.5 (Appendix 1, Figure A1.S5) indicates no manganite and the persistence of hausmannite, which suggests long-term stability of hausmannite under these conditions consistent with

thermodynamic prediction. Of note in Figure 2.1 are the “kick-ups” seen in the experimental isotherms measured at pH 7.0 and 8.0, where Mn(II) removal increases notably from an apparent lower to a higher sorption plateau within the experimental Mn(II) solution concentration range applied. These distinct increases in Mn(II) sorption are correlated with the onset of feitknechtite formation at pH 7.0 (Figures 2, 3, Appendix 1, Figures A1.S1, A1.S3), and with the onset of hausmannite precipitation at pH 8.0 (Figures 2.2 and 2.3), and thus identify Mn(II) solution thresholds for the transformation of birnessite into feitknechtite and hausmannite, respectively. At pH 8.0, the rise in Mn(II) sorption to a level of 800 μM as the solution $[\text{Mn(II)}]$ increases to 1 mM (Figure 2.1) reflects a kinetic effect where acceleration of hausmannite formation with increasing $[\text{Mn(II)}]$ increasingly outcompetes manganite formation.

The results of the pH 7.0 isotherm are of interest from a thermodynamic point of view, as the Mn(II) solution threshold evident from the isotherm can be used to estimate the equilibrium constant for reaction 2.1 ($K_{\text{eq}} = (\text{H}^+)^2 / a_{\text{Mn(II)}}$). Results from IR analyses of the pH 7.0 isotherm samples indicate first appearance of feitknechtite at an aqueous Mn(II) concentration of 274 μM (Appendix 1, Figure A1.S1). This corresponds to a free Mn(II) solution activity of $\sim 100 \mu\text{M}$ calculated with the Davies equation and accounting for solution complexation of Mn^{2+} with Cl^- , yielding an estimated $K_{\text{eq}} = 10^{-10.2}$ for reaction 2.1 producing feitknechtite based on the current data. This compares to a theoretical value of $K_{\text{eq}} = 10^{-12.14}$ calculated from available thermodynamic data as discussed above. The 2 orders of magnitude difference between experimental and theoretical K_{eq} underscores the need for improved estimates of thermodynamic data pertinent to these systems. We note that we consider the experimental K_{eq} value a

preliminary estimate since our sorption experiments were not necessarily designed to achieve sorption equilibrium; we are currently conducting long-term sorption experiments for more accurate estimates of such thermodynamic data from Mn(II)–birnessite sorption isotherm results. The influence of pH on Mn(II)–birnessite interactions is significant under oxic conditions as well, as demonstrated in Figure 2.5, where the oxic and anoxic isotherms measured at pH 6.0–8.0 are compared. At pH 6.0, the oxic and anoxic isotherms overlap, indicating the absence of a significant influence of O₂ on occurring sorption processes. No detectable oxidation of Mn(II) and associated formation of lower valence Mn phases occurs at this pH (Figure 2.2). In contrast, at pH 7.0 and 7.5, and especially at pH 8.0, Mn(II) removal is substantially higher under oxic than under anoxic conditions (Figure 2.5). The IR data from the pH 7.0, 7.5, and 8.0 isotherm sample solids show a much larger fraction of feitknechtite in the oxic samples relative to equivalent samples reacted under anoxic conditions (Figure 2.6). We attribute these findings to surface-catalyzed oxidation of Mn(II) by molecular oxygen under oxic conditions, where sorbed Mn(II) is oxidized to feitknechtite according to the reaction:



The reaction represents a pathway of Mn(II) removal under oxic conditions that is operational in addition to the oxidation of Mn(II) by structural Mn(IV) defined by reaction 2.1, and thus leads to higher overall Mn(II) sorption in oxic experiments relative to anoxic systems. The release of protons in reaction 4 explains the increased significance of this reaction with increasing pH evident from the isotherm data presented in Figure 2.6. Formation of feitknechtite has also been shown during autocatalytic oxidation of Mn(II) in oxic solutions, and during surface-catalyzed oxidation of Mn(II) by O₂ at the

surfaces of goethite and hematite,^{111,112} suggesting feitknechtite as an important metastable Mn-oxide phase in geochemical systems exhibiting abiotic Mn(II) oxidation.

2.4 Environmental Implications

The results from this study show that pH exerts strong control on the extent and pathways of the reductive mineralogical and structural transformation of hexagonal birnessite by aqueous Mn(II). The findings are relevant to aqueous geochemical environments with hexagonal birnessite in contact with solutions containing appreciable dissolved Mn(II), a scenario common in, for example, suboxic riparian soils, the redox-clines of stratified marine and lake water columns, and aquifers affected by acid mine drainage. Solution pH in these environments is an important variable, with marine systems typically having pH values near 8, noncalcareous suboxic and anoxic soils pH values near 7.0, and acid mine drainage having pH values <3.^{13,113} The results of the current study indicate that such pH variations may significantly impact the extent and mechanisms by which dissolved Mn(II) influences the structure and mineralogy of solid phase Mn-oxides in these aqueous geochemical environments, with reductive transformation expected to be particularly relevant at neutral and alkaline pH, whereas effects in acidic systems are likely to be less pronounced. Reductive transformation of hexagonal birnessite by aqueous Mn(II) will radically alter the sorption and redox reactivity of the Mn-oxide mineral fraction, and significantly affect the biogeochemical cycling of trace metal(loid)s that interact strongly with this mineral, including Co, Zn, Pb, Cr, As, and Se. Further studies are needed to define and quantify the thermodynamics and kinetics of the operational reductive transformation pathways, and to assess associated impacts on the fate of sorbed impurities; in turn, the effects of sorbed impurities on the interaction of

Mn(II) with the hexagonal birnessite surface and resulting mineralogical transformations require further study as well.

2.5 Figures

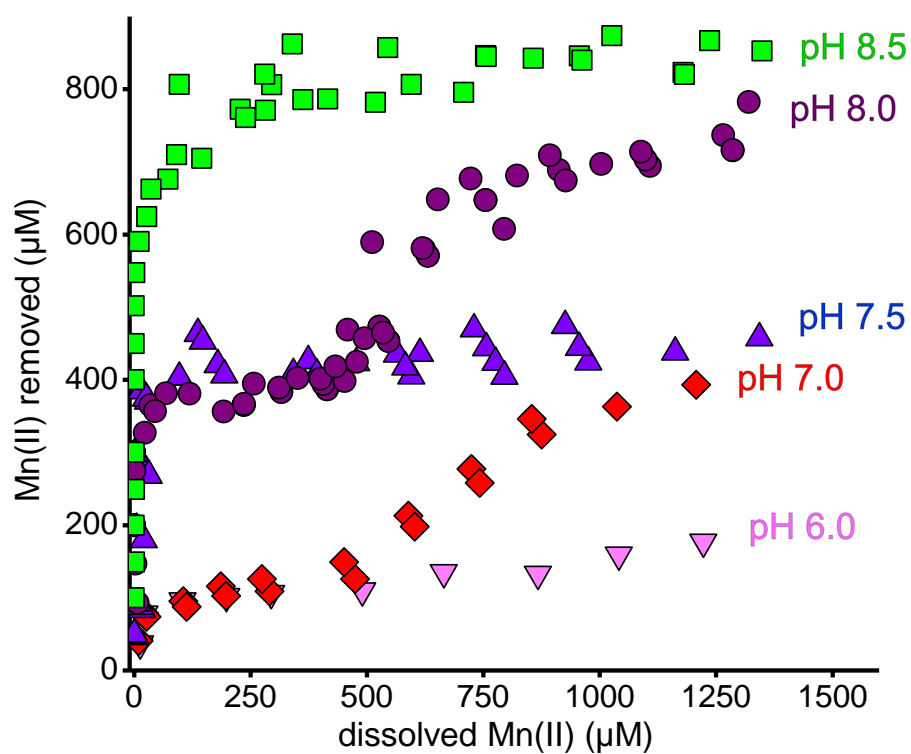


Figure 2.1. Macroscopic results of Mn(II)-birnessite isotherm experiments.

Mn(II) sorption in anoxic 0.05 g L^{-1} birnessite suspensions at pH 6.0–8.5 following 8 days of reaction, plotted as a function of the remaining Mn(II) solution concentration.

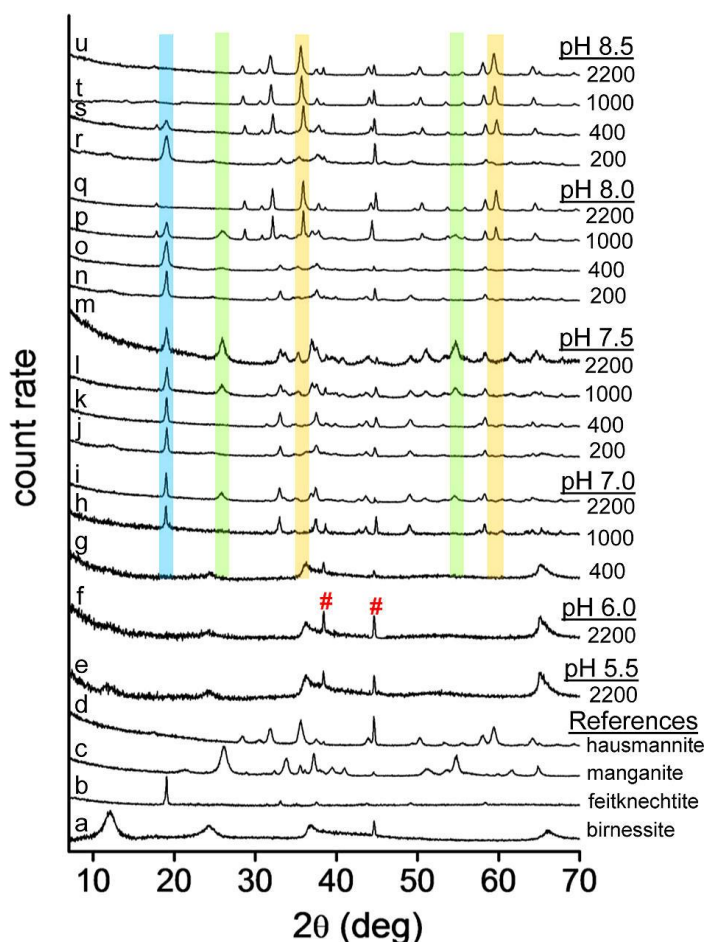


Figure 2.2. XRD results for sorption samples from pH 5.5-8.5.

XRD patterns of Mn-oxide reference samples (a-d) and Mn(II)-birnessite sorption samples (patterns e-u) reacted under anoxic conditions in the pH range 5.5–8.5. The birnessite suspension density in the sorption samples was 0.05 g L^{-1} ; numbers indicated along the patterns represent the initial Mn(II) solution concentrations in μM . The red symbols in pattern f mark peaks resulting from the XRD sample holder that also appear in other patterns. The colored areas in patterns g–u locate XRD peaks characteristic of feitknechtite (blue), manganite (green), and hausmannite (orange) in the sorption samples at $\text{pH} \geq 7.0$ where reductive transformation of birnessite occurs.

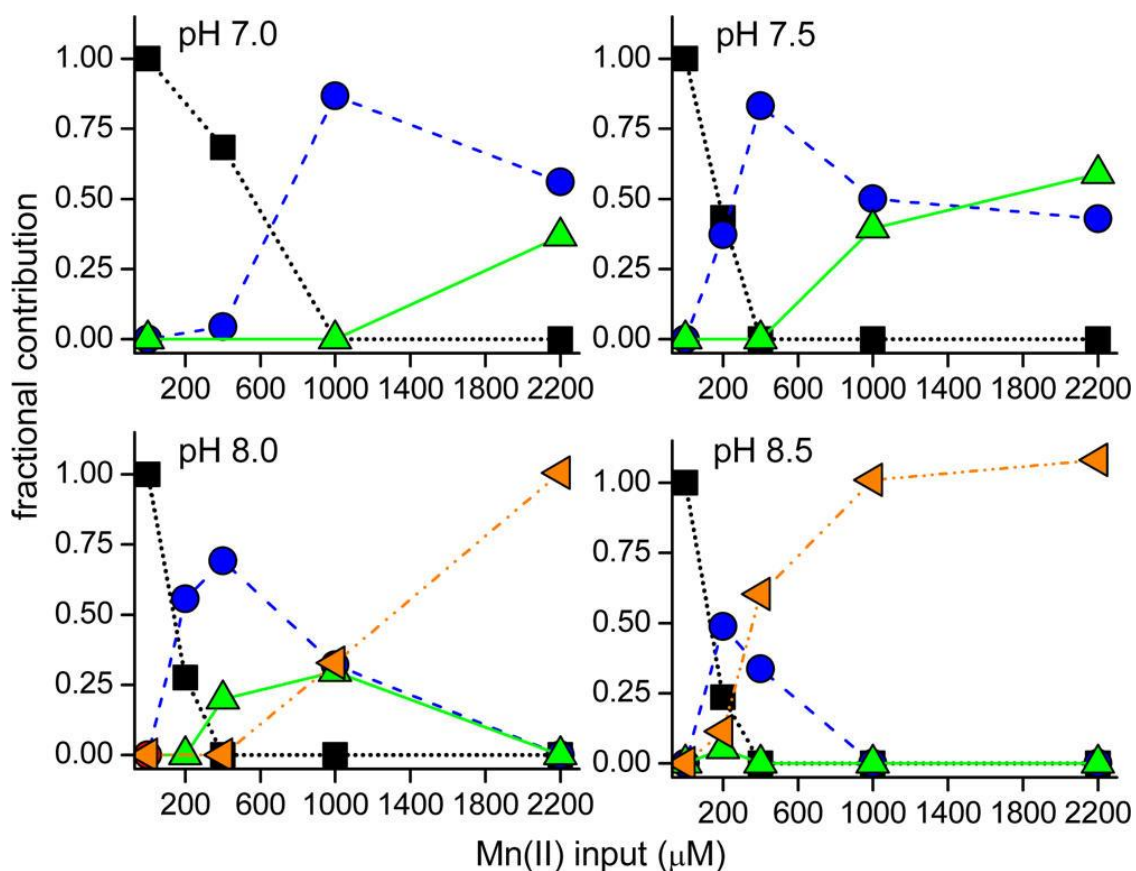


Figure 2.3. Results from linear combination fits.

Results of the linear combination (LC) fits of the k^3 -weighted χ spectra of the Mn(II)-birnessite sorption samples, indicating pH- and [Mn(II)]-driven trends in the fractional contributions of the Mn-oxide phases present (black square = birnessite; blue circle = feitknechtite; green triangle = manganite; orange triangle = hausmannite). The raw and fitted χ spectra are presented in Appendix 1 Figure A2.S3, and the fit results are tabulated in Appendix 1, Table A1.S1.

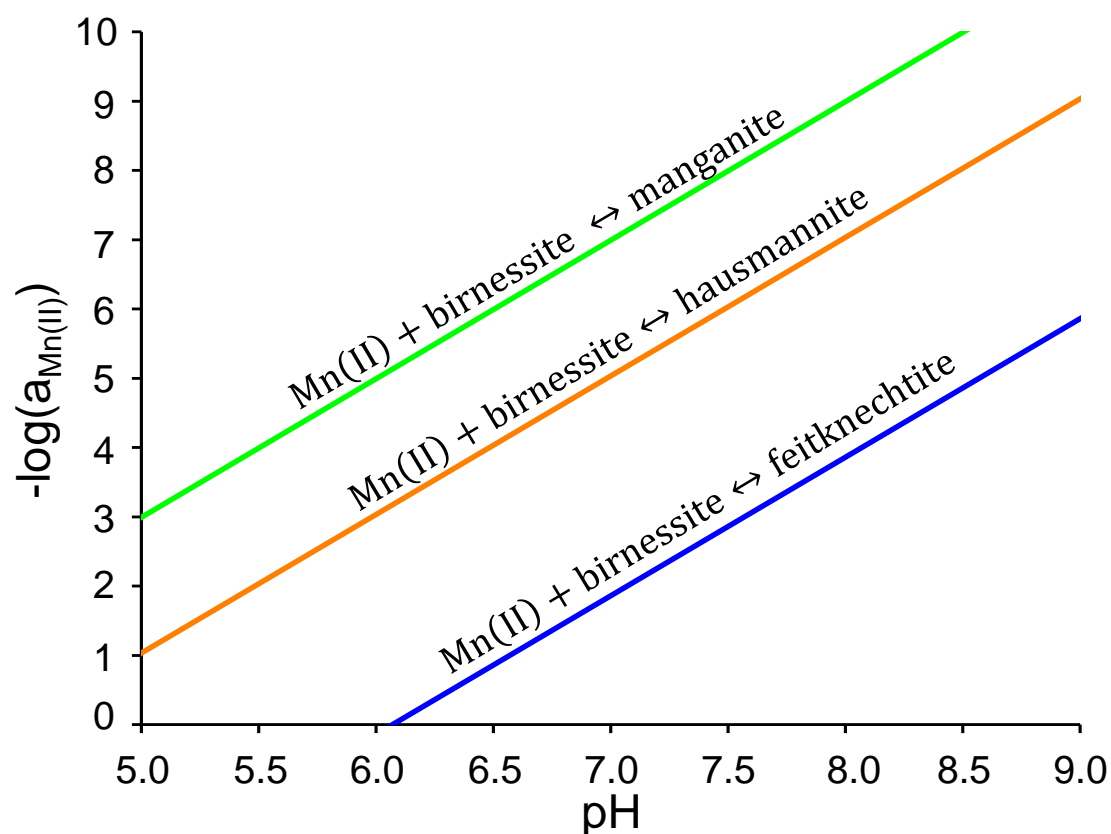


Figure 2.4. Thermodynamic stability plot: feitknechtite, manganite and hausmannite. Theoretical $-\log(a_{\text{Mn(II)}})$ versus pH stability lines of the Mn(II)–birnessite equilibria with manganite, feitknechtite and hausmannite calculated based on thermodynamic data provided in the scientific literature.^{110,114} See text for derivation of the relations. The Mn(II)–birnessite equilibrium with manganite maintains the lowest $a_{\text{Mn(II)}}$ across the pH range, indicating that manganite is the most stable transformation product of the reductive transformation of birnessite by aqueous Mn(II), whereas feitknechtite is the least stable, and hausmannite is intermediate.

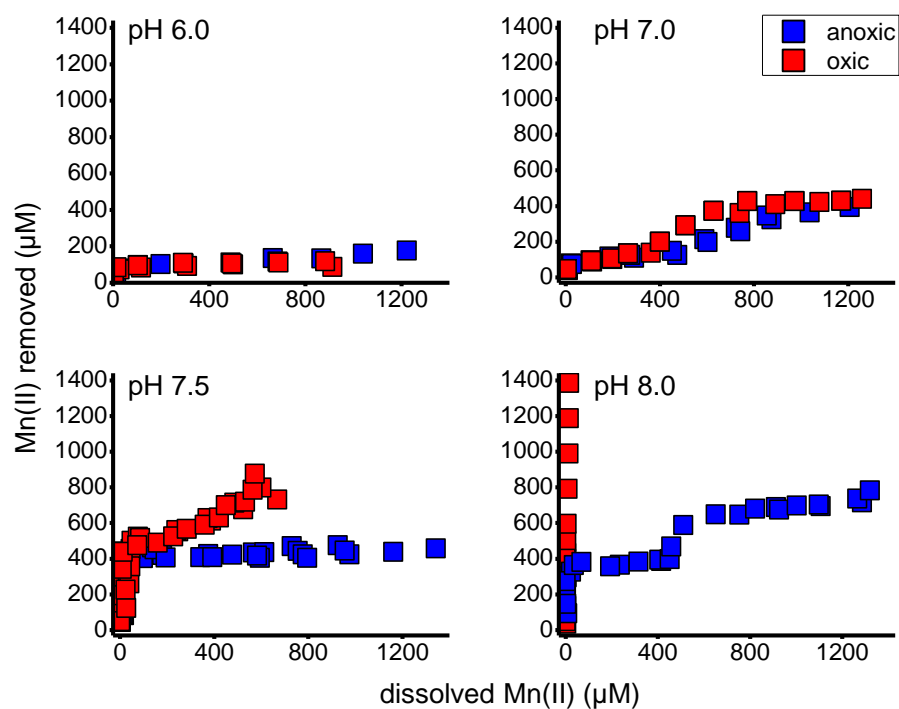


Figure 2.5. Macroscopic results for anoxic and oxic sorption isotherms at pH 6-8.

Comparison of oxic and anoxic Mn(II)–birnessite sorption isotherms at pH 6.0, 7.0, 7.5, and 8.0, measured using a birnessite suspension density of 0.05 g L^{-1} , and a reaction time of 8 days.

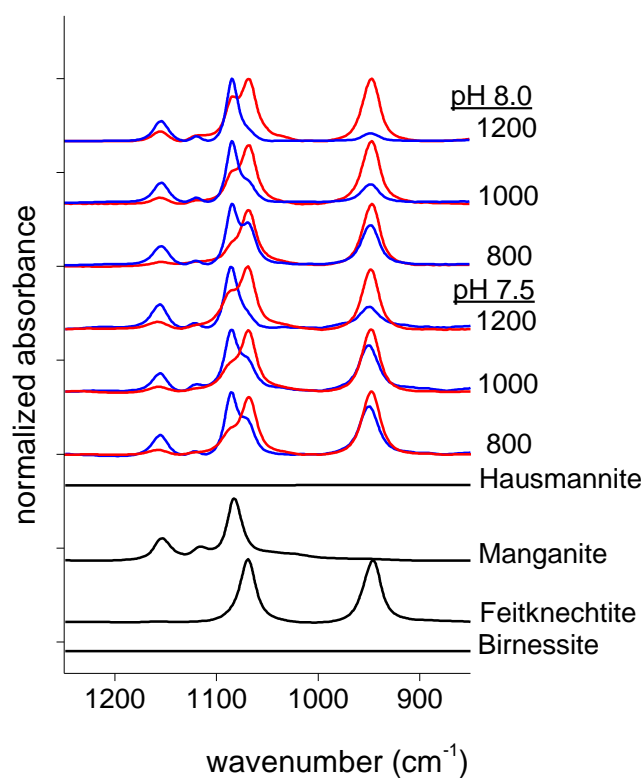


Figure 2.6. ATR-FTIR results.

ATR-FTIR spectra of Mn-oxide references and Mn(II)– birnessite sorption samples (0.05 g L^{-1} suspensions) reacted under oxic and anoxic conditions at pH 7.5 and 8.0. Numbers indicated along the spectra represent the initial Mn(II) solution concentration in μM . Bands in the spectral region shown represent OH bending modes allowing identification of manganite and feitknechtite. Reacted solids from oxic experiments (red lines) show additional formation of feitknechtite as compared to equivalent anoxic samples (blue lines) reacted at the same input of aqueous Mn(II).

Chapter 3: Impacts of aqueous Mn(II) on the sorption of Zn(II) by hexagonal birnessite

Abstract

We used a combination of batch studies and spectroscopic analyses to assess the impacts of aqueous Mn(II) on the solubility and speciation of Zn(II) in anoxic suspensions of hexagonal birnessite at pH 6.5 and 7.5. Introduction of aqueous Mn(II) into pre-equilibrated Zn(II)-birnessite suspensions leads to desorption of Zn(II) at pH 6.5, but enhances Zn(II) sorption at pH 7.5. XAS results show that Zn(II) adsorbs as tetrahedral and octahedral triple-corner-sharing complexes at layer vacancy sites when reacted with birnessite in the absence of Mn(II). Addition of aqueous Mn(II) causes no discernible change in Zn(II) surface speciation at pH 6.5, but triggers conversion of adsorbed Zn(II) into spinel $\text{Zn(II)}_{1-x}\text{Mn(II)}_x\text{Mn(III)}_2\text{O}_4$ precipitates at pH 7.5. This conversion is driven by electron transfer from adsorbed Mn(II) to structural Mn(IV) generating Mn(III) surface species that co-precipitate with Zn(II) and Mn(II). Our results demonstrate substantial production of these reactive Mn(III) surface species within 30 minutes of contact of the birnessite substrate with aqueous Mn(II). Their importance as a control on the sorption and redox reactivity of Mn-oxides towards Zn(II) and other trace metal(loid)s in environments undergoing biogeochemical manganese redox cycling requires further study.

3.1 Introduction

Manganese oxides are recognized for their important role in controlling the fate of trace elements and pollutants in the environment. These minerals are believed to be of primarily biogenic origin, resulting from the oxidation of Mn(II) by phylogenetically diverse microbes through both direct and indirect Mn(II) oxidation pathways.^{22,42,115} The Mn-oxides produced by bacteria and fungi are nanocrystalline, turbostratic phyllomanganates resembling hexagonal birnessite^{18–20,23,44,45,88,97,115–118}. These reactive primary biominerals are readily reworked through abiotic processes to produce more stable Mn-oxide phases including todorokite, hausmannite, and manganite.^{85–88,93,102,119–121} The geochemical pathways and controls of these secondary transformation reactions are the subject of ongoing research.

Recent work has shown that aqueous Mn(II) may be an important agent of structural modification of hexagonal birnessite.^{15,18,85–88,93,101,102,116,120,122} Work performed in the past 5 years^{86,120} demonstrated bulk reductive transformation of birnessite into lower valence Mn-oxides by aqueous Mn(II). The process starts with the adsorption of Mn(II) atoms at the birnessite surface. Electron transfer from adsorbed Mn(II) to structural Mn(IV) inside the birnessite lattice generates Mn(III) which nucleates as the Mn(III)-oxyhydroxide feitknechtite, β -Mn(III)OOH. This feitknechtite phase is metastable, and subsequently converts into manganite (γ -MnOOH) at pH 7.0–7.5 and into hausmannite (Mn₃O₄) at pH > 8.0.

An important finding from these previous studies is that the transformation of birnessite into feitknechtite, the metastable precursor to manganite and hausmannite, occurs at Mn(II) concentrations substantially lower than thermodynamically predicted,

presumably as a result of uncertainty in thermodynamic data of the Mn-oxide phases involved (due to size and composition effects). For instance, Elzinga⁸⁶ observed conversion of birnessite into feitknechtite in a dilute birnessite suspension of pH 7.5 spiked with 10 μM of aqueous Mn(II), which is two orders of magnitude below the Mn(II) solution threshold of transformation predicted from currently available thermodynamic data. This discrepancy underscores the need for experimental assessment of occurring reactions and transformations in these systems, and additionally indicates that the observed transformations operate at Mn(II) solution levels relevant to natural environments.

Due to its high sorption capacity, hexagonal birnessite is an important sink of trace metals such as Pb(II), Zn(II) and Ni(II) which coordinate to vacancy and edge sites of the octahedral Mn-hydroxide sheets through multidentate inner-sphere bonds.^{54,56,58,59,86,87,89–93,123} It is likely that sorbed metal impurities are impacted by Mn(II)-driven structural modification of the birnessite substrate, and that they in turn influence this process by competing with Mn(II) for adsorption sites on the birnessite surface where electron transfer occurs. Ternary sorption systems remain largely unexplored, although recent studies have started to address operational mechanisms. Chang et al.⁹⁵ reported formation of hetaerolite (ZnMn_2O_4) and hydrohetaerolite during treatment of biogenic birnessite with mixed Zn(II)/Mn(II) solutions at pH 7, which was attributed to comproportionation of Mn(II) and Mn(IV) at the mineral surface triggered by Zn(II). Zhu et al.⁸⁷ observed low Mn(III) contents in the layer structure of biogenic birnessite grown in the presence of Ni(II), and attributed this to competition between

Ni(II) and Mn(II) for adsorption sites on the birnessite substrate inhibiting formation of Mn(III) through comproportionation.

Here, we report results of a detailed study addressing the dynamics and mechanisms of the abiotic processes controlling the solubility and speciation of manganese and zinc in ternary Zn(II)-Mn(II)-birnessite sorption systems, using a combination of batch experiments, X-ray absorption spectroscopy, X-ray diffraction, and infrared analyses. We demonstrate that Mn(II)-Zn(II) co-sorption transitions from being competitive to synergistic as pH increases over a narrow range, and provide evidence for production of reactive Mn(III) surface species that readily react with sorbed Zn(II) and modify the birnessite substrate at pH >7. This study provides new insights into the processes governing manganese and trace metal solubility and speciation in aqueous environments undergoing biogeochemical manganese redox cycling.

3.2 Materials and Methods

3.2.1. Mn-oxide substrates

Preparation of hexagonal birnessite, and reference feitknechtite (β -MnOOH), manganite (γ -MnOOH), hausmannite ($\text{Mn(II)Mn(III)}_2\text{O}_4$), hetaerolite ($\text{Zn(II)Mn(III)}_2\text{O}_4$), and Zn(II)-substituted hausmannite ($\text{Zn(II)}_{0.09}\text{Mn(II)}_{0.91}\text{Mn(III)}_2\text{O}_4$) is described in the Supporting Information (Appendix 1).

3.2.2. Batch sorption experiments

All sorption experiments were conducted under strictly anoxic conditions using established procedures^{86,120} detailed in Appendix 2. Binary isotherms of Zn(II) and Mn(II) sorption onto birnessite were measured to compare the macroscopic sorption behavior of these metals. The experiments employed aqueous suspensions of birnessite

(0.1 g L^{-1}) prepared in 0.1 M NaCl and maintained at pH 7.5 or 6.5 using 20 mM HEPES or MES buffer, respectively. Samples were prepared from a 250 mL suspension volume from which twelve 20-mL aliquots were pipetted into 30-mL opaque polyethylene tubes. The samples were spiked with aliquots of 0.05 M MnCl_2 or ZnCl_2 stock to achieve initial Zn(II) or Mn(II) concentrations in the range of $50\text{--}2200 \text{ }\mu\text{M}$, and then sealed and equilibrated inside the glovebox for 8 d. Following reaction, the samples were syringe-filtered through $0.22 \text{ }\mu\text{m}$ nitrocellulose membranes to collect the reaction solutes for analysis of dissolved Mn(II) or Zn(II) using flame atomic absorption spectrometry (FAAS), while the filtered solids were washed with DI water and dried (at room temperature) inside the glovebox. Metal sorption was calculated as the difference between the initial and final Zn(II) and Mn(II) solution concentrations.

Kinetic studies were conducted to monitor Mn(II) and Zn(II) sorption in both binary (i.e. Zn(II) -birnessite and Mn(II) -birnessite) and ternary (Zn(II) - Mn(II) -birnessite) sorption systems at pH 7.5 or 6.5, using the same birnessite suspension density and background electrolyte as for the isotherms experiments described above. In the binary experiments, suspensions were spiked with either Zn(II) ($200 \text{ }\mu\text{M}$) or Mn(II) (1000 or $1200 \text{ }\mu\text{M}$). Metal sorption was tracked over the course of 9 days by regular withdrawal of 10 mL subsamples which were filtered through $0.22 \text{ }\mu\text{m}$ nitrocellulose membranes. Suspensions were shaken before subsample withdrawal to maintain a constant suspension density. The filtered solutes were analyzed for dissolved Mn(II) or Zn(II) using FAAS, while the solids were syringe-washed with 5 mL of anoxic DI water and then dried inside the glovebox.

The ternary batch kinetic experiments involved a two-step sorption process whereby the birnessite suspension was first equilibrated with Zn(II) and subsequently with Mn(II). In the first step, aqueous Zn(II) was added at an initial concentration of 200 μM , and reacted with the birnessite substrate for 2-3 days. Aqueous Mn(II) was then added at a concentration of 1000 μM (pH 7.5) or 1200 μM (pH 6.5), and allowed to react for 1-3 weeks. Sorption of Zn(II) and Mn(II) was monitored through regular withdrawal of 10 mL subsamples as described above for the binary experiments.

Blank and control samples were prepared and sampled in parallel to the binary and ternary sorption samples. The blank samples consisted of identical solutions as used for the sorption samples but without mineral sorbent added, while the control samples consisted of birnessite mineral suspensions with no metal added. Analyses of the solutions and solids of the blanks and controls were performed to check for any changes in aqueous metal concentrations or Mn-oxide mineralogy not related to metal-birnessite sorptive interactions; such changes were not observed.

3.2.3. Solids analyses

Manganese-oxide sample solids from the sorption experiments were characterized by attenuated total reflectance Fourier transform infrared (ATR-FTIR) spectroscopy, powder X-ray diffraction (XRD), and Zn K-edge X-ray absorption spectroscopy (XAS) to determine Mn-oxide mineralogy and Zn speciation. The IR measurements were performed on a Perkin Elmer Spectrum 100 spectrometer equipped with a Balston Parker dry-air purger and a TGS detector. These analyses require only a small amount of material and were performed on the dried Mn-oxide solids retrieved from the batch sorption samples described in the previous section. The samples were further analyzed by

X-ray powder diffraction on a Bruker D8 Advance diffractometer using Ni-filtered Cu K α radiation and a LynxEye XE detector. Samples were stored under anaerobic conditions prior to analysis by ATR-FTIR and XRD, but the actual measurements were performed under ambient conditions. Analysis times were 5 minutes per sample for the IR measurements, and 30 minutes for the XRD analyses. We assume that any changes in Zn and Mn speciation during exposure to air of these dried samples were minimal.

The Zn K-edge XAS spectra were collected at beamline X11A of the National Synchrotron Light Source at Brookhaven National Laboratory, and beamline 12BM-B of the Advanced Photon Source at Argonne National Laboratory. The measurements were performed at room temperature and in fluorescence mode with a Stern-Heald type Lytle detector (X11A) or a Canberra 13 element detector (12BM-B). The XAS sorption samples were prepared under the same conditions and with the same protocols as used for the batch experiments described in the previous section, except that the sample volume was scaled up to 1 L to obtain enough material for analysis. Sample preparation was done entirely inside the anaerobic glovebox, including suspension filtration to retrieve the Mn-oxide solids and subsequent sealing of the wet pastes inside XAS sample holders with Kapton tape. Samples were transported to the synchrotron facility under anoxic conditions using tested protocols¹²⁰, and remained sealed during analysis.

The samples consisted of a kinetic series monitoring Zn(II) speciation in a Zn(II)-Mn(II)-birnessite ternary system (pH 7.5, [Zn(II)]=200 μ M; [Mn(II)]=1000 μ M) with samples retrieved at various time points (0.5 h – 6 d) following the introduction of Mn(II). A second set of sorption samples consisted of a series of birnessite solids reacted with Zn(II) at variable pH (6.5-8.5) and at various concentrations of Zn(II) (50-200 μ M)

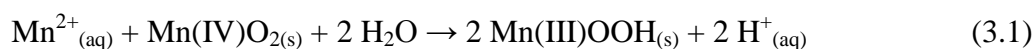
and Mn(II) (0-1000 μM), where the birnessite was first equilibrated with Zn(II) for 2 days and subsequently reacted with Mn(II) for 6 days. Zinc K-edge EXAFS spectra were also collected for reference smithsonite (ZnCO_3), zincite (ZnO), hetaerolite ($\text{Zn(II)Mn(III)}_2\text{O}_4$) and Zn(II)-substituted hausmannite ($\text{Zn(II)}_{0.09}\text{Mn(II)}_{0.91}\text{Mn(III)}_2\text{O}_4$) to assist data interpretation of the sorption samples. These fine-grained reference solids were dispersed in boron nitride and analyzed in transmission mode at room temperature. XAS data analysis is described in Appendix 2.

3.3. Results and Discussion

3.3.1. Sorption isotherms

The binary isotherms of Zn(II) and Mn(II) sorption onto birnessite at pH 7.5 and 6.5 are compared in Figure 3.1. Solution pH strongly impacts the extent of Mn(II) and Zn(II) sorption, with higher sorption levels reached at pH 7.5 than at pH 6.5 for both metals. The increase in sorption with pH is particularly pronounced in the Mn(II)-birnessite system, with a Mn(II) sorption plateau approximately 8 times higher at pH 7.5 than at pH 6.5, whereas maximum Zn(II) sorption increases by a factor ~ 2 when pH increases from 6.5 to 7.5 (Figure 3.1).

The sharp increase in removal of Mn(II) with pH is explained by the IR results obtained for the Mn-oxide sample solids (SI Figure S5a), which show the formation of feitknechtite ($\beta\text{-Mn(III)OOH}$) and manganite ($\gamma\text{-Mn(III)OOH}$) in the pH 7.5 experiments, while these phases are absent at pH 6.5. Elzinga⁸⁶ and Lefkowitz et al.¹²⁰ demonstrated that at near-neutral pH values, Mn(II) is oxidized by lattice Mn(IV) following adsorption onto the birnessite surface, and that the resulting Mn(III) precipitates as MnOOH, a reaction summarized by:



Because of the release of protons, reaction 3.1 becomes less favorable at lower pH. The IR results indicate that this Mn(II) removal mechanism does not occur to any significant extent at pH 6.5 while it is active at pH 7.5 under the experimental conditions applied here (Figure S5a). As in our earlier work,^{86,120} the Mn(II) sorption plateau of ~800 μM observed at pH 7.5 (Figure 3.1) is comparable to the molar concentration of Mn(IV) in the birnessite suspensions, which is estimated at 890 μM based on the 0.1 g L^{-1} suspension density and the Mn content of the birnessite starting substrate (48.9 wt%; see SI). The extent of Mn(II) removal observed at pH 7.5 thus is consistent with the 1:1 stoichiometry between Mn(II) and Mn(IV)O₂ predicted from reaction 3.1, and points to nearly complete Mn(II)-driven transformation of the birnessite starting substrate into secondary feitknechtite and manganite at pH 7.5.^{86,120}

Birnessite interactions with Zn(II) involve coordination of Zn(II) atoms to vacancy sites on the birnessite surface without changes in Zn(II) redox state.^{59,89,91,92,124–128} Such adsorption processes are influenced by competition between metals and protons for coordination to the surface,¹⁰⁸ explaining the observed decrease in Zn(II) adsorption at lower pH (Figure 3.1). Impacts of Mn(II)-driven changes of the birnessite substrate on the retention of Zn(II) are assessed in the ternary experiments described next.

3.3.2. Sorption kinetics

Figures 3.2 and 3.3 compare the kinetic patterns of Mn(II) sorption (Figure 3.2) and Zn(II) sorption (Figure 3.2-3.3) in the binary (i.e. Mn(II)-birnessite and Zn(II)-birnessite) and ternary (Mn(II)-Zn(II)-birnessite) experiments. At pH 6.5, both the binary Zn(II)-birnessite and the binary Mn(II)-birnessite systems show a steep decrease in dissolved

Mn(II) or Zn(II) during the first few hours of interaction, and reach apparent equilibrium within 1-2 days (Figures 3.2a, 3.3a). A similar kinetic pattern is observed for Zn(II) sorption in the binary Zn(II)-birnessite experiment conducted at pH 7.5, where the vast majority of Zn(II) sorption occurs during the first few hours of reaction and stabilizes after approximately 2 days (Figure 3.2-3.3b).

In the binary Mn(II)-birnessite system run at pH 7.5, where reductive transformation of birnessite into manganite takes place (Figures 3.1 and A2.S5), Mn(II) sorption proceeds continuously for 5 days before reaching equilibrium (Figure 3.2b). The IR spectra of sample solids retrieved from this system (Figure A2.S5b) document two distinct stages in the process of Mn(II)-induced reductive transformation of birnessite consistent with our earlier findings.^{86,120} The continuous decline in Mn(II) solution concentrations observed during the first five days of reaction is due to the formation and growth of feitknechtite (β -MnOOH), as demonstrated by the increase in intensity of the characteristic feitknechtite IR bands during this time period (Figure A2.S5b). Feitknechtite production is driven by the interfacial redox processes described above, and is summarized by reaction 3.1. Metastable feitknechtite transforms into the more stable manganite polymorph (γ -Mn(III)OOH) at reaction times > 5 days where no further Mn(II) sorption occurs (Figures 3.2 and A2.S5b). This is consistent with the previously identified catalytic role of aqueous Mn(II) in facilitating the feitknechtite-manganite conversion.⁸⁶

The kinetic sorption patterns of Zn(II) and Mn(II) in the ternary systems differ from those of the binary samples at both pH 6.5 and 7.5 (Figures 3.2 and 3.3). At pH 6.5, sorption of Zn(II) and Mn(II) is competitive, leading to lower amounts of Zn(II) and

Mn(II) sorbed in the ternary Zn(II)-Mn(II)-birnessite sample than in the binary Zn(II)-birnessite and Mn(II)-birnessite samples. Competition between Zn(II) and Mn(II) for adsorption onto the birnessite surface is readily demonstrated by the increase in the Zn(II) solution concentration upon Mn(II) introduction into the pH 6.5 birnessite suspensions pre-reacted with Zn(II) (Figure 3.2-3.3a), indicating competitive displacement of Zn(II) from birnessite surface sites. At pH 7.5, in contrast, sorption of both Mn(II) and Zn(II) is higher in the ternary than in the binary experiments (Figure 3.2b, 3.3b), indicating promotive effects of co-sorption. Synergistic sorption is particularly well illustrated by the quick drop in Zn(II) solution concentration following introduction of Mn(II) in the birnessite suspensions pre-reacted with Zn(II) at pH 7.5 (Figure 3.2-3.3b). The mechanistic underpinnings of these macroscopic sorption trends are assessed below based on the results of Zn K-edge XAS spectroscopy and XRD analyses.

3.3.3. EXAFS and powder XRD data

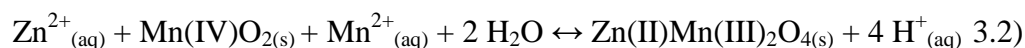
The Zn K-edge EXAFS data collected for the kinetic experiments conducted at pH 7.5 and 6.5 are shown in Figure 3.4, with the k^3 -weighted χ functions shown in Figure 4a, and the corresponding radial structure functions (RSFs) in Figure 3.4b. The XAS data of the reference compounds hetaerolite and Zn(II)-substituted hausmannite are included in these figures as well. Also shown in Figure 3.4a are the shell-by-shell fits of the binary Zn(II)-birnessite sorption samples and the reference compounds, and the linear combination fits of the ternary sorption samples. The procedures used to generate these fits are described in Appendix 2, and the corresponding fit parameters are summarized in Tables A2.S1 (shell-by-shell fits) and A2.S2 (LC fits).

The shell-by-shell fits of the Zn EXAFS data for the Zn(II)-birnessite samples reacted in the absence of aqueous Mn(II) (Figure 3.4 spectra a and e; fit results in Table A2.S1) show that Zn(II) adsorbs as mixture of octahedral and tetrahedral surface complexes onto the birnessite surface (see discussion in Appendix 2). Coordination occurs predominantly at vacancies in the birnessite sheet structure, where Zn(II) forms triple-corner-sharing inner-sphere complexes, consistent with the results of previous studies^{59,89,91,92,124,126–129}

Addition of Mn(II) to the Zn(II)-reacted birnessite suspensions has little impact on the speciation of sorbed Zn(II) at pH 6.5, based on the nearly identical EXAFS results of the ternary and binary sorption samples reacted at this pH (Figure 3.4, Table A2.S1). In contrast, at pH 7.5, introduction of Mn(II) leads to rapid changes in Zn(II) speciation as shown by the XAS data of the kinetic samples. The sample collected 30 minutes after Mn(II) addition exhibits distinct changes in spectral features relative to the starting sample, and these become increasingly pronounced over longer sorption times (Figure 3.4). Comparison to the reference spectra shows that the changes are due to the formation and growth of Zn(II) precipitates resembling hetaerolite ($\text{Zn(II)Mn(III)}_2\text{O}_4$; Figure 3.4). The spectra of the sorption samples collected over the course of the 6 day reaction time period are successfully reproduced with linear combination fits using the hetaerolite spectrum and the spectrum of Zn(II)-sorbed birnessite prior to Mn(II) addition as endmembers (Figure 3.4; Table A2.S2). This indicates that Zn(II) is present as a mixture of Zn(II) surface complexes and hetaerolite-type precipitates. The LC fits show that the proportion of precipitated Zn(II) increases from ~30% of Zn(II) 30 minutes after the addition of Mn(II) to ~80% after 6 days (Table A2.S2; Figure A2.S1), demonstrating

ongoing formation of Zn(II)-Mn(III)-mineral phases over the course of this reaction time frame.

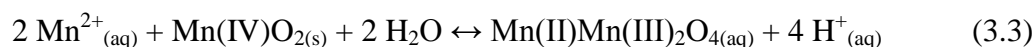
The Zn XAS data of the pH 7.5 ternary experiment suggest formation of hetaerolite in this system, which can be represented by:



Mechanistically, the reaction involves precipitation of Zn(II) with Mn(III) cations that are generated at the birnessite surface through interfacial electron transfer from Mn(II) to lattice Mn(IV). The reaction leads to formation of hetaerolite within the first 30 minutes following the Mn(II) spike (Figures 3.4 and A2.S2; Table A2.S2), an initial sampling time point constrained by the time required to filter the 1 L suspension volume needed to obtain enough Mn-oxide material for XAS analysis. The release of protons makes formation of hetaerolite through reaction 3.2 less favorable as pH decreases, explaining why this phase is observed at pH 7.5 but not at pH 6.5 (Figure 3.4). The precipitation of $\text{Zn(II)Mn(III)}_2\text{O}_4$ correlates with a notable drop in the solution concentration of Zn(II) at pH 7.5 (Figure 3.2), suggesting that formation of this phase lowers Zn(II) solubility. Further inspection of the macroscopic and spectroscopic results reveals additional details of the mechanisms involved in Mn(II) and Zn(II) sorption in the pH 7.5 ternary system, and the composition of the Zn(II) sorption products formed. Sorption of Mn(II) in the ternary experiment exceeds that of the binary experiment (Figure 3.2b). This is perhaps unexpected, as both reaction 3.1 and reaction 3.2 define a 1:1 reaction stoichiometry between Mn(II) and Mn(IV). Since the Mn(IV) concentration of the birnessite suspensions was the same in the binary and ternary experiments ($\sim 800 \mu\text{M}$), total Mn(II) sorption is expected to be the same as well (at $\sim 800 \mu\text{M}$ Mn(II) removed from solution).

The higher than expected sorption of Mn(II) in the ternary system suggests an additional route for Mn(II) removal in these samples not accounted for by reaction 3.2.

X-ray powder diffraction patterns of solids from the pH 7.5 ternary experiment are presented in Figure 3.5. The patterns show that the Zn(II) phases formed are not pure Zn(II)Mn(III)₂O₄, but exhibit XRD reflections at 2θ positions intermediate between those of hetaerolite (Zn(II)Mn(III)₂O₄) and hausmannite (Mn(II)Mn(III)₂O₄). Hausmannite and hetaerolite both have normal spinel structures with Mn(III) occupying the octahedral site, but the tetrahedral site is occupied by Zn(II) in hetaerolite, and by Mn(II) in hausmannite.^{130,131} We have previously shown¹²⁰ that reaction of Mn(II) with birnessite at pH 8.0 and 8.5 readily produces hausmannite according to:



The structural similarity of hausmannite and hetaerolite and the ease with which they precipitate in our experimental systems makes Mn(II)-for-Zn(II) substitution likely during precipitation of hetaerolite in the presence of Mn(II). Such substitutions would account for the XRD results suggesting formation of a hetaerolite:hausmannite solid solution (Figure 3.5), and explain the high level of Mn(II) sorption observed in the ternary system (Figure 3.2b). In support of this proposed mechanism, Hem et al.¹³⁰ demonstrated that solids intermediate in composition between hetaerolite and hausmannite readily form during co-precipitation of Zn(II) and Mn(II) at pH 8.5. In addition, the Zn K-edge EXAFS data of a dilute Zn(II)-hausmannite solid solution are nearly identical to that of pure hetaerolite (Figure 3.4; Table A2.S1), consistent with the notion of facile co-substitution of Mn(II) and Zn(II) in the tetrahedral Me(II) site of Me(II)Mn(III)₂O₄. Combined, our macroscopic and spectroscopic results point to

formation of spinel $\text{Zn(II)}_{1-x}\text{Mn(II)}_x\text{Mn(III)}_2\text{O}_4$ phases during reaction of Mn(II) with Zn(II)-sorbed birnessite at pH 7.5, triggered by the formation of reactive surface Mn(III) species that precipitate with sorbed Zn(II) and Mn(II).

The formation rate of hetaerolite-like phases in the pH 7.5 ternary system (within 30 minutes; Figure 3.4) contrasts with the much slower precipitation of secondary Mn(III) phases in the binary Mn(II)-birnessite experiment at pH 7.5, where formation of feitknechtite (β -Mn(III)OOH) is not seen until 1 day of reaction with Mn(II) (Figure A2.S5). Since the binary and ternary experiments were run under identical conditions, it is unlikely that this is due to a difference in the rate and extent of Mn(III) production in these systems. An important factor in Mn(III) mineral formation is the lability of Mn(III), which rapidly disproportionates into Mn(II) and Mn(IV).^{132,133} Any surface Mn(III) not incorporated into secondary precipitates will therefore quickly disappear again. Our results indicate that adsorbed Zn(II) “traps” Mn(III) by inducing precipitation of $\text{Zn(II)}_{1-x}\text{Mn(II)}_x\text{Mn(III)}_2\text{O}_4$ solids. The much slower precipitation of β -Mn(III)OOH suggests that this phase is a less effective sink for stabilizing the labile Mn(III) species that form at the birnessite surface than is hetaerolite.

The IR data of the pH 7.5 sample solids (Figures A2.S5) demonstrate that formation of feitknechtite ultimately occurs in the ternary system as well, but at a later stage than in the binary system. In the ternary experiment, feitknechtite is not observed until 2 days of reaction with Mn(II), while for the binary system this phase forms within the first day (Figure A2.S5b, c). The delay in feitknechtite formation in the ternary experiment can be explained by competitive precipitation of $\text{Zn(II)}_{1-x}\text{Mn(II)}_x\text{Mn(III)}_2\text{O}_4$ and Mn(III)OOH as sinks for Mn(III). The formation of Zn(II)-Mn(III) spinels (Figure

3.4) appears to effectively outcompete precipitation of β -Mn(III)OOH, delaying formation of this phase until the later stages of reaction when a significant fraction of Zn(II) has precipitated as $\text{Zn(II)}_{1-x}\text{Mn(II)}_x\text{Mn(III)}_2\text{O}_4$ (Figure A2.S1). This competition between precipitation of $\text{Zn(II)}_{1-x}\text{Mn(II)}_x\text{Mn(III)}_2\text{O}_4$ and Mn(III)OOH suggests that the pathways of reaction are sensitive to the relative timing of Mn(II) and Zn(II) addition. Additional work is required to determine the influence of the Mn(II) and Zn(II) addition sequence on the speciation and solubility of zinc and manganese in these ternary systems.

In a final set of XAS samples, we assessed the influence of pH (6.5-8.5) and the Zn(II) (50-200 μM) and Mn(II) concentrations (100-1000 μM) on the formation of secondary $\text{Zn(II)}_{1-x}\text{Mn(II)}_x\text{Mn(III)}_2\text{O}_4$ phases in ternary sorption systems. The results are presented in Figure A2.S2, and demonstrate formation of hetaerolite-type phases in all samples reacted at $\text{pH} \geq 7.0$. Linear combination fits show that precipitation of these phases occurs alongside Zn(II) surface complexation (Table A2.S3). The relative importance of $\text{Zn(II)}_{1-x}\text{Mn(II)}_x\text{Mn(III)}_2\text{O}_4$ precipitation increases with increasing pH, and with increasing concentrations of Mn(II) relative to that of Zn(II) (Figures A2.S3 and A2.S4). The nucleation of these phases even at low levels of Zn(II) and Mn(II) demonstrates their potential influence on Zn(II) solubility and speciation in environments where Mn redox transformations occur. These findings emphasize the need for additional work defining in more detail the kinetics and thermodynamics of precipitation of these phases. This would allow prediction of their occurrence in natural systems and their impact on Zn(II) solubility over a range of geochemical conditions. Ongoing work in our laboratory addresses these issues.

3.4. Environmental Implications

Hexagonal birnessite typifies the Mn- oxides found in aqueous geochemical environments, where they are major sinks of trace metals. Because of the high redox reactivity of birnessite, changes in environmental redox conditions may significantly impact the structure of this phase, and impact the solubility and speciation of sorbed trace metals. We show evidence for the formation of reactive Mn(III) species at the surface of hexagonal birnessite during contact with aqueous Mn(II). Resulting impacts on the solubility and speciation of sorbed Zn(II) depend strongly on pH. At pH > 7, aqueous Mn(II) triggers conversion of Zn(II) surface complexes into $\text{Zn(II)}_{1-x}\text{Mn(II)}_x\text{Mn(III)}_2\text{O}_4$ precipitates, and lowers Zn(II) solubility. At pH < 7, in contrast, Zn(II) solubility increases with addition of Mn(II), while no changes in Zn(II) speciation occur. These findings are of importance to the geochemistry of zinc and manganese in geochemical systems where hexagonal birnessite is in contact with solutions that contain significant levels of dissolved Mn(II). Our results suggest that in neutral and alkaline environments, such as marine redoxclines, precipitation of Zn(II)-Mn(III) phases may occur, while in acidic environments, such as acid-mine drainage impacted systems, adsorption of Zn(II) to Mn(IV) phyllomanganates likely dominates. Additional studies on the kinetics and thermodynamics of $\text{Zn(II)}_{1-x}\text{Mn(II)}_x\text{Mn(III)}_2\text{O}_4$ phases are required to assess their importance in natural systems, and their impact on Zn(II) solubility. We observe substantial formation of Mn(III) at the surface of birnessite within minutes of contact of the substrate with aqueous Mn(II). This suggests that these Mn(III) surface species may be an important component of the manganese redox cycle in suboxic environments. Their impacts on the redox and sorption reactivity of manganese towards trace metal(loid)s

other than Zn(II), and their potential importance as a source of soluble Mn(III)^{134,135} require further study.

3.5. Figures

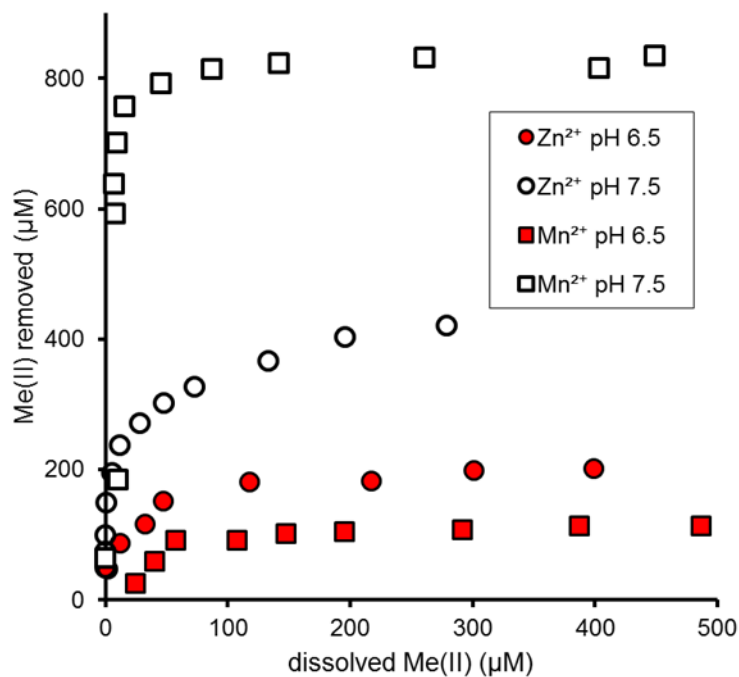


Figure 3.1. Macroscopic results from anoxic metal(II)-birnessite isotherms at pH 7.5. Mn(II)-birnessite (squares) and Zn(II)-birnessite sorption isotherms (circles) at pH 6.5 (red symbols) and pH 7.5 (open symbols). The experiments were run under anoxic conditions in 0.1 g L^{-1} birnessite suspensions for a reaction time of 8 days. Sorption is quantified as the concentration of aqueous metal removed from solution.

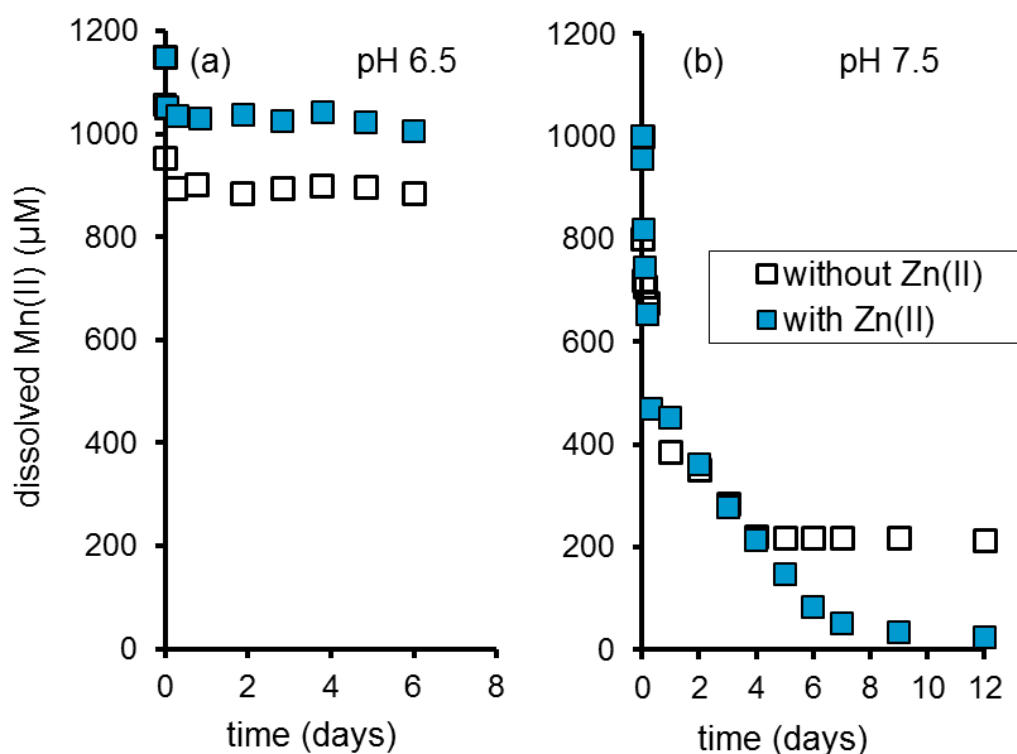


Figure 3.2. Time dependent removal of Mn(II) in binary and ternary experiments.

Time dependence of the Mn(II) solution concentration in anoxic birnessite suspensions (0.1 g L^{-1}) in the absence (open squares) or presence (blue squares) of Zn(II) at (a) pH 6.5 and (b) pH 7.5. In the ternary experiments, Zn(II) (200 μM) was equilibrated with birnessite for 2 days before addition of aqueous Mn(II) (1000 μM at pH 7.5; 1200 μM at pH 6.5). Corresponding Zn(II) sorption profiles are presented in Figure 3.3.

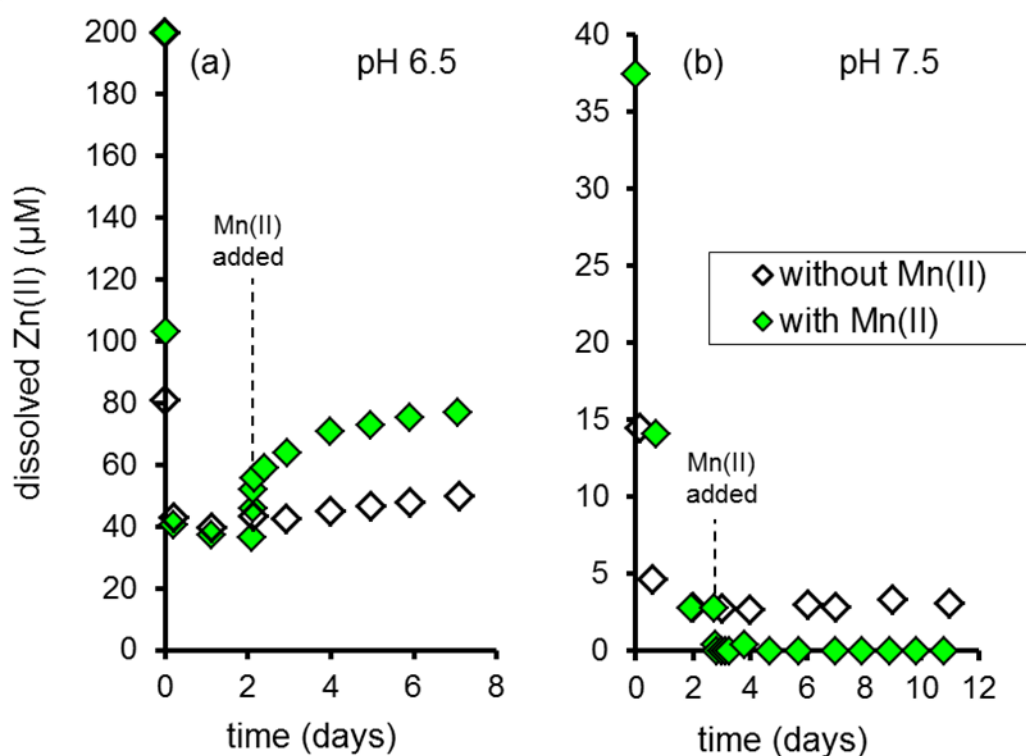


Figure 3.3. Time dependent removal of Ni(II) in binary and ternary experiments.

Time dependence of the aqueous Zn(II) concentrations in anoxic 0.1 g L^{-1} birnessite suspensions at (a) pH 6.5; and (b) pH 7.5 in the absence (open diamonds) or presence (green diamonds) of aqueous Mn(II). The ternary Zn(II)-Mn(II)-birnessite experiments are the same as those presented in Figure 3.2, and involved equilibration of Zn(II) with birnessite for 2 days before Mn(II) was added; the time point of Mn(II) addition is indicated by the dashed line. The Zn(II) concentration in the experiments was $200 \mu\text{M}$, while aqueous Mn(II) was added at a concentration of $1000 \mu\text{M}$ at pH 7.5 and $1200 \mu\text{M}$ at pH 6.5.

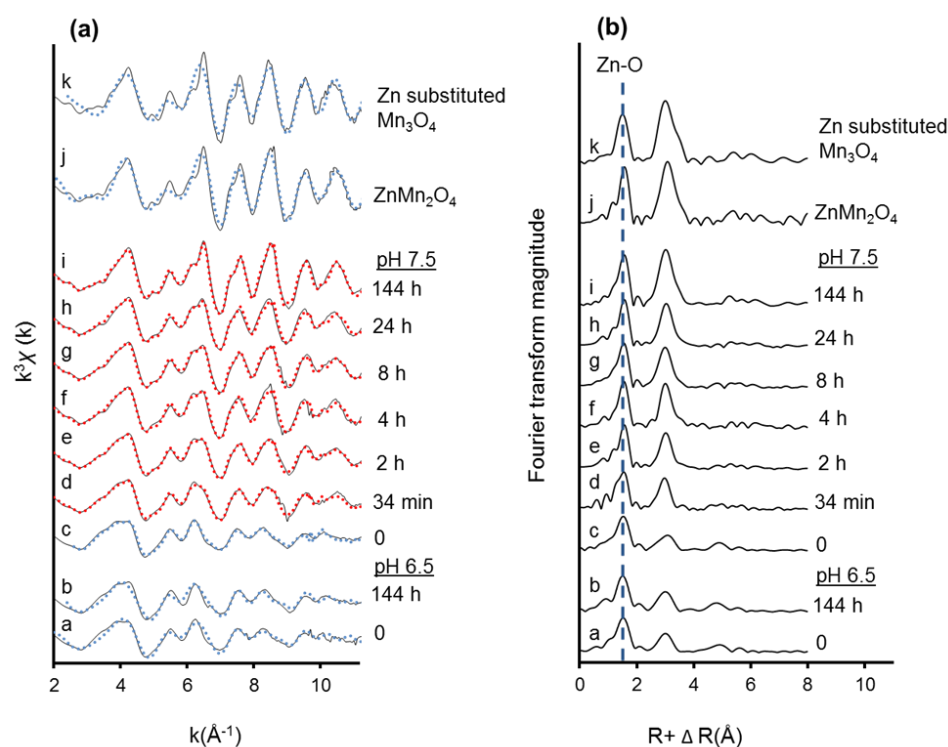


Figure 3.4. Zn K-edge data of Zn(II)-Mn(II)-birnessite sorption samples.

Zn K-edge data monitoring the speciation of sorbed Zn(II) ($200 \mu\text{M}$) in anoxic birnessite suspensions (0.1 g L^{-1}) in the 6 d time frame following addition of aqueous Mn(II) ($1000 \mu\text{M}$) to reaction vessels pre-equilibrated with Zn(II) for 2 days at pH 7.5 and pH 6.5. Panel (a) shows the k^3 -weighted χ functions and (b) the corresponding radial structure functions obtained by Fourier transformation of the raw spectra. The reaction times following the Mn(II) spike are indicated along the spectra. The $t=0$ samples received no Mn(II). The two top spectra (j and k) are for the reference compounds hetaerolite (ZnMn_2O_4) and Zn(II)-substituted hausmannite ($\text{Zn(II)}_{0.09}\text{Mn(II)}_{0.91}\text{Mn(III)}_2\text{O}_4$). In panel (a), the raw spectra are shown in black, blue dotted lines represent shell-by-shell fits (spectra a-c, j and k) and red dotted lines represent linear combination fits(d-i).

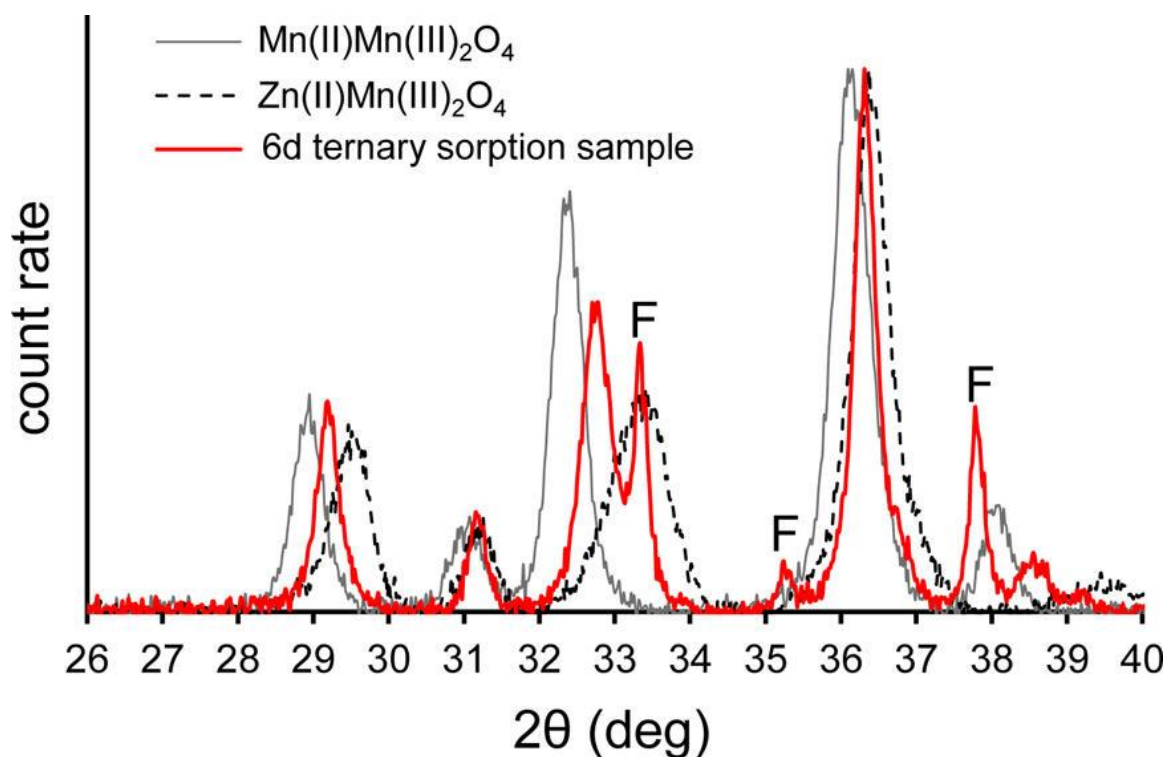


Figure 3.5. X-ray powder diffraction: Mn_3O_4 , ZnMn_2O_4 and ternary sorption product.

X-ray powder diffraction (XRD) patterns comparing major reflections of the reference compounds hausmannite ($\text{Mn(II)Mn(III)}_2\text{O}_4$) and hetaerolite ($\text{Zn(II)Mn(III)}_2\text{O}_4$) to those of the Mn-oxide solids of the pH 7.5 ternary sorption sample where birnessite was first equilibrated with $200\ \mu\text{M}$ Zn(II) for 2 days and subsequently reacted for 6 d with $1000\ \mu\text{M}$ Mn(II) . The label “F” indicates peaks associated with feitknechtite in the data of the sorption sample. The full XRD patterns collected for these samples are presented in

Figure A2.S7.

Chapter 4: Impact of Mn(II)-driven transformation of Ni(II) sorbed birnessite

Abstract

We investigate the role of Mn(II) interactions with birnessite on the solubility and speciation of pre-sorbed Ni(II). Employing flame AAS, UV-Vis spectroscopy XAS, XRD and FTIR spectroscopy, we quantify changes in solution chemistry and concurrent substrate modifications in anoxic batch sorption studies. In Ni(II)-birnessite experiments manually maintained at pH 6.5 and 7.5, Ni surface complexes at vacancy and particle edges were observed; an additional edge sharing Ni complex was observed in the presence of MES or HEPES. The influence of these buffers on Ni speciation is relatively minor compared to the impact of aqueous Mn(II), highlighted by the macroscopic and microscopic results of pH 7.5 experiments. At pH 6.5, competitive sorption between Ni(II) and Mn(II) without bulk structural transformation of birnessite is observed in ternary experiments. At pH 7.5, ternary experiments demonstrate the influence of each metal reactant on the speciation of Ni and Mn. Transformation of Ni(II)-birnessite to a feitknechtite-like phase bearing Ni(II) is evident by XRD analysis, without any further conversion to manganite, as occurs in Mn(II)-birnessite systems, observed. Macroscopic data demonstrates that Mn(II) enhances Ni(II) sorption. XAS, FTIR, and XRD analyses suggest that Ni(II) is incorporated into the feitknechtite-like structure, but surface complexation cannot be ruled out.

4.1 Introduction

As the major product of the microbially mediated oxidation of Mn(II),^{22,23,96,136,137} birnessite is a ubiquitous and important phyllomanganate in the environment. The biogenic form is characterized by hexagonal sheet symmetry, turbostratic layered stacking, low Mn(III) content, and a relatively high density of Mn(IV) vacancy sites;¹³⁸ these vacancies yield a negative lattice charge that is balanced by coordinating cations in the interlayer region.⁴² Birnessite is further characterized by high specific surface area,⁴⁶ and low point of zero charge.⁴⁸ Due to their physical and chemical properties, birnessite minerals exhibit relatively high reactivity with a variety of chemical species and play an important role in the geochemical cycling of trace metal(loid)s.^{1,54,89,116,139–141}

Numerous studies point to an important role of birnessite in the formation of secondary mineral products through abiotic processes. A variety of Mn(III,IV) ox(yhydrox)ides, including nsutite, ramsdellite, cryptomelane, groutite, feitknechtite and manganite, have been shown to form by reacting birnessite with aqueous Mn(II) at fixed pH values.^{15,85} Our more recent work^{86,120} examined Mn(II)-birnessite interactions in detail, focusing on the influence of pH, the ratio of Mn(II) and (structural) Mn(IV) in the system, anoxic versus oxic conditions, and reaction time on the formation of Mn oxides and their associated mechanisms. Biogenic birnessite has been observed to undergo conversion to feitknechtite¹⁰¹, triclinic birnessite¹⁰² and todorokite¹⁸. These secondary abiotic processes are influenced by temperature, pH, phylogeny, microbial growth conditions, and cation effects^{15,18,85,88,101,102,122}; the distinct relationship of Mn(II) with birnessite results in a wide range of impacts to the mineral, from surface passivation⁶⁴ to chemical transformation.^{15,85,101} Transformation of birnessite to secondary mineral phases

has been shown to occur via the reduction of structural (lattice) Mn(IV) by aqueous Mn(II).^{15,85,86,101} In these systems, Mn(II) reductively transformed birnessite into feitknechtite and manganite at pH values 7-8. At pH 8, an additional transformation product, hausmannite (Mn₃O₄), was observed and favored with increasing pH. The concentration of Mn(II) relative to Mn(IV) in birnessite was observed to determine chemical transformation outcomes. At lower inputs of Mn(II), the stacking order of birnessite is disrupted but the bulk mineral structure remains intact; increasing inputs of Mn(II) initially induces transformation to feitknechtite, then manganite.^{86,120} At pH \geq 8, increasing inputs of Mn(II) favored formation of hausmannite.^{120,142}

The formation of secondary Mn oxides from birnessite may be influenced by additional metal sorbates. Trace metal sorbates have been shown to impede the conversion of biogenic birnessite to triclinic birnessite.⁸⁷ In reaction systems containing Mn(II) and birnessite at pH 7.5, Zn(II) inhibits the formation of secondary MnOOH (feitknechtite and manganite) phases. Mn(II)-birnessite interactions may be important determinants in the solubility and speciation of sorbed trace metals. Our previous work on Mn(II)-Zn(II)-birnessite demonstrated how sorption and structural incorporation of Zn(II) into the transformation product occurred at pH 7-8.5. Formation of Zn(II)_{1-x}Mn(II)_xMn(III)₂O₄ was demonstrated to occur more rapidly than feitknechtite due to more effective “trapping” of Mn³⁺ species that would otherwise disproportionate in the absence of Zn(II). At pH 6.5 Mn(II) does not induce transformation of the birnessite structure, but competes for sorption sites with Zn(II).

In the current study, we examine the consequences of sorbing Ni(II) on birnessite prior to addition of Mn(II) at pH 6.5 and 7.5. We examined how introduction of Mn(II)

into Ni(II)-birnessite systems impacted the sorption of each aqueous metal. Where Mn(II) induced transformation of the substrate, we determined the differences in the resulting mineralogy. Employing a combination of batch experiments, X-ray absorption spectroscopy (XAS), powder X-ray diffraction (XRD), and Fourier transform infrared (FTIR) analyses, we probed the differences in binary and ternary systems at pH 6.5 and pH 7.5. The results of this study enhance and foster fresh insight into the geochemical cycling of Mn and Ni species in environments subject to Mn redox transformations.

4.2 Materials and Methods

4.2.1 Experimental Conditions

The birnessite suspension density was 0.1 g L^{-1} , unless otherwise specified. The ionic strength was fixed to 0.1 M using NaCl. Sample pH values were set at pH 6.5 and 7.5 using 20 mM MES or HEPES buffer, respectively, unless otherwise specified.

4.2.2 Experimental protocols to ensure anoxic conditions

Anoxic conditions were achieved by maintaining a glovebox under an atmosphere composed of 95% N_2 and 5% H_2 . The glovebox contains a palladium catalyst that removes any traces of molecular oxygen. The oxygen and hydrogen levels were monitored by a digital $\text{O}_2\text{-H}_2$ meter to confirm anoxic conditions to a detection limit of 0 ppm. Equipment used for each experiment was equilibrated in the anoxic environment for 24 hours prior to use.

4.2.3 Synthesis of Mn-oxide substrates

Hexagonal birnessite was synthesized according to the protocol of McKenzie.¹⁴³ The specific surface area of the product, as determined by N_2 using the Brunauer, Emmett and Teller (BET) method was $42 \text{ m}^2 \text{ g}^{-1}$. The Mn content was 48.9 wt% as determined by

dissolving a known amount of birnessite in 30% HCl followed by analysis of the solution for aqueous Mn(II) by flame atomic absorption spectroscopy (FAAS). The average oxidation state of the material was 4.0 as measured with the iodine titration method.¹⁴⁴ Feitknechtite (β -MnOOH) was synthesized by reacting 400 μ M Mn(II) with an equimolar concentration of Mn(IV) present in a 0.05 g L⁻¹ suspension of birnessite at pH 7.5 for 8 days. Manganite (γ -MnOOH) was synthesized by reacting 36 mM Mn(II) with 1 g L⁻¹ birnessite for 3 months at pH 7, whereas hausmannite (Mn₃O₄) was synthesized following the procedure of Gibot et al.¹⁴⁵

Adapting the procedure of Kovanda et al.,¹⁴⁶ a Ni(II)-Mn(III) layered double hydroxide (LDH) was produced by the following steps. Two 15 mL solutions, one containing MnCl₂·6H₂O and the other NiCl₂·6H₂O, were combined to produce 2:1 mixture of aqueous Ni(II):Mn(II) with a total aqueous metal concentration of 33 mM. A solution of 0.5 M Na₂CO₃ was prepared and adjusted to pH 10 using 1M NaOH; this solution was maintained with vigorous stirring. The Ni(II)-Mn(II) solution was added dropwise to the pH 10 carbonate buffered solution over the course of one hour. Following addition of all reagents, the solution was maintained at pH 10 and allowed to react for 18 hours. At the end of the reaction cycle, the solution was run through a Büchner funnel and the product was rinsed copiously with DDI water. X-ray diffraction (XRD) was employed to confirm the phase identity of the Ni(II)-Mn(III) LDH and other reference materials.

4.2.4 Batch sorption experiments

Binary Ni(II)-birnessite and Mn(II)-birnessite isotherms were measured to compare the macroscopic sorption of Ni(II) and Mn(II) at pH 7.5. An additional Mn(II)-birnessite

isotherm was measured at pH 6.5 . Samples were prepared from an anoxic 250 mL birnessite suspension from which twelve 20-mL aliquots were pipetted into 30-mL opaque polyethylene tubes. To each sample, a calculated amount of a 50 mM Ni(II) or Mn(II) stock solution was added to achieve initial concentrations in the range 50-2200 μM Mn(II) or 25-700 μM Ni(II). The samples were then sealed and equilibrated inside the glovebox for eight days. At the end of the reaction cycle, samples were syringe-filtered through 0.22 μm nitrocellulose membranes to collect the reaction solutes for analysis of dissolved Mn(II) or Ni(II) by FAAS. The filtered solids were rinsed with DDI and dried (at room temperature) inside the glovebox. Metal sorption was calculated as the difference between the initial and final solution concentrations.

Kinetic experiments were performed under binary and ternary conditions at pH 6.5 and 7.5. In the binary experiments, a 250 mL anoxic birnessite suspension was spiked with either Ni(II) (200 μM) or Mn(II) (1000 μM). Metal sorption was monitored by regular retrieval of subsamples over a 22 day time period. The subsamples were filtered, and the supernatants were analyzed for dissolved Mn(II) or Ni(II) to determine the concentration of metal remaining in solution. The solids were syringe-washed with 5 mL of anoxic DDI water and dried inside the glovebox at room temperature. To maintain a constant suspension density in the main vessel, the suspension was mixed thoroughly during sampling.

In the Ni(II)-Mn(II)-birnessite kinetic experiments, birnessite was first reacted with 50-200 μM Ni(II) for 2 days, and subsequently with 1000 μM Mn(II) for an additional 22 days. Metal sorption was monitored through regular withdrawal of 5 mL suspension aliquots from the reaction vessel over the time course of the experiment. The

samples were filtered through 0.22 μm nitrocellulose membranes, and the supernatants were analyzed for dissolved Ni(II) and Mn(II) using FAAS. The solids were syringe-washed with 5 mL of anoxic DDI water and dried inside the glovebox at room temperature. In a second type of ternary experiments (referred to as Mn(II)-Ni(II)-birnessite), the addition sequence of Mn(II) and Ni(II) was reversed. Here, birnessite was first reacted with 1000 μM Mn(II) for five days, and subsequently with 200 μM Ni(II) for an additional two days. Sampling and analyses were identical to those of the other experiments described above.

Blank and control samples were prepared side-by-side to the kinetic experiments described above. The blank reactors consisted of solutions lacking mineral sorbent, but were otherwise identical to those used in the sorption samples. The control vessels lacked aqueous Ni(II) and Mn(II) but were otherwise identical to the experimental suspensions of the sorption systems. Aqueous metal concentrations in the blanks were analyzed to account for any changes in dissolved metal not related to sorption; no such changes were observed. The control experiments were analyzed to assess any changes in Mn-oxide mineralogy not related to interaction of birnessite with aqueous Mn(II) or Ni(II); such changes were not observed. To determine the influence of the MES and HEPES buffers on occurring reactions, three non-buffered samples were prepared using identical protocols and conditions as for sorption samples described above, except for the addition of MES or HEPES buffer. The non-buffered samples consisted of Ni(II)-birnessite samples reacted at pH 6.5 and 7.5, as well as a Ni(II)-Mn(II)-birnessite sample reacted at pH 6.5. An unbuffered ternary sample at pH 6.5 was also prepared, where 1000 μM Mn(II) was added following two day pre-equilibration with 200 μM Ni(II). For each of

these three unbuffered samples, the pH was carefully adjusted and maintained through regular addition of 1 M NaOH.

4.2.5 Analysis of solid materials

The Mn-oxide sample solids procured from the sorption experiments were characterized with a combination of attenuated total reflectance Fourier transform infrared (ATR-FTIR) spectroscopy, powder X-ray diffraction (XRD) measurements, and Ni *K*-edge X-ray absorption spectroscopy (XAS).

ATR-FTIR data collection was carried out using a Perkin Elmer Spectrum 100 IR spectrometer equipped with a TGS detector and a Balston-Parker dry air purger to eliminate CO₂ and moisture from the optics and sample compartments. Spectra were collected over the range 600-4000 cm⁻¹ as the average of 100 co-added scans with a spectral resolution of 4 cm⁻¹ using a Perkin Elmer Miracle ATR accessory containing a single reflection ZnSe ATR crystal. XRD measurements were performed with a Bruker D8 Advance diffractometer equipped with a LynxEye XE detector, using Ni-filtered Cu K α radiation.

Ni *K*-edge (8333 eV) XAS data were collected at beamline X11A located at the National Synchrotron National Laboratory and beamline 12BM-B located at the Advanced Photon Source of Argonne National Laboratory. Spectra were collected at room temperature in fluorescence mode using a Stern-Herald type Lytle detector at X11A, and a Canberra 13 element detector at 12BM-B.

The samples analyzed by XAS consisted of Ni(II) binary and ternary sorption products from a series of experiments that probed the effects of pH, time of reaction with Mn(II), buffer (HEPES and MES) effects, as well as Ni(II) and Mn(II) addition sequence.

The samples were prepared under conditions identical to those of the batch experiments described above, except that the sample volume was scaled up to 1 L in order to procure enough material for analysis. All steps of XAS sample preparation (preparation, equilibration, filtration, collection and mounting) were performed inside the glovebox. Samples were retrieved as wet pastes, sealed in XAS sample holders using Kapton Tape, and transported to the synchrotron facility maintaining anoxic conditions as previously documented.¹⁴⁷ The pH values examined were 6.5 and 7.5. For each of these samples, 200 μM Ni(II) was used. The Ni(II)-Mn(II)-birnessite samples in this pH series involved 1000 μM Mn(II) and were reacted for 5 and 18 days more than the Ni(II)-birnessite samples (for total reaction times of 7 and 20 days, respectively). The kinetic series of samples were performed at pH 7.5 under the same reaction conditions as in the macroscopic experiments; the samples from this series were obtained at time points of 0, 10 minutes, 1 day, 5 days, and 18 days of reaction with respect to Mn(II). A ternary Mn(II)-Ni(II)-birnessite sample was prepared at pH 7.5 by reacting 1000 μM Mn(II) for five days followed by reaction with 200 μM Ni(II) for two days. Ni *K*-edge XAS spectra were additionally procured for the reference Ni(II)-Mn(III) LDH to assist in the interpretation of the sorption sample data. The Ni(II)-Mn(III) LDH was ground and dispersed in boron nitride, using a mortar and pestle, and analyzed in transmission mode at room temperature.

WinXAS 3.1¹⁴⁸ was used in the data processing of EXAFS spectra. Normalization was achieved by using a linear function for the pre-edge region and a second-order polynomial in the post-edge region. The $\chi(k)$ functions were produced by using a cubic spline and Fourier transformation with k^3 weighting over the approximate k range 2.7-

12.5 Å⁻¹. Shell-by-shell fits were performed on Ni(II)-birnessite and ternary samples at pH 6.5 and 7.5. In the fits for Ni(II)-birnessite at pH 6.5 and 7.5, as well as the Ni(II)-Mn(II)-birnessite samples at pH 6.5, Ni was present in a mixture of forms that occur at vacancies and particle edges as discussed in the next section.

Shell-by-shell fits were performed in R-space over the approximate range of 0-4 Å. The programs ATOMS and FEFF7¹⁴⁹ were used to calculate theoretical Ni scattering paths based on the crystal structures of chalcophanite,¹⁵⁰ where Ni was substituted for Zn in the feff input file. An amplitude reduction factor (S_0^2) of 0.8 was determined from a fit of the Ni-O shell of α -Ni(OH)₂¹⁵¹, which has a uniform and distinct first shell containing Ni(II) in octahedral coordination^{152,153}

The Fourier transformed spectra of the experimental χ data for the binary sorption samples revealed two or three main shells surrounding the central Ni atom, consistent with vacancy and edge site Ni(II) complexes.^{56-58,124,140,154,155} The first shell is Ni-O, whereas the other two shells are Ni-Mn shells resulting from different coordination environments (further discussed below).^{56-58,124,140,154,155} Ternary sorption samples at pH 7.5, reacted for more than 10 minutes with Mn(II), exhibited the same Ni-O distance in the RSF (uncorrected for phase shift) and had a Ni-Mn shell centered around 2.7 Å (uncorrected for phase shift).

EXAFS fits on all sorption samples were accomplished by fitting the shells in the RSF with Ni-O, and one or two Ni-Mn shells. To distinguish between the three different Ni-Mn shells present in these samples, we refer to Ni-Mn_A, Ni-Mn_B and Ni-Mn_C, corresponding to the peaks in the RSF located at 2.5 Å, 3.1 Å and 2.7 Å, respectively. The amplitude reduction factor was fixed at 0.8 (as discussed above). Preliminary fits

were performed without any additional constraints; these fits yielded coordination numbers (CN) in the first shell Ni-O shell that, for some samples, exceeded an estimated 20% error. Therefore, a final set of fits were performed with S_0^2 still fixed at 0.8 and constraints imposed on CN in each shell; in the first Ni-O shell, CN was fixed to 6 for all samples. Resolution of vacancy and edge site complexes is limited in EXAFS. The structural parameters derived from shell fits may contain overlap between the coordination environments present in a particular sample.¹⁵⁵ For a sample containing only particle edge sharing complexes, the CN for Ni-Mn would be 2, whereas at vacancies the value would be 6, and a mixture of coordination environments would exhibit an intermediary value. Therefore, for each of the Ni-Mn shells, the CN was constrained to the range 2-6. These constraints produced values for each shell that were both physically realistic and consistent with previous results reported in the literature. The fits yielded radial distance values of 2.05 ± 0.01 Å, 2.86 ± 0.01 Å, and 3.47 ± 0.02 Å for Ni-O, Ni-Mn_A and Ni-Mn_B shells, respectively. Two approaches were attempted for the ternary sample that was reacted with Mn(II) for one day. The optimal fit is reported here, wherein two Ni-Mn shells were fit (Ni-Mn_A and Ni-Mn_C) in place of the single Ni-Mn shell fit applied to the 5-18 d samples (using Ni-Mn_C). This fit yielded Ni-Mn_A and Ni-Mn_C distances of 2.94 Å and 3.11 Å, respectively. The shell fits for the ternary sorption samples at pH 7.5 reacted for 5-18 days with Mn(II) yielded a Ni-Mn_C radial distance of 3.04 ± 0.01 Å. For the complete set of values derived from shell-by-shell fits, the reader is pointed to the SI (Table S1).

4.3 Results and Discussion

4.3.1 Batch kinetic studies

Figures 4.1 and 4.2 compare the kinetic patterns of Mn(II) sorption (Figure 4.1) and Ni(II) sorption (Figure 4.2) in the binary (i.e., Mn(II)-birnessite and Ni(II)-birnessite) and ternary (Mn(II)–Ni(II)-birnessite) experiments. At pH 6.5, the Mn(II)-birnessite system reaches apparent equilibrium within the first day of reaction (Figure 4.1a), while in the Ni(II)-birnessite system equilibrium is reached after approximately 4 days (Figure 4.2a). At pH 7.5, the extent of metal sorption is markedly higher than at pH 6.5 for both binary systems. This is consistent with the general notion that metal sorption increases with increasing pH¹⁰⁸. The amount of time required to reach sorption equilibrium is different at pH 7.5 than at pH 6.5. The pH 7.5 Ni(II)-birnessite system does not reach equilibrium within the 20-day time frame of the experiment (Figure 4.2b), while Mn(II) sorption in the pH 7.5 Mn(II)-birnessite system proceeds for 5 days before reaching equilibrium (Figure 4.2a). ATR-FTIR analyses of the sample solids retrieved from these experiments demonstrate bulk reductive transformation of birnessite into feitknechtite and manganite in the Mn(II)-birnessite experiment conducted at pH 7.5 (Figure A3.S1), consistent with our previous studies employing similar reaction conditions.^{86,120,142} As previously discussed and demonstrated,^{86,120,142} this transformation process involves initial transformation of birnessite (nominally MnO₂) into feitknechtite (β-MnOOH) according to $\text{Mn(II)} + \text{Mn(IV)O}_2 + 2 \text{H}_2\text{O} \rightarrow 2 \text{Mn(III)OOH} + 2\text{H}^+$ followed by conversion into manganite (γ-Mn(III)OOH). These transformations are readily monitored by ATR-FTIR through the growth and/or disappearance of characteristic feitknechtite IR bands at 1150, 1116, and 1087 cm⁻¹ and manganite IR bands at 1067 and 946 cm⁻¹ (Figure A3.S1), which are the bending modes of the structural OH groups inside the lattice of these minerals.

The kinetic sorption patterns of Ni(II) and Mn(II) in the ternary systems differ from those of the binary samples at both pH 6.5 and 7.5 (Figures 4.1 and 4.2). At pH 6.5, sorption of Ni(II) and Mn(II) is competitive, leading to lower amounts of Ni(II) and Mn(II) sorbed in the Ni(II)–Mn(II)-birnessite system than in the Ni(II)-birnessite and Mn(II)-birnessite samples. The increase in aqueous Ni(II) concentration immediately following Mn(II) introduction into the pH 6.5 birnessite suspensions (Figure 4.2a) indicates competitive displacement of Ni(II) from surface sites by Mn(II). At pH 7.5, sorption of Ni(II) is higher in the ternary system than in the binary experiment (Figure 4.2b), but lower for Mn(II) (Figure 4.1b); this indicates promotive effects for Ni(II) and inhibitive effects for Mn(II). The mechanisms behind these macroscopic sorption trends are addressed below based on the results of Ni K-edge XAS spectroscopy and XRD analyses.

4.3.2 XRD and ATR-FTIR results

Figure 4.3 displays the XRD patterns of reacted Mn-oxide solids obtained from the Ni(II)-birnessite and Ni(II)-Mn(II)-birnessite experiments, as well as the XRD patterns of reference materials: the birnessite starting substrate, Mn(III) phases (feitknechtite, manganite, hausmannite and Ni(II)-Mn(III)-LDH). At pH 6.5, the XRD patterns of the reacted substrates are nearly identical to that of the starting material, indicating a lack of mineralogical transformations of the birnessite sorbent at this pH. At pH 7.5, however, bulk transformations occur in the Ni(II)-Mn(II)-birnessite samples, evident by the appearance of new XRD reflections. Comparison to the reference XRD patterns suggests the formation of feitknechtite in these samples. However, a detailed inspection of the data (SI, Figure A3.S3) reveals distinct differences in the XRD patterns of the feitknechtite

formed between the ternary and binary samples. This suggests that Ni(II) affects the structure of this secondary Mn(III) phase. Interactions that may be involved include incorporation of Ni(II) into the feitknechtite structure, and adsorption of Ni(II) on the feitknechtite surface. To further characterize the impacts of Ni(II) on the secondary Mn(III) phases formed during Mn(II)-birnessite interactions at pH 7.5, ATR-FTIR analyses of the reacted Mn-oxide solids were performed. Figure 4.4 shows the ATR-FTIR spectra of six sorption samples reacted with 1000 μM Mn(II) in either the presence or absence of Ni(II) (50 or 200 μM) at pH 7.5. The Mn(II)-birnessite samples demonstrate the formation of feitknechtite, followed by conversion to manganite as discussed above. The formation of feitknechtite is observed from the sharp and well defined peaks at 1067 cm^{-1} and 946 cm^{-1} in the 5 d binary sample. Conversion of feitknechtite into manganite during long-term sorption is demonstrated by the 18 d Mn(II)-birnessite sample (Figure 4.4, spectrum f), which shows diminished feitknechtite bands relative to the 5 day sample, and pronounced new bands at 1150, 1116, and 1087 cm^{-1} that are due to manganite.¹⁵⁶ The IR spectra of the ternary samples that were pre-reacted with Ni(II) before addition of Mn(II) (spectra c-e in Figure 4.4) show no evidence for the presence of manganite, and exhibit notable changes in the spectral region of the feitknechtite OH bending modes, with the appearance of shoulders around 1000 cm^{-1} and 850 cm^{-1} that intensify with increasing Ni(II) inputs. These results are not only consistent with the XRD data but indicate impacts of Ni(II) on the structure of feitknechtite in these samples (Figure 4.4. In contrast, the ternary sample where feitknechtite was allowed to form prior to addition of Ni(II) to the reaction system shows no evidence for additional IR peaks and is identical to that of the 5 d binary Mn(II)-birnessite sample (Figure 4.4,

spectra a and b). This suggests that adsorption of Ni(II) onto the feitknechtite surface (Figure 4.4, spectrum b) does not produce the spectral changes observed for the ternary samples where birnessite undergoes reductive transformation in the presence of re-sorbed Ni(II) (Figure 4.4, spectra c-e). The most likely explanation for these changes is incorporation of Ni(II) into the lattice of secondary feitknechtite. Additional characterization of the Ni(II) speciation in these samples is provided by the Ni EXAFS results presented next.

4.3.3 Ni *K*-edge EXAFS results

The Ni *K* edge XAS of the binary and ternary sorption samples reacted at pH 6.5 and 7.5 are presented in Figure 4.5. Figure 4.5a shows the raw and fitted k^3 -weighted χ functions, while Figure 4.5b presents the corresponding radial structure functions (RSFs) obtained by Fourier transformation. The EXAFS fitting results are summarized in Table A3.S1. Inspection of the RSFs (Figure 4.5b) shows that the local coordination environment of sorbed Ni(II) is dominated by 2-3 coordination shells, centered near 1.6 Å, 2.4 Å and 3.1 Å (uncorrected for phase shift); an additional coordination shell, centered near 2.7 Å (uncorrected for phase shift), occurs for the ternary samples at pH 7.5. The first shell represents the O ligands in the first coordination sphere of the Ni(II) cations. It is fitted with 5-6 O atoms at a radial distance of ~ 2.05 Å (Table A3.S1), indicating that sorbed Ni(II) is in octahedral coordination with first-shell O.¹⁵⁵ The RSF peaks near 2.4 Å and 3.1 Å are Ni-Mn correlations,^{56–58,124,140,154,155} and are referred to here as Ni-Mn_A and Ni-Mn_B, respectively. The Ni-Mn_B shell is fitted at a radial distance of 3.49 Å (Table A3.S1). This correlation indicates inner-sphere coordination of Ni(II) to O ligands of Mn(III, IV) octahedra and occurs as “corner sharing” complexes at vacancies and particle

edges¹⁵⁵; the former complex is further described as a "triple corner-sharing" (^{TCS}Ni(II)) octahedron bound to three O atoms around a vacancy site, whereas the latter is characterized by Ni(II) adsorption complexes coordinated in a bridging bidentate fashion to two O atoms of structural Mn(IV) octahedra at particle edges.¹⁵⁵ The similar Ni-Mn distances for ^{TCS}Ni(II) and bidentate corner-sharing Ni(II) complexes at particle edges complicates distinction between these surface complexes on the basis of EXAFS results, and requires consideration of the intensity of the second-shell backscattering signal. Second shell Mn scattering is more pronounced for Ni(II) coordination at vacancy sites than at particles edges due to the difference in coordination number of second shell Mn between the two Ni(II) surface configurations ($CN_{Ni-Mn_B} = 6$ for Ni(II) coordination for ^{TCS}Ni(II), versus $CN_{Ni-Mn_B} = 2$ for Ni(II) bridging bidentate coordination at particle edges¹⁵⁵). Coordination of Ni(II) at vacancy sites predominates at low Ni(II) surface coverage, whereas bridging bidentate complexes gain importance as the Ni(II) surface loading increases beyond the layer vacancy content.¹⁵⁵

The radial distance of the Ni-Mn_A shell is fitted at 2.86 ± 0.01 Å for the ternary sorption samples at pH 6.5 (Table A3.S1). This distance is consistent with inner-sphere coordination of Ni(II) to Mn(III, IV) octahedra in an edge-sharing fashion.¹⁵⁵ This coordination occurs for Ni(II) atoms incorporated (^{INC}Ni(II)) into the octahedral birnessite mineral sheets, as well as for Ni(II) cations adsorbed at particle edges through coordination to two surface O atoms in a double-edge sharing configuration (^{DES}Ni(II)).¹⁵⁵ As with the corner-sharing complexes discussed above, distinguishing between ^{INC}Ni(II) and ^{DES}Ni(II) is feasible by considering the intensity for second-shell Mn scattering, which is more pronounced for the incorporated Ni(II) species (CN=6) than

for adsorbed Ni(II) (CN=2).¹⁵⁵ Gradual incorporation of Ni(II) has been observed during Ni(II)-birnessite interaction at alkaline pH,¹²² while ^{DES}Ni(II) complexes form at Ni(II) surface loadings exceeding the layer vacancy content.^{50,155}

The EXAFS data of the binary Ni(II)-birnessite samples show a pronounced Ni-Mn_B shell which is fitted at R=3.47 Å (Figure 4.5b; Table A3.S1). This indicates the predominance of corner-sharing Ni(II) complexes at the birnessite surface at both pH 6.5 and pH 7.5. The coordination numbers fitted for these shells are ~6 with Debye-Waller factors of ~0.01 Å (Table A3.S1). These values are consistent with the results of previous XAS studies assigning this shell to ^{TCS}Ni(II) complexes that cap birnessite layer vacancies.¹⁵⁵ This suggests that the Ni(II) surface speciation in the binary samples is dominated by Ni(II) adsorbed at layer vacancies.

The presence of Mn(II) in the ternary samples induces a notable change in the speciation of sorbed Ni(II) (Figure 4.5). At pH 6.5, introduction of Mn(II) leads to the formation of edge-sharing Ni(II) surface complexes, as shown by the appearance of Ni-Mn_A shells in the RSFs (Figure 4.5b), which are fitted at a radial distance of 2.86 Å (Table A3.S1). At pH 7.5, introduction of Mn(II) leads to formation of a Ni(II) complex with a fitted radial distance of 3.04-3.05 Å attributed to Ni-Mn_C (Table A3.S1). The XRD and FTIR data above shows that sorbed Ni(II) in these samples are associated with feitknechtite. These data, as discussed above, appear to suggest incorporation of Ni(II) into the feitknechtite structure. The evidently uniform Ni-Mn_C shell, with a relatively shorter radial distance than might be expected for a surface complex, is further suggestive of an incorporated Ni(II) species. However, in view of the “reverse ternary” Mn(II)-Ni(II)-birnessite sample (Figure 4.5b, spectrum j) which was fitted at 3.05 Å for Ni-Mn_C,

the current EXAFS data does not unambiguously rule out surface complexation on its own.

At pH 6.5, in ternary samples, Mn(II) displaces Ni(II) sorbed at vacancies then reacts with structural Mn(IV); the Mn(III) produced in this process drives Ni(II) to the particle edges reflected by the Ni-Mn_B peak in the RSF (Figure 4.5b, spectra d and g). As reported by Simanova et al.,¹⁵⁵ reduction of Mn(IV) at particle edges may also influence Ni(II) speciation, resulting the formation of a double edge sharing complexes at shorter radial distances than the triple corner sharing complexes observed in the Ni(II)-birnessite system. Such a complex may form on the residual birnessite in the system.

The impact on Ni speciation on birnessite is mimicked by the Good's buffers MES and HEPES as demonstrated in the SI (Figure A3.S5). In Figure A3.S5 we compare the k^3 -weighted χ functions (panel a) and their corresponding RSFs (panel b) obtained via Fourier Transformation in Figure A3.S5. This data was obtained from binary and ternary sorption samples exposed to Ni(II) and Mn(II) in the presence and absence of MES and HEPES at pH 6.5 and 7.5, respectively. Apparent in the RSFs at pH 6.5 for the Ni(II)-birnessite samples (Figure A3.S5, spectra a), the unbuffered sorption sample contains a single, Ni-Mn_B shell as discussed above. The sample exposed to MES buffer contains an additional Ni-Mn_A shell. In the ternary samples at pH 6.5, both samples yield essentially identical RSFs with Ni-Mn_A and Ni-Mn_B shells. It is therefore evident that these buffers mimic the effects of Mn(II). Simanova et al.¹⁵⁵ observed the same effect with HEPES buffer, attributing it to the piperazine-ring group as an electron donating source. MES buffer, evidently, has the same effect and may react with birnessite through the morpholino ring. At pH 7.5, comparison of the 2 day and 20 day binary samples shows

that the influence of the buffer is limited over the timecourse of these experiments, with no transformation towards Ni(II) associated feitknechtite observed. XRD data (not shown for the 20 day sample) further confirms that in the absence of Mn(II), exposure to buffer does not lead to bulk mineralogical transformation of birnessite.

At pH 7.5, introduction of Mn(II) into the reaction system has an impact on Ni(II) speciation that is distinct from pH 6.5 as evident by the single Ni-Mn_C shell with a fitted radial distance of 3.04 Å (Figure 4.5, spectra h and i). In this case, As discussed above, Ni(II) may be pushed to particle edges and may interact with residual birnessite. The RSF corresponding to the “reverse order” ternary sample (Figure 4.5b, spectrum j) has a the same Ni-Mn_C shell as the other pH 7.5 ternary samples fit at 3.05 Å. XRD data shows that some birnessite remains following five days of reaction for the ternary sample at pH 7.5 (Figure 4.3, pattern l); for the reverse ternary sample, the substrate has completely reacted to form feitknechtite (Figure A3.S2). Close inspection of the XRD patterns of the five day reacted samples for Mn(II)-birnessite, Mn(II)-Ni(II)-birnessite and Mn(II)-Ni(II)-birnessite (Figure A3.S3, patterns b-d) demonstrate similarities and differences that may further clarify the speciation evident by EXAFS. This XRD data demonstrates that when Mn(II) reacts with birnessite prior to addition of Ni(II), essentially the same pattern is produced as in the Mn(II)-birnessite system following 5 days of reaction (Figure A3.S3, patterns b and c). The “normal” ternary sorption sample, however, produces an XRD pattern with distinct shifts (Figure A3.S3, pattern d). This XRD data is consistent with the IR data discussed above (Figure 4.4) where structural incorporation is evident by the “normal” ternary sample spectra, but not in the “reverse” ternary sample spectrum. In view of the XRD and FTIR data, it seems that more than one Ni(II) species

may be produced in ternary systems, but these difference complexes are not resolved by EXAFS data presented here (Figure 4.5). The combined data suggests that both Ni(II) incorporation and surface complexation occur in these systems. The former species could explain why Ni(II) associated feitknechtite is inhibited from further conversion to manganite as occurs in the Mn(II)-birnessite system (Figure 4.3, patterns n and o; Figure 4.4, spectra e and f). In the absence of Ni(II), Mn(II) catalyzes conversion of metastable feitknechtite into manganite as previously discussed;^{86,120} Ni(II) sorption could inhibit this catalytic process.

Significant similarities for the Ni(II)-Mn(II)-birnessite system compared to Zn(II)-Mn(II)- birnessite are observed at pH 6.5 whereas pH 7.5 exhibits major differences. At pH 6.5, where Mn(II) does not induce bulk transformation of the substrate, competitive adsorption between the aqueous metals is observed. At pH 7.5, where Mn(II) induces transformation of the substrate, the Zn(II)-Mn(II)-birnessite system exhibits completely synergistic effects with enhanced removal of Zn(II) and Mn(II) concomitant with the formation of a $\text{Zn(II)}_{1-x}\text{Mn(II)}_x\text{Mn(III)}_2\text{O}_4$ spinel. Formation of this phase was shown to occur more rapidly than feitknechtite, due to the more effective trapping of reactive Mn^{3+} species produced via the interfacial electron transfer of Mn(II) to lattice Mn(IV) in birnessite. In the Ni(II)-Mn(II)-birnessite system, no such spinel analog is formed. Instead, Ni(II) appears to be inhibitory, lowering the overall removal of Mn(II) from solution and associating with the secondary feitknechtite phase and impeding conversion to manganite. These findings are consistent with early work performed by Hem et al.¹³⁰ which examined coprecipitation reactions of manganese oxides with copper, nickel and zinc. While Ni(II), Zn(II) and Mn(II) each have similar

atomic radii, their electronic d orbital structure may explain the behavior of these sorbates in the current study as well as our previous work where formation of a hetaerolite-like phase was demonstrated.¹⁴² The d orbital properties of Mn(II) and Zn(II) yield similar crystal field stabilization energies for tetrahedral coordination¹³⁰, whereas the d^8 configuration of Ni(II) restricts it to octahedral coordination.¹⁵⁷ Thus, Zn(II) may substitute Mn(II) in tetrahedral coordination in the spinel structure of Mn(II)Mn(III)₂O₄; Ni(II), would be more likely to substitute for Mn(III) in the same spinel structure. Evidently, Ni(II) has a greater propensity for substitution of Mn(III) in feitknechtite; Hem et al.¹⁵⁷ speculated that such a scenario would require charge compensation in the manganese oxide substrate by increasing the oxidation state of an equivalent amount of Mn(III) to Mn(IV) in the mineral structure. The reduced overall sorption of Mn(II) in the ternary system at pH 7.5 (Figure 4.1b) and concurrent inhibited conversion of feitknechtite to manganite (Figure 4.3), supports this possibility.

4.4 Environmental Implications

The solubility of trace metals is heavily influenced by Mn oxides like birnessite in the environment. Fluctuations in redox conditions can lead to structural modification and phase transformation of the initial substrate which can have consequences for any sorbed species. The data presented in this study demonstrate how Ni(II) treated birnessite impacts the speciation of Ni and Mn when the substrate is in contact with aqueous Mn(II). The speciation of Ni(II) is heavily dependent on pH with competitive effects with Mn(II) observed at pH 6.5, and enhanced sorption (of Ni(II)) observed at pH 7.5. Where transformation of the substrate occurs, Mn(II) initiates the formation of a Ni(II)-substituted feitknechtite phase via interfacial electron transfer between Mn(II) and structural Mn(IV).

Incorporation of Ni(II) in feitknechtite acts as an inhibitor of the Mn(II) catalyzed conversion to manganite. These findings merit consideration in the geochemistry of Ni and Mn in those geochemical systems where hexagonal birnessite is in contact with solutions containing significant levels of dissolved Mn(II) and Ni(II). Environments where neutral and alkaline conditions prevail may observe formation of this Ni(II) substituted feitknechtite phase, e.g. marine redoxclines. Environments wherein more acidic conditions prevail, as those surrounding acid mine drainage, will not observe this phase transformation. Additional studies on the long term stability of the Ni(II) substituted feitknechtite phase are required, in the presence and absence of Mn(II). Further characterization of sorption products in ternary systems containing Ni(II), Mn(II) and birnessite, is required to determine their impact on Ni and Mn solubility, Mn(IV) reactivity, and the fate of aqueous species.

4.5 FIGURES

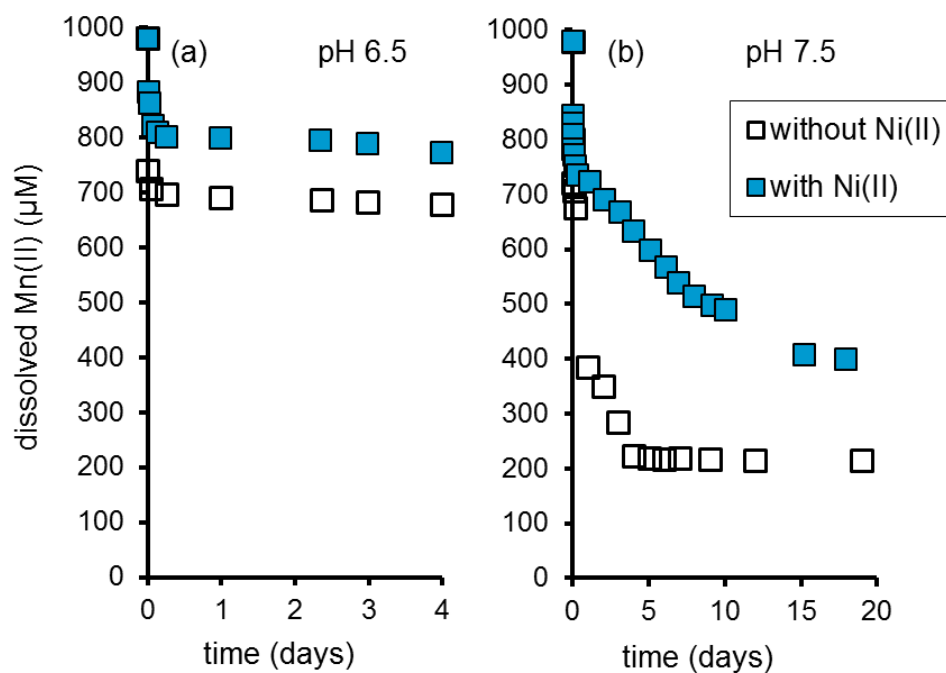


Figure 4.1 Time dependent removal of Mn(II) in binary and ternary experiments.

Aqueous Mn(II) concentration plotted as a function of time in binary (open squares) and ternary (closed squares) experiments at pH values of 6.5 (panel a) and 7.5 (panel b). Each experiment contained a birnessite suspension density of 0.1 g L^{-1} and an initial Mn(II) input of 1000 μM . In the ternary experiments, 200 μM Ni(II) was reacted with birnessite for two days prior to the addition of Mn(II). Corresponding time dependent Ni(II) sorption profiles are presented in Figure 4.2.

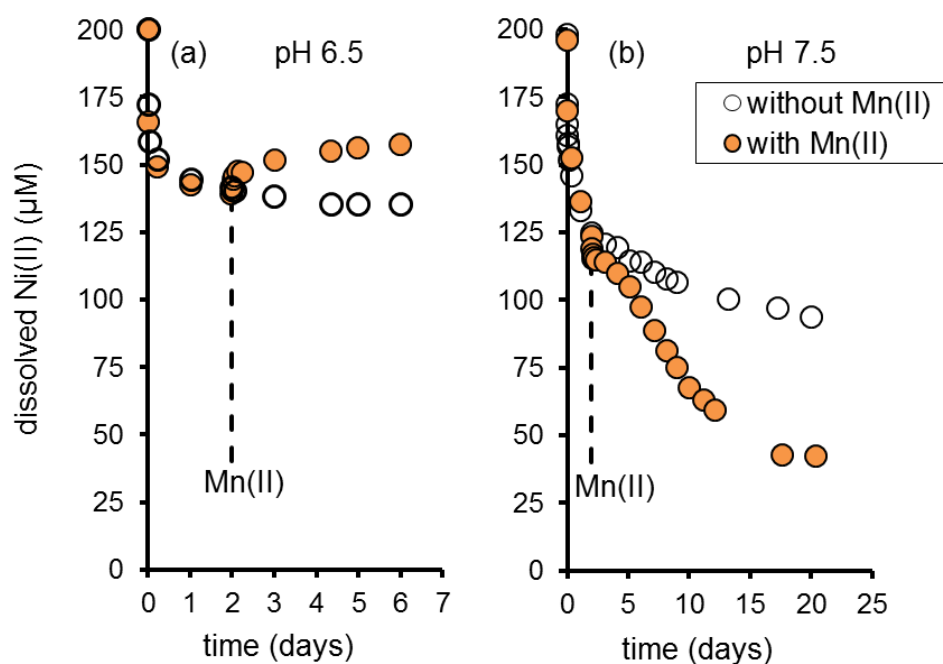


Figure 4.2 Time dependent removal of Ni(II) in binary and ternary experiments.

Aqueous Mn(II) concentration plotted as a function of time in binary (open circles) and ternary (closed circles) experiments at pH values of 6.5 (panel a) and 7.5 (panel b). Each experiment contained a birnessite suspension density of 0.1 g L^{-1} and an initial Ni(II) input of $200 \mu\text{M}$. In the ternary experiments, $1000 \mu\text{M}$ Mn(II) was added following two days of reaction between Ni(II) and birnessite, as indicated by the dashed line. The data presented for the ternary experiments here is the corresponding data to Figure 4.1.

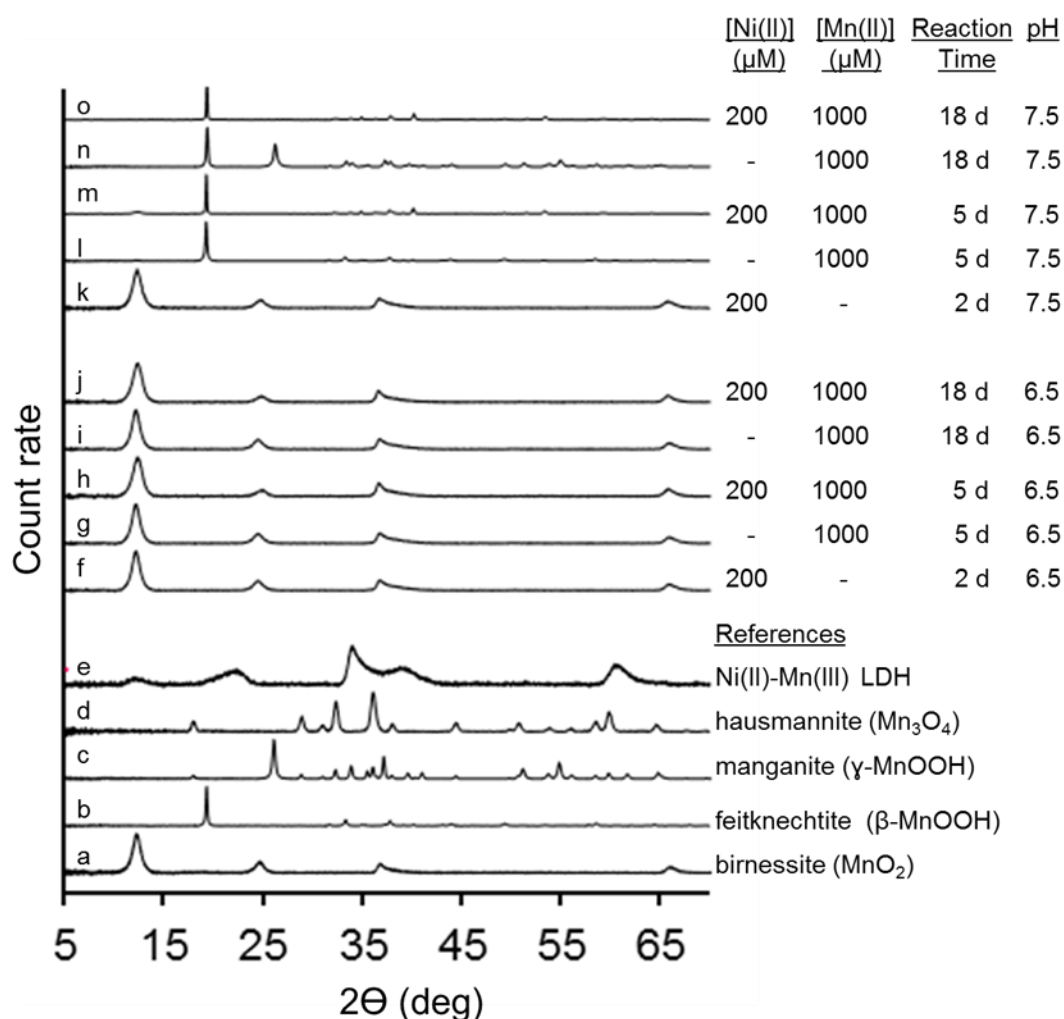


Figure 4.3 XRD patterns of sorption samples from binary and ternary experiments.

XRD patterns of reference samples (a-e) and sorption samples (f-o). Reference Mn-oxide patterns a-d are phases previously observed in systems containing hexagonal birnessite reacted with Mn(II) over the pH range 6.5-8.5, whereas pattern e is a layered double hydroxide containing Ni(II) and Mn(III). Binary sorption samples were obtained by reacting 0.1 g L^{-1} birnessite with either $200 \mu\text{M}$ Ni(II) for two days (patterns f and k) or $1000 \mu\text{M}$ Mn(II) (patterns l and n). Ternary sorption samples (patterns g, j, m and o) were treated with Ni(II) for two days followed by addition of $1000 \mu\text{M}$ Mn(II) for 5 or 18 days. Experimental conditions are summarized to the right of each pattern. Reaction times for ternary samples correspond to Mn(II).

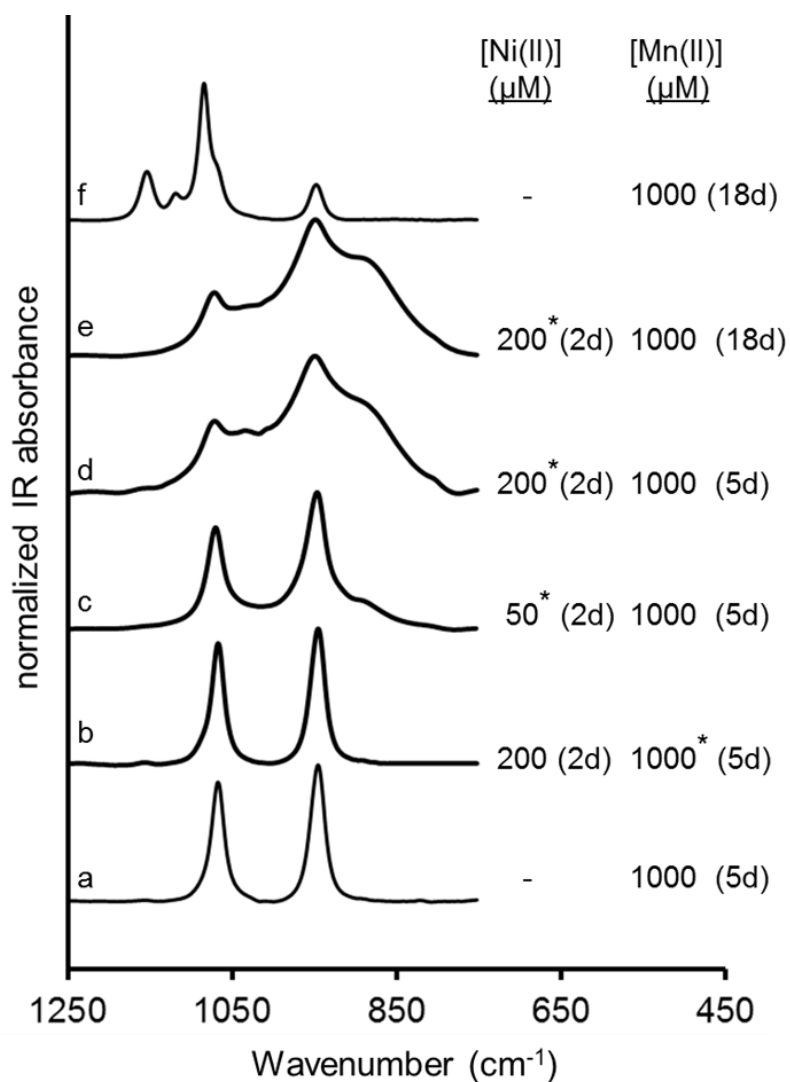


Figure 4.4 ATR-FTIR spectra of sorption samples from binary and ternary experiments

ATR-FTIR spectra of binary and ternary sorption products resulting from 0.1 g L^{-1} birnessite reacted with Ni(II) and/or Mn(II) under anoxic conditions at pH 7.5. The reaction conditions are summarized to the right of each spectrum, and the asterisk (*) for spectra b-e indicates which aqueous metal was added first. The reaction time with each metal is indicated in parentheses.

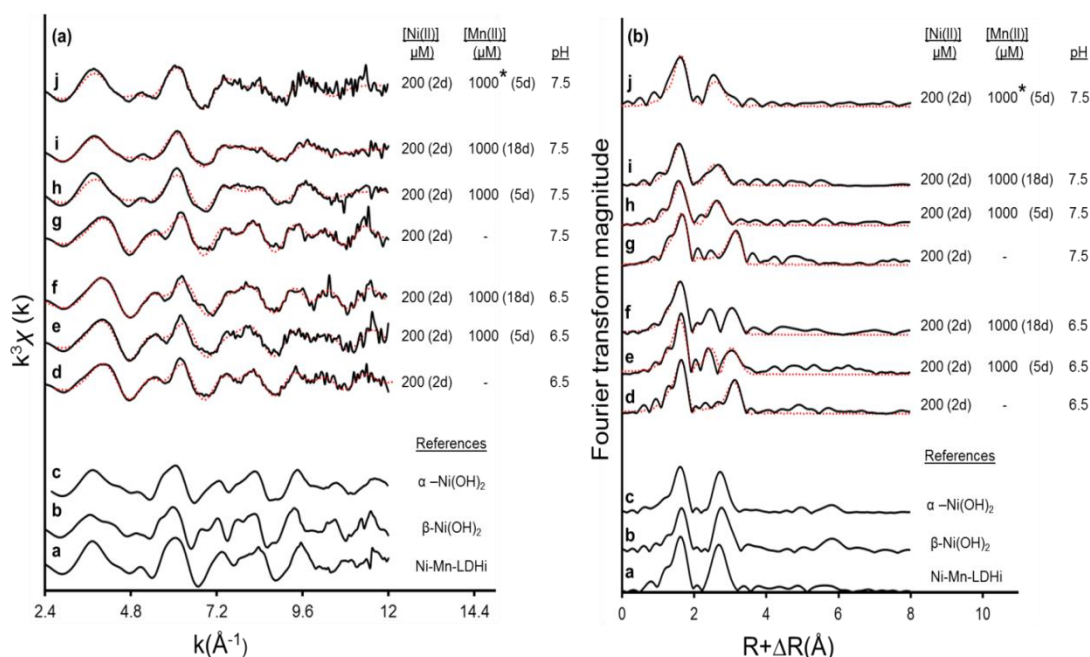


Figure 4.5 Ni K edge EXAFS data from samples from binary and ternary experiments. Ni K edge EXAFS data of anoxic birnessite (0.1 g L^{-1}) sorption samples reacted at pH 6.5 and 7.5 under binary and ternary reaction conditions, and reference samples: (a) k^3 -weighted χ functions. Raw spectra are shown in black, whereas shell fits to theoretical paths—further described in the text—are represented by red dotted lines. (b) Corresponding radial distribution functions. The conditions are summarized to the right of each spectrum, where reaction times are indicated in parentheses. For all ternary experiments, Ni(II) was added prior to addition of Mn(II), except in the case of sample j where the reaction sequence was reversed as indicated by the asterisk (*).

Chapter 5: Conclusions

5.1. General Conclusions

Evident from results presented in this dissertation, aqueous Mn(II) may be an important environmental reactant with birnessite that can strongly influence Mn oxide mineralogy. This is apparent from the results in Chapter 2 which demonstrated how Mn(II) can induce mineralogical transformation of birnessite at pH values greater or equal to 7. Mn(II) can react with birnessite to produce feitknechtite and manganite at pH 7-7.5. At pH 8-8.5, in addition to these Mn(III) oxy-hydroxides, reaction of Mn(II) with birnessite results in the transformation product hausmannite. For each of these possible outcomes, the reactions are essentially driven by the chemistry between sorbed Mn(II) and structural Mn(IV) in birnessite. In view of the competing transformation pathways occurring at pH 8-8.5, it is clear that, in addition to pH, the ratio of aqueous Mn(II) to solid Mn(IV) (in birnessite) is a controlling parameter in the final Mn oxide mineralogy. At pH values less than 7, transformation of birnessite is not observed, but significant comproportionation between Mn(II) and Mn(IV) appears to be ongoing. Thus, for what might be assumed to be a relatively simple system where Mn(II) and Mn(IV) in birnessite are the essential reactants, the results demonstrate that Mn(II)-birnessite interactions have great complexity.

Real world scenarios are typically even more complex than a binary system such as one containing Mn(II) and birnessite. Chapters 3 and 4 demonstrate how reaction systems involving Mn(II), birnessite and an additional divalent aqueous metal sorbate can produce complex mineralogical outcomes. Similar to the binary Mn(II)-birnessite system (Chapter 2) discussed above, transformation of pretreated Zn(II)-birnessite (Chapter 3)

and Ni(II)-birnessite (Chapter 4) substrates is observed at pH values greater-or-equal-to 7 when Mn(II) is added to the system. The transformation products observed in each of the reaction systems examined bear significant differences; as discussed above, the reaction system of Chapter 2 produced feitknechtite, manganite and hausmannite; the reaction system in Chapter 3 produced a hetaerolite-like phase that was kinetically favored over formation of the three phases observed in Chapter 2. In Chapter 4, a Ni(II) incorporated feitknechtite-like phase was observed and conversion to manganite was impeded.

In each of these studies (Chapters 2-4), Mn(II) sorption by birnessite was observed to be promoted with increasing pH. The pH boundaries of mineralogical transformation of the substrate were consistently observed at and above pH 7. Interfacial electron transfer between sorbed Mn(II) and structural Mn(IV) in birnessite is an important mechanism in these transformation pathways. This mechanism generates reactive Mn(III) species which can either disproportionate between Mn(II) and Mn(IV) or precipitate as insoluble Mn(III); in Chapter 2, precipitation of metastable feitknechtite is observed and this phase undergoes catalytic conversion in the presence of Mn(II) to the more stable polymorph, manganite. In Chapter 3, the presence of Zn(II) was shown to “trap” additional reactive Mn(III) that would otherwise disproportionate. In Chapter 4, the presence of Ni(II) was shown to inhibit the transformation pathway, presumably by blocking surface sites that Mn(II) would otherwise occupy. At lower pH values, competitive sorption was observed between Mn(II) and both Ni(II) and Zn(II).

The solubility of trace metals is heavily influenced by Mn oxides, particularly birnessite, in the environment. Variations in redox conditions can lead to structural modification and phase transformation of substrates which can have consequences for

sorbed species. The data presented in this thesis demonstrated how Ni(II) and Zn(II) treated birnessite impacts the speciation of Ni, Zn and Mn when the substrate is in contact with aqueous Mn(II). The speciation of Ni(II) and Zn(II) is heavily dependent on pH with competitive effects with Mn(II) observed at pH 6.5, and enhanced sorption (of Ni(II) and Zn(II)) observed at pH 7.5.

5.1. Environmental Significance

Factors that may impact the reductive transformation of birnessite by aqueous Mn(II) include, among others, pH, Eh, and the presence of sorbed impurities, such as Ni(II) and Zn(II); their influence on transformation pathways and the stability of products formed requires further study. In the work reported here, we began with a focus on the influence of pH, which is a key variable in determining metal adsorption processes⁸⁵, and may have a pronounced effect on occurring reactions. We examined the role of Mn(II) concentration at each pH value on secondary transformation pathways. Further we examined the impact of sorbed impurities, Zn(II) and Ni(II) on secondary transformation pathways as well as the sorption behavior of birnessite.

The potential importance of pH effects has been previously demonstrated⁸⁵; it was observed that the products formed during reaction of aqueous Mn^{2+} with birnessite were dependent on pH, with formation of nsutite, ramsdellite, cryptomelane, groutite, and manganite seen at pH 2.4, 4, 5, 6, and 8, respectively. However, these results were produced from experiments run at very high Mn(II) concentrations (3.3-330 mM), which makes extrapolation to natural systems uncertain.⁸⁵ Typical dissolved Mn concentrations in environmental settings are well below this range, e.g. less than 1 nM in surface and subsurface waters of the Southern Ocean;¹⁵⁸ higher levels at a maximum of 500 μM

Mn(II) have been observed in the suboxic zone of sediments in the Black Sea.¹⁵⁹ Systems with elevated levels of Mn(II), such as those affected by acid mine drainage (AMD), contain concentrations that are still below 3.3 mM. For example, Streams affected by AMD have been observed to contain 9.6 ppm (175 μ M) dissolved Mn(II) at the highest level¹⁶⁰. A highly contaminated site in Pinal Creek, AZ, contained 1.5 mM of dissolved Mn observed within the plume;¹⁶¹ within the hyporheic zone, the Mn(II) concentrations were reported to be below 1 mM. The current investigations focused on pH effects in systems with Mn(II) input concentrations and pH values that span ranges found in a variety of aquatic systems, including sites affected by AMD and marine sediments.

Our results also suggest that in environments defined by neutral and alkaline conditions, such as observed in marine redoxclines, precipitation of Zn(II)-Mn(III) phases can occur. In acid-mine drainage impacted systems, surface complexation of Zn(II) with Mn(IV) phyllosulfates are likely to dominate. Additional kinetic and thermodynamic studies pertaining to $\text{Zn(II)}_{1-x}\text{Mn(II)}_x\text{Mn(III)}_2\text{O}_4$ phases are required to assess their importance in natural systems as well as their impact on Zn(II) solubility. In consideration of the substantial formation of reactive Mn(III) at the surface of birnessite occurring within minutes of contact of the substrate with aqueous Mn(II), this (surface) Mn species suggests further refinement of the Mn redox cycle, particularly in suboxic environments. Their influence on the redox and sorption capacity of manganese towards reactants other than Zn(II), and their potential importance as a source of soluble Mn(III)^{134,135} requires further study.

Finally, Ni(II) treated birnessite can impact the speciation of Ni and Mn when the substrate is in contact with aqueous Mn(II). The speciation of Ni(II) is heavily dependent

on pH, consistent with the above observations, with competitive effects between the former species and Mn(II) observed at pH 6.5, and enhanced sorption (of Ni(II)) observed at pH 7.5. When transformation of the substrate is observed, Mn(II) initiates the formation of a Ni(II)-substituted feitknechtite phase via interfacial electron transfer between Mn(II) and structural Mn(IV). This incorporation of Ni(II) in feitknechtite evidently inhibits the Mn(II) catalyzed conversion to manganite. Such findings suggest that reconsideration of the geochemistry of Ni and Mn in relevant systems, as discussed above, are required. Similar to Zn, those environments where neutral and alkaline conditions prevail formation of this Ni(II) substituted feitknechtite phase, e.g. marine redoxclines, may occur. In environments that are more acidic, such as those surrounding acid mine drainage sites, will not observe this phase transformation and Ni(II) surface complexation will dominate. Further studies to determine the long term stability of the long term stability of the Ni(II) substituted feitknechtite phase are required, in the presence and absence of Mn(II). Additionally, the sorption products found in ternary systems containing Ni(II), Mn(II) and birnessite require more refined characterization to resolve the Ni speciation as well as to determine their impact on Ni and Mn solubility, Mn(IV) reactivity, and the fate of aqueous species.

5.2. Future Research

Real world scenarios involving birnessite and aqueous metals in solution are expected to be characterized by greater complexity than one or two sorbates as examined in this thesis. The following list represents possible future research to be performed:

1. Multisorbate systems containing birnessite, Mn(II), Zn(II), Ni(II).

2. Examination of aqueous metal sequence addition on macroscopic sorption behavior and transformation of birnessite.
3. Examination of the role of the transformation products of birnessite as induced by Mn(II), e.g., feitknechtite, manganite, and haussmanite on sorption of Mn(II), Ni(II), Zn(II) and other aqueous metal sorbates.
4. Long term stability of the metal oxides observed in the systems of this thesis.
5. Further comparison of buffered and unbuffered systems.
6. Comparison of Mn(II)-birnessite interactions in the presence and absence of organic matter.
7. Examination of Mn(II)-birnessite interactions in the presence and absence of As, Se, and U.
8. Comparison of the role of vacancies on Mn(II)-birnessite interactions and competing metals.
9. Examination of Mn(II)-birnessite interactions in the presence and absence of competing redox active metals, such as Co.

References

- (1) Borch, T.; Kretzschmar, R.; Kappler, A.; Cappellen, P. Van; Ginder-Vogel, M.; Voegelin, A.; Campbell, K. Biogeochemical redox processes and their impact on contaminant dynamics. *Environ. Sci. Technol.* **2010**, *44*, 15–23.
- (2) Burdige, D. J.; Nealson, K. H. Chemical and microbiological studies of sulfide-mediated manganese reduction • mediated manganese reduction 1. *Geomicrobiol. J.* **1986**, *4*, 361.
- (3) Neretin, L. N.; Pohl, C.; Jost, G.; Leipe, T.; Pollehne, F. Manganese cycling in the Gotland Deep, Baltic Sea. *Mar. Chem.* **2003**, *82*, 125–143.
- (4) Oguz, T.; Murray, J. W.; Callahan, A. E. Modeling redox cycling across the suboxic-anoxic interface zone in the Black Sea. *Deep. Res. Part I-Oceanographic Res. Pap.* **2001**, *48*, 761–787.
- (5) Morgan, J. J.; Stumm, W. The role of multivalent metal oxides in limnological transformations, as exemplified by iron and manganese. In *Proceedings of the international conference of the international association on water pollution research*; 1965; Vol. 2, pp. 103–131.
- (6) Lafferty, B. J.; Ginder-vogel, M.; Sparks, D. L.; Zhu, M.; Livi, K. J. T. Arsenite oxidation by a poorly crystalline manganese-oxide. 2. results from x-ray absorption spectroscopy and x-ray diffraction. *Environ. Sci. Technol.* **2010**, *44*, 8467–8472.
- (7) Scott, M. J.; Morgan, J. J. Reactions at Oxide Surfaces .1. Oxidation of As(III) by Synthetic Birnessite. *Environ. Sci. Technol.* **1995**, *29*, 1898–1905.
- (8) Weaver, R. M., Hochella, Jr., M. F. The reactivity of seven Mn-oxides with $\text{Cr}_{\text{aq}}^{3+}$: A comparative analysis of a complex, environmentally important redox reaction. *Am. Miner.* **2003**, *88*, 2016–2027.
- (9) Balistrieri, L. S.; Chao, T. T. Adsorption of selenium by amorphous iron oxyhydroxide and manganese dioxide. *Geochim. Cosmochim. Acta* **1990**, *54*, 739–751.
- (10) Scott, M. J.; Morgan, J. J. Reactions at oxide surfaces. 2. Oxidation of Se(IV) by synthetic birnessite. *Environ. Sci. Technol.* **1996**, *30*, 1990–1996.
- (11) Post, J. E. Crystal structure determinations of synthetic sodium, magnesium, and potassium birnessite using TEM and Rietveld method. **1990**, *75*, 477–489.
- (12) Morgan, J. J. Manganese in natural waters and earth's crust: its availability to organisms. *Met. Ions Biol. Syst.* **2000**, *37*, 1–34.

- (13) Stumm, W.; Morgan, J. J. *Aquatic Chemistry: chemical equilibria and rates in natural waters*; John Wiley & Sons: New York, NY, 1965.
- (14) Morgan, J. J. Kinetics of reaction between O₂ and Mn(II) species in aqueous solutions. *Geochim. Cosmochim. Acta* **2005**, *69*, 35–48.
- (15) Mandernack, K. W.; Post, J.; Tebo, B. M. Manganese mineral formation by bacterial-spores of the marine bacillus, strain SG1: Evidence for the direct oxidation of Mn(II) to Mn(IV). *Geochim. Cosmochim. Acta* **1995**, *59*, 4393–4408.
- (16) Miyata, N.; Sugiyama, D.; Tani, Y.; Tsuno, H.; Seyama, H.; Sakata, M.; Iwahori, K. Production of biogenic manganese oxides by repeated-batch cultures of laboratory microcosms. *J. Biosci. Bioeng.* **2007**, *103*, 432–439.
- (17) Nealson, K. H.; Tebo, B. M.; Rosson, R. A. Occurrence and mechanisms of microbial oxidation of manganese. *Adv. Appl. Microbiol.* **1986**, *33*, 280–318.
- (18) Santelli, C. M.; Webb, S. M.; Dohnalkova, A. C.; Hansel, C. M. Diversity of Mn oxides produced by Mn(II)-oxidizing fungi. *Geochim. Cosmochim. Acta* **2011**, *75*, 2762–2776.
- (19) Saratovsky, I.; Wightman, P. G.; Pasten, P. A.; Gaillard, J.-F. ; Poeppelmeier, K. R.; Pastén, P. A. Manganese oxides: Parallels between abiotic and biotic structures. *J. Am. Chem. Soc.* **2006**, *128*, 11188–11198.
- (20) Spiro, T. G.; Bargar, J. R.; Sposito, G.; Tebo, B. M. Bacteriogenic manganese oxides. *Acc.Chem. Res.* **2010**, *43*, 2–9.
- (21) Tebo, B. M. Manganese(II) Oxidation in the Suboxic Zone of the Black-Sea. *Deep. Res. Part A-Oceanographic Res. Pap.* **1991**, *38*, S883–S905.
- (22) Tebo, B. M.; Bargar, J. R.; Clement, B. G.; Dick, G. J.; Murray, K. J.; Parker, D.; Verity, R.; Webb, S. M. Biogenic manganese oxides: properties and mechanisms of formation. *Annu. Rev. Earth Planet. Sci.* **2004**, *32*, 287–328.
- (23) Villalobos, M., Lanson, B. Manceau, A., Toner, B., and Sposito, G. Structural model for the biogenic Mn oxide produced by *Pseudomonas putida*. *Am. Miner.* **2006**, *91*, 489–502.
- (24) Webb, S. M.; Dick, G. J.; Bargar, J. R.; Tebo, B. M. Evidence for the presence of Mn(III) intermediates in the bacterial oxidation of Mn(II). *Proc. Natl. Acad. Sci. U. S. A.* **2005**, *102*, 5558–5563.
- (25) Hastings, D.; Emerson, S. Oxidation of Manganese by Spores of a Marine Bacillus - Kinetic and Thermodynamic Considerations. *Geochim. Cosmochim. Acta* **1986**, *50*, 1819–1824.

- (26) Hem, J. D. Chemistry of manganese in natural water. *USGS*, 1963, A1–A64.
- (27) Morgan, J. J.; Stumm, W. Oxygenation of manganese in aqueous systems. In *American Chemical Society*; American Chemical Society, 1963; pp. 13–16.
- (28) Morgan, J. J. Chemical Equilibria and Kinetic Properties of Manganese in Natural Waters. In *Principles and Applications of Water Chemistry*; Faust, S. D.; Hunter, J. V, Eds.; 1965; pp. 561–624.
- (29) Wilson, D. E. Surface and complexation effects on the rate of Mn(II) oxidation in natural waters. *Geochim. Cosmochim. Acta* **1980**, *44*, 1311–1317.
- (30) Golden, D. C.; Chen, C. C.; Dixon, J. B.; Tokashiki, Y. Pseudomorphic Replacement of Manganese Oxides by Iron-Oxide Minerals. *Geoderma* **1988**, *42*, 199–211.
- (31) Postma, D. Concentration of Mn and Separation from Fe in Sediments. 1. Kinetics and Stoichiometry of the Reaction between Birnessite and Dissolved Fe(II) at 10 °C. *Geochim. Cosmochim. Acta* **1985**, *49*, 1023–1033.
- (32) Dellwig, O.; Leipe, T.; März, C.; Glockzin, M.; Pollehne, F.; Schnetger, B.; Yakushev, E. V.; Böttcher, M. E.; Brumsack, H.-J. H.-J.; Maerz, C.; et al. A new particulate Mn-Fe-P-shuttle at the redoxcline of anoxic basins. *Geochim. Cosmochim. Acta* **2010**, *74*, 7100–7115.
- (33) Waite, T. D.; Wrigley, I. C.; Szymczak, R. Photoassisted Dissolution of a Colloidal Manganese Oxide in the Presence of Fulvic-Acid. *Environ. Sci. Technol.* **1988**, *22*, 778–785.
- (34) Stone, A. T.; Morgan, J. J. Reduction and Dissolution of Manganese(III) and Manganese(IV) Oxides by Organics: 1. Reaction with hydroquinone, *18*, 617–624.
- (35) Stone, A. T.; Morgan, J. J. Reduction and Dissolution of Manganese(III) and Manganese(IV) Oxides by Organics: 2. Survey. of the Reactivity of organics. *Environ. Sci. Technol.* **1984**, *18*, 450–456.
- (36) Sunda, W. G.; Kieber, D. J. Oxidation of humic substances by manganese oxides yields low-molecular-weight organic substrates. *Nature* **1994**, *367*, 62.
- (37) Wang, Y.; Stone, A. T. The citric acid-Mn(III,IV)O₂ (birnessite) reaction. Electron transfer, complex formation, and autocatalytic feedback. *Geochim. Cosmochim. Acta* **2006**, *70*, 4463–4476.
- (38) Wang, Y.; Stone, A. T. Reaction of Mn(III,IV) (hydr)oxides with oxalic acid, glyoxylic acid, phosphonoformic acid, and structurally-related organic compounds. *Geochim. Cosmochim. Acta* **2006**, *70*, 4477–4490.

- (39) Godfredsen, K. L.; Stone, A. T. Solubilization of Manganese Dioxide-Bound Copper by Naturally-Occurring Organic-Compounds. *Environ. Sci. Technol.* **1994**, *28*, 1450–1458.
- (40) Sunda, W. G.; Huntsman, S. A. Photoreduction of manganese oxides in seawater. *Mar. Chem.* **1994**, *46*, 133–152.
- (41) Kwon, K. D.; Refson, K.; Sposito, G. On the role of Mn(IV) vacancies in the photoreductive dissolution of hexagonal birnessite. *Abstr. Pap. Am. Chem. Soc.* **2009**, *73*, 4142–4150.
- (42) Post, J. E. Manganese oxide minerals: crystal structures and economic and environmental significance. *Proc. Natl. Acad. Sci. U. S. A.* **1999**, *96*, 3447–3454.
- (43) Villalobos, M.; Toner, B.; Bargar, J.; Sposito, G. Characterization of the manganese oxide produced by *Pseudomonas putida* strain MnB1. *Geochim. Cosmochim. Acta* **2003**, *67*, 2649–2662.
- (44) Bargar, J. R.; Webb, S. M.; Tebo, B. M. EXAFS, XANES and in-situ SR-XRD characterization of biogenic manganese oxides produced in sea water. *Phys. Scr.* **2005**, *T115*, 888–890.
- (45) Bargar, J. R.; Webb, S. M.; Fullers, C. C.; Tebo, B. M. Structural chemistry, reactivity, and environmental occurrence of bacteriogenic manganese oxides. *Abstr. Pap. Am. Chem. Soc.* **2005**, *229*, U784–U784.
- (46) Manning, B. A.; Fendorf, S. E.; Bostick, B.; Suarez, D. L. Arsenic(III) oxidation and arsenic(V) adsorption reactions on synthetic birnessite. *Environ. Sci. Technol.* **2002**, *36*, 976–981.
- (47) Pal, S.; Bollag, J.-M.; Huang, P. M. Role of abiotic and biotic catalysts in the transformation of phenolic compounds through oxidative coupling reactions. *Soil. Biol. Biochem* **1994**, *26*, 813–8120.
- (48) McKenzie, R. M. Manganese oxides and hydroxides. In *Minerals in Soil Environments*; Dixon, J. B., Weed, S. B., Ed.; Soil Sci. Soc. Am. Book Ser.: Madison, 1989; pp. 439–465.
- (49) Lanson, B.; Drits, V. A.; Silvester, E.; Manceau, A. Structure of H-exchanged hexagonal birnessite and its mechanism of formation from Na-rich monoclinic busserite at low pH. *Am. Miner.* **2000**, *85*, 826–838.
- (50) Bodeř, S.; Manceau, A.; Geoffroy, N.; Baronnet, A.; Buatier, M. Formation of todorokite from vernadite in Ni-rich hemipelagic sediments. *Geochim. Cosmochim. Acta* **2007**, *71*, 5698–5716.
- (51) Gray, M. J.; Malati, M. A. The adsorption of lead and other heavy metals on

- oxides of manganese and iron. *J. Chem. Tech. Biotechnol.* **1979**, 29, 135–144.
- (52) Manceau, A.; Gorshkov, A. I.; Drits, V. A. Structural Chemistry of Mn, Fe, Co, and Ni in manganese hydrous oxides: Part II. Information from EXAFS spectroscopy and electron and X-ray diffraction. *Am. Miner.* **1992**, 77, 1144–1157.
- (53) Gaillot, A. C.; Flot, D.; Drits, V. A.; Manceau, A.; Burghammer, M.; Lanson, B. Structure of synthetic K-rich birnessite obtained by high-temperature decomposition of KMnO_4 . I. Two-layer polytype from 800 °C experiment. *Chem. Mater.* **2003**, 15, 4666–4678.
- (54) Matocha, C. J.; Elzinga, E. J.; Sparks, D. L. Reactivity of Pb(II) at the Mn(III,IV) (oxyhydr)oxide–water interface. *Environ. Sci. Technol.* **2001**, 35, 2967–2972.
- (55) McKenzie, R. M. The adsorption of lead and other heavy metals on oxides of manganese and iron. *Aust. J. Soil Res.* **1980**, 18, 61–73.
- (56) Peacock, C. L.; Sherman, D. M. Sorption of Ni by birnessite: equilibrium controls on Ni in seawater. *Chem. Geol.* **2007**, 238, 94–106.
- (57) Peacock, C. L. Physiochemical controls on the crystal-chemistry of Ni in birnessite: Genetic implications for ferromanganese precipitates. *Geochim. Cosmochim. Acta* **2009**, 73, 3568–3578.
- (58) Pena, J.; Kwon, K. D.; Refson, K.; Bargar, J. R.; Sposito, G.; Peña, J. Mechanisms of nickel sorption by a bacteriogenic birnessite. *Geochim. Cosmochim. Acta* **2010**, 74, 3076–3089.
- (59) Toner, B.; Manceau, A.; Webb, S. M.; Sposito, G. Zinc sorption to biogenic hexagonal-birnessite particles within a hydrated bacterial biofilm. *Geochim. Cosmochim. Acta* **2006**, 70, 27–43.
- (60) Sherman, D. M.; Peacock, C. L. Surface complexation of Cu on birnessite δ - MnO_2 : Controls on Cu in the deep ocean. *Geochim. Cosmochim. Acta* **2010**, 74, 6721–6730.
- (61) Dyer, A.; Pillinger, M.; Harjula, R.; Amin, S. Sorption characteristics of radionuclides on synthetic birnessite-type layered manganese oxides. *J. Mater. Chem.* **2000**, 10, 1867–1874.
- (62) Fredrickson, J. K.; Zachara, J. M.; Kennedy, D. W.; Liu, C. X.; Duff, M. C.; Hunter, D. B.; Dohnalkova, A. Influence of Mn oxides on the reduction of uranium(VI) by the metal-reducing bacterium *Shewanella putrefaciens*. *Geochim. Cosmochim. Acta* **2002**, 66, 3247–3262.
- (63) Han, X.; Li, Y.-L.; Gu, J.-D. Oxidation of As(III) by MnO_2 in the absence and presence of Fe(II) under acidic conditions. *Geochim. Cosmochim. Acta* **2011**, 75,

368–379.

- (64) Parikh, S. J.; Lafferty, B. J.; Meade, T. G.; Sparks, D. L.; Lafferty, B. J. Evaluating Environmental Influences on As(III) Oxidation Kinetics by a Poorly Crystalline Mn-Oxide. *Environ. Sci. Technol.* **2010**, *44*, 3772–3778.
- (65) Tournassat, C.; Charlet, L.; Bosbach, D.; Manceau, A. Arsenic(III) oxidation by birnessite and precipitation of manganese(II) arsenate. *Environ. Sci. Technol.* **2002**, *36*, 493–500.
- (66) Zhu, M.; Paul, K. W.; Kubicki, J. D.; Sparks, D. L. Quantum Chemical Study of Arsenic (III,V) Adsorption on Mn-Oxides: Implications for Arsenic(III) Oxidation. *Environ. Sci. Technol.* **2009**, *43*, 6655–6661.
- (67) Banerjee, D.; Nesbitt, H. W. Oxidation of aqueous Cr(III) at birnessite surfaces: Constraints on reaction mechanism. *Geochim. Cosmochim. Acta* **1999**, *63*, 1671–1687.
- (68) Dai, R.; Liu, J.; Yu, C.; Sun, R.; Lan, Y.; Mao, J. D. A comparative study of oxidation of Cr(III) in aqueous ions, complex ions and insoluble compounds by manganese-bearing mineral (birnessite). *Chemosphere* **2009**, *76*, 536–541.
- (69) Fendorf, S. E.; Fendorf, M.; Sparks, D. L.; Gronsky, R. Inhibitory Mechanisms of Cr(III) Oxidation by δ -MnO₂. *J. Colloid Interface Sci.* **1992**, *153*, 37–54.
- (70) Kim, J. G.; Dixon, J. B.; Chusuei, C. C.; Deng, Y. J. Oxidation of chromium(III) to (VI) by manganese oxides. *Soil Sci. Soc. Am. J.* **2002**, *66*, 306–315.
- (71) Oze, C.; Bird, D. K.; Fendorf, S. Genesis of hexavalent chromium from natural sources in soil and groundwater. *Proc. Natl. Acad. Sci. U. S. A.* **2007**, *104*, 6544–6549.
- (72) Banerjee, D.; Nesbitt, H. W. XPS study of reductive dissolution of birnessite by H₂SeO₃ with constraints on reaction mechanism. *Am. Miner.* **2000**, *85*, 1328.
- (73) Pizzigallo, M. D. R.; Napola, A.; Spagnuolo, M.; Ruggiero, P. Mechanochemical removal of organo-chlorinated compounds by inorganic components of soil. *Chemosphere* **2004**, *55*, 1485–1492.
- (74) Jeng, H. A.; Pan, C.-H.; Diawara, N.; Chang-Chien, G.-P.; Lin, W.-Y.; Huang, C.-T.; Ho, C.-K.; Wu, M.-T. Polycyclic aromatic hydrocarbon-induced oxidative stress and lipid peroxidation in relation to immunological alteration. *Occup. Environ. Med.* **2011**, *68*, 653–658.
- (75) Jung, J.-W.; Lee, S.; Ryu, H.; Nam, K.; Kang, K.-H. Enhanced reactivity of hydroxylated polycyclic aromatic hydrocarbons to birnessite in soil: Reaction kinetics and nonextractable residue formation. *Environ. Toxicol. Chem.* **2008**, *27*,

1031–1038.

- (76) Jung, J.-W.; Lee, S.; Ryu, H.; Kang, K.-H.; Nam, K. Detoxification of phenol through bound residue formation by birnessite in soil: Transformation kinetics and toxicity. *J. Environ. Sci. Heal. Part A-Toxic/hazardous Subst. Environ. Eng.* **2008**, *43*, 255–261.
- (77) Keith, L. H.; Telliard, W. A. Priority pollutants: 1--A perspective view. *Environ. Sci. Technol.* **1979**, *13*.
- (78) Lee, S.; Ryu, H.; Nam, K. Phenanthrene Metabolites Bound to Soil Organic Matter by Birnessite Following Partial Biodegradation. *Environ. Toxicol. Chem.* **2009**, *28*, 946–952.
- (79) Russo, F.; Rao, M. A.; Gianfreda, L. Bioavailability of phenanthrene in the presence of birnessite-mediated catechol polymers. *Appl. Microbiol. Biotechnol.* **2005**, *68*, 131–139.
- (80) Jokic, A.; Frenkel, A. I.; Vairavamurthy, M. A.; Huang, P. M. Birnessite catalysis of the Maillard reaction: Its significance in natural humification. *Geophys. Res. Lett.* **2001**, *28*, 3899–3902.
- (81) Shindo, H. and Huang, P. M. Role of Mn(IV) oxide in abiotic formation of humic substances in the environment. *Nature* **1982**, *298*, 363–365.
- (82) Wang, M. C., and Huang, P. M. Significance of Mn(IV) oxide in the abiotic ring cleavage of pyrogallol in natural environments. *Sci. Total Environ.* **1992**, *113*, 147–157.
- (83) Shindo, H.; Huang, P. M. Significance of Mn(IV) oxide in abiotic formation of organic nitrogen complexes in natural environments. *Nature* **1984**, *308*, 57–59.
- (84) Kang, K. H.; Dec, J.; Park, H.; Bollag, J. M. Effect of phenolic mediators and humic acid on cyprodinil transformation in presence of birnessite. *Water Res.* **2004**, *38*, 2737–2745.
- (85) Tu, S., Racz, G. J., and Goh, T. B. Transformations of synthetic birnessite as affected by pH and manganese concentration. *Clays Clay Miner.* **1994**, *42*, 321–330.
- (86) Elzinga, E. J. Reductive transformation of birnessite by aqueous Mn(II). *Environ. Sci. Technol.* **2011**, *45*, 6366–6372.
- (87) Zhu, M.; Ginder-Vogel, M.; Parikh, S. J.; Feng, X.-H.; Sparks, D. L. Cation effects on the layer structure of biogenic Mn-oxides. *Environ. Sci. Technol.* **2010**, *44*, 4465–4471.

- (88) Feng, X. H.; Zhu, M.; Ginder-Vogel, M.; Ni, C.; Parikh, S. J.; Sparks, D. L. Formation of nano-crystalline todorokite from biogenic Mn oxides. *Geochim. Cosmochim. Acta* **2010**, *74*, 3232–3245.
- (89) Fuller, C. C.; Bargar, J. R. Processes of Zinc Attenuation by Biogenic Manganese Oxides Forming in the Hyporheic Zone of Pinal Creek, Arizona. **2014**.
- (90) Hochella, Jr., M. F. Mineral surfaces: their characterization and their chemical physical and reactive nature. In *Mineral surfaces*; 1995; Vol. 5, pp. 17–60.
- (91) Manceau, A.; Tamura, N.; Celestre, R. S.; MacDowell, A. A.; Geoffroy, N.; Sposito, G.; Padmore, H. A. Molecular-scale speciation of Zn and Ni in soil ferromanganese nodules from loess soils of the Mississippi Basin. *Environ. Sci. Technol.* **2003**, *37*, 75–80.
- (92) Marcus, M.; Manceau, A.; Kersten, M. Mn, Fe, Zn and As speciation in a fast-growing ferromanganese marine nodule. *Geochim. Cosmochim. Acta* **2004**, *68*, 3125–3136.
- (93) Perez-Benito, J. F. Reduction of colloidal manganese dioxide by manganese(II). *J. Colloid Interface Sci.* **2002**, *248*, 130–135.
- (94) Villalobos, M.; Bargar, J.; Sposito, G. Trace metal retention on biogenic manganese oxide nanoparticles. *Elements* **2005**, *1*, 223–226.
- (95) Chang, J.; Tani, Y.; Naitou, H.; Miyata, N.; Tojo, F.; Seyama, H. Zn(II) sequestration by fungal biogenic manganese oxide through enzymatic and abiotic processes. *Chem. Geol.* **2014**, *383*, 155–163.
- (96) Webb, S. M.; Tebo, B. M.; Bargar, J. R. Structural characterization of biogenic Mn oxides produced in seawater by the marine bacillus sp strain SG-1. *Am. Miner.* **2005**, *90*, 1342–1357.
- (97) Grangeon, S.; Lanson, B.; Miyata, N.; Tani, Y.; Manceau, A. Structure of nanocrystalline phyllomanganates produced by freshwater fungi. *Am. Mineral.* **2010**, *95*, 1608–1616.
- (98) Manceau, A.; Lanson, B.; Drits, V. A.; Structure of heavy metal sorbed birnessite. Part III: Results from powder and polarized extended X-ray absorption fine structure spectroscopy. *Geochim. Cosmochim. Acta* **2002**, *66*, 2639–2663.
- (99) Webb, S. M.; Tebo, B. M.; Bargar, J. R.; Fuller, C. C. Structural influences of sodium and calcium ions on the biogenic manganese oxides produced by the marine *Bacillus* sp., strain SG-1. *Environ. Sci. Technol.* **2005**, *T115*, 181–193.
- (100) Pankow, J. F.; Morgan, J. J. Kinetics for the aquatic environment. *Environ. Sci. Technol.* **1981**, *15*, 1155–1164.

- (101) Bargar, J. R. Biotic and abiotic products of Mn(II) oxidation by spores of the marine *Bacillus* sp. strain SG-1. *Am. Mineral.* **2005**, *90*, 143–154.
- (102) Learman, D. R.; Wankel, S. D.; Webb, S. M.; Martinez, N.; Madden, A. S.; Hansel, C. M. Coupled biotic–abiotic Mn(II) oxidation pathway mediates the formation and structural evolution of biogenic Mn oxides. *Geochim. Cosmochim. Acta* **2011**, *75*, 6048–6063.
- (103) Scheidegger, A. M.; Sparks, D. L. A critical assessment of sorption-desorption mechanisms at the soil mineral/water interface. *Soil Sci.* **1996**, *161*, 813–831.
- (104) Brown, G. E.; Henrich, V. E.; Casey, W. H.; Clark, D. L.; Eggleston, C.; Felmy, A.; Goodman, D. W.; Grätzel, M.; Maciel, G.; McCarthy, M. I. Metal oxide surfaces and their interactions with aqueous solutions and microbial organisms. *Chem. Rev.* **1999**, *99*, 77–174.
- (105) Diem, D.; Stumm, W. Is dissolved Mn^{2+} being oxidized by O_2 in absence of Mn-bacteria or surface catalysts? *Geochim. Cosmochim. Acta* **1984**, *48*, 1571–1573.
- (106) Gustafsson, J. P. Visual MINTEQ, 2006.
- (107) Papers, S.; Burle, E.; Kirby-Smith, W. Application of formaldoxime colorimetric method for the determination of manganese in the pore water of anoxic estuarine sediments. *Estuaries and Coasts* **1979**, *2*, 198–201.
- (108) Sparks, D. L. Toxic metals in the environment: The role of surfaces. *Elements* **2005**, *1*, 193–197.
- (109) Lanson, B.; Drits, V. A.; Gaillot, A.-C.; Silvester, E. Plançon, A.; Manceau, A. Structure of heavy-metal sorbed birnessite : part 1. Results from X-ray diffraction. *Am. Miner.* **2002**, *87*, 1631–1645.
- (110) Bricker, O. Some stability relations in the system $\text{Mn-O}_2\text{-H}_2\text{O}$ at 25° and one atmosphere total pressure. *Am. Miner.* **1965**, *50*, 1296–1354.
- (111) Junta, J.; Hochella, M. Manganese(II) oxidation at mineral surfaces: A microscopic and spectroscopic study. *Geochim. Cosmochim. Acta* **1994**, *58*, 4985–4999.
- (112) Kessick, M. A.; Morgan, J. J. Mechanism of autoxidation of manganese in aqueous solution. *Environ. Sci. Technol.* **1975**, *9*, 157–159.
- (113) Bigham, J. M.; Schwertmann, U.; Carlson, L.; and Murad, E. A poorly crystallized oxyhydroxysulfate of iron formed by bacterial oxidation of Fe(II) in acid mine waters. *Geochim. Cosmochim. Acta* **1990**, *54*, 2743–2758.
- (114) Stumm, W.; Morgan, J. J. *Chemical Equilibria and Rates in Natural Waters*; 3rd

ed.; 1996.

- (115) Learman, D. R.; Voelker, B. M.; Vazquez-Rodriguez, A. I.; Hansel, C. M. Formation of manganese oxides by bacterially generated superoxide. *Nat. Geosci.* **2011**, *4*, 95–98.
- (116) Friedrich, A. J.; Hasenmueller, E. A.; Catalano, J. G. Composition and structure of nanocrystalline Fe and Mn oxide cave deposits: Implications for trace element mobility in karst systems. *Chem. Geol.* **2011**, *284*, 82–96.
- (117) Hansel CM, Zeiner CA, Santelli CM, W. S. Mn(II) oxidation by an ascomycete fungus is linked to superoxide-production during asexual reproduction. *Proc. Natl. Acad. Sci. U. S. A.* **2012**, *109*, 12621–12625.
- (118) Jurgensen, A.; Widmeyer, J. R.; Gordon, R. A.; Bendell-Young, L. I.; Moore, M. M. The structure of the manganese oxide on the sheath of the bacterium *Leptothrix discophora*: An XAFS study. *Am. Mineral.* **2004**, *89*, 1110–1118.
- (119) Friedrich, A. J.; Luo, Y.; Catalano, J. G. Trace element cycling through iron oxide minerals during redox-driven dynamic recrystallization. *Geology* **2011**, *39*, 1083–1086.
- (120) Lefkowitz, J. P.; Rouff, A. A.; Elzinga, E. J. Influence of pH on the reductive transformation of birnessite by aqueous Mn(II). *Environ. Sci. Technol.* **2013**, *47*, 10364–10371.
- (121) Mandernack, K. W.; Fogel, M. L.; Tebo, B. M.; Usui, A.; Biology, M.; Jolla, L. Oxygen isotope analyses of chemically and microbially produced manganese oxides and manganates. *Geochim. Cosmochim. Acta* **1995**, *59*, 4409–4425.
- (122) Atkins, A. L.; Shaw, S.; Peacock, C. L. Nucleation and growth of todorokite from birnessite: Implications for trace metal cycling in marine sediments. *Geochim. Cosmochim. Acta* **2014**.
- (123) Villalobos, M.; Bargar, J.; Sposito, G. Mechanisms of Pb(II) sorption on a biogenic manganese oxide. *Environ. Sci. Technol.* **2005**, *39*, 569–576.
- (124) Manceau, A.; Lanson, M.; Geoffroy, N. Natural speciation of Ni, Zn, Ba, and As in ferromanganese coatings on quartz using X-ray fluorescence, absorption, and diffraction. *Geochim. Cosmochim. Acta* **2007**, *71*, 95–128.
- (125) Isaure, M. P.; Laboudigue, A.; Manceau, A.; Sarret, G.; Tiffreau, C.; Trocellier, P.; Lamble, G.; Hazemann, J. L.; Chateigner, D. Quantitative Zn speciation in a contaminated dredged sediment by μ -PIXE, μ -SXRF, EXAFS spectroscopy and principal component analysis. *Geochim. Cosmochim. Acta* **2002**, *66*, 1549–1567.
- (126) Grangeon, S.; Manceau, A.; Guilhermet, J.; Gaillot, A.-C.; Lanson, M.; Lanson, B.

Zn sorption modifies dynamically the layer and interlayer structure of vernadite. *Geochim. Cosmochim. Acta* **2012**, 85, 302–313.

- (127) Kwon, K. D.; Refson, K.; Sposito, G. Zinc surface complexes on birnessite: A density functional theory study. *Geochim. Cosmochim. Acta* **2009**, 73, 1273–1284.
- (128) Du, X.; Boonchayaanant, B.; Wu, W.-M.; Fendorf, S.; Bargar, J.; Criddle, C. S. Reduction of Uranium(VI) by Soluble Iron(II) Conforms with Thermodynamic Predictions. *Environ. Sci. Technol.* **2011**, 45, 4718–4725.
- (129) Manceau, A.; Lanson, B.; Schlegel, M. L.; Hargé, J. C.; Musso, M.; Eybert-Bérard, L.; Hazemann, J. L.; Chateigner, D.; Lambelle, G. M. Quantitative Zn speciation in Smelter-contaminated soils by EXAFS spectroscopy. *Am. J. Sci.* **2000**, 300, 289–343.
- (130) Hem, J. D.; Roberson, C. E.; Lind, C. J. Synthesis and stability of hetaerolite, ZnMn_2O_4 , at 25 °C. *Geochim. Cosmochim. Acta* **1987**, 51, 1539–1547.
- (131) Nogues, M., and Poix., P. Effet Jahn-Teller cooperatif dans le system ZnMn_2O_4 - Zn_2SnO_4 . *Ann. Chim.* **1972**, 7, 301–314.
- (132) Klewicki, J. K.; Morgan, J. J. Kinetic behavior of Mn(III) complexes of pyrophosphate, EDTA, and citrate. *Environ. Sci. Technol.* **1998**, 2916–2922.
- (133) Wang, Y.; Stone, A. T. Phosphonate- and carboxylate-based chelating agents that solubilize (hydr)oxide-bound Mn(III). *Environ. Sci. Technol.* **2008**, 42, 4397–4403.
- (134) Trouwborst, R. E.; Clement, B. G.; Tebo, B. M.; Glazer, B. T.; Luther, G. W. Soluble Mn(III) in suboxic zones. *Science* **2006**, 313, 1955–1957.
- (135) Madison, A. S.; Tebo, B. M.; Luther, G. W. Simultaneous determination of soluble manganese(III), manganese(II) and total manganese in natural (pore)waters. *Talanta* **2011**, 84, 374–381.
- (136) Yu, Q.; Sasaki, K.; Tanaka, K.; Ohnuki, T.; Hirajima, T. Structural factors of biogenic birnessite produced by fungus *Paraconiothyrium* sp. WL-2 strain affecting sorption of Co^{2+} . *Chem. Geol.* **2012**, 310-311, 106–113.
- (137) Droz, B.; Dumas, N.; Duckworth, O. W.; Pena, J. A comparison of the sorption reactivity of bacteriogenic and mycogenic {Mn} oxides nanoparticles. *Environ. Sci. Technol.* **2015**.
- (138) Cheney, M. A.; Bhowmik, P. K.; Moriuchi, S.; Villalobos, M.; Qian, S.; Joo, S. W. The Effect of Stirring on the Morphology of Birnessite Nanoparticles. *J. Nanomater.* **2008**, 2008, 1–9.

- (139) Miyata, N.; Tani, Y.; Sakata, M.; Iwahori, K. Microbial manganese oxide formation and interaction with toxic metal ions. *J. Biosci. Bioeng.* **2007**, *104*, 1–8.
- (140) Zhu, M.; Ginder-Vogel, M.; Sparks, D. L. Ni(II) sorption on biogenic Mn-oxides with varying Mn octahedral layer structure. *Environ. Sci. Technol.* **2010**, *44*, 4472–4478.
- (141) Matocha, C. J.; Sparks, D. L.; Amonette, J. E.; Kukkadapu, R. K. Kinetics and mechanism of birnessite reduction by catechol. *Soil Sci. Soc. Am. J.* **2001**, *65*, 58–66.
- (142) Lefkowitz, J. P.; Elzinga, E. J. Impacts of aqueous Mn(II) on the sorption of Zn(II) by hexagonal birnessite. *Environ. Sci. Technol.* **2015**, *49*, 4886–4893.
- (143) McKenzie, R. M. The synthesis of birnessite, cryptomelane, and some other oxides and hydroxides of manganese. *Miner. Mag.* **1971**, *38*, 493–502.
- (144) Murray, J. W.; Balistrieri, L. S.; Paul, B. The oxidation state of manganese in marine sediments and ferromanganese nodules. *Geochim. Cosmochim. Acta* **1984**, *48*, 1237–1247.
- (145) Gibot, P.; Laffont, L. Hydrophilic and hydrophobic nano-sized Mn₃O₄ particles. *J. Solid State Chem.* **2007**, *180*, 695–701.
- (146) Kovanda, F.; Grygar, T.; Dorný, V. Thermal behaviour of Ni – Mn layered double hydroxide and characterization of formed oxides. **2003**, *5*, 1019–1026.
- (147) Elzinga, E. J. Formation of layered Fe(II)-Al(III)-hydroxides during reaction of Fe(II) with aluminum oxide. *Environ. Sci. Technol.* **2012**, *46*, 4894–4901.
- (148) Ressler, T. WinXAS: a program for X-ray absorption spectroscopy data analysis under MS-Windows. *J. Synchrotron Radiat.* **1998**, *5*, 118–122.
- (149) Ankudinov, A.; Rehr, J. J. Relativistic calculations of spin-dependent x-ray-absorption spectra. *Phys. Rev. B* **1997**, *56*, R1712–R1716.
- (150) Post, J. E.; Appleman, D. E. Chalcophanite, ZnMn₃O₇·3H₂O: New crystal-structure determinations were corrected for absorption using the Gaussian integration. *Am. Miner.* **1988**, *73*, 1401–1404.
- (151) Scheinost, A. C.; Sparks, D. L. Formation of Layered Single- and Double-Metal Hydroxide Precipitates at the Mineral/Water Interface: A Multiple-Scattering XAFS Analysis. *J. Colloid Interface Sci.* **2000**, *178*, 167–178.
- (152) Ramesh, T. N.; Kamath, P. V.; Shivakumara C. Classification of stacking faults and their stepwise elimination during the disorder--> order transformation of nickel hydroxide. *Acta Crysta.* **2006**, *B62*, 530–536.

- (153) Pandya, K. I.; O'Grady, W. E.; Corrigan, D. a; McBreen, J.; Hoffman, R. W. Extended x-ray absorption fine structure investigations of nickel hydroxides. *J. Phys. Chem.* **1990**, *94*, 21–26.
- (154) Kwon, K. D.; Refson, K.; Sposito, G. Understanding the trends in transition metal sorption by vacancy sites in birnessite. *Geochim. Cosmochim. Acta* **2013**, *101*, 222–232.
- (155) Simanova, A. A.; Kwon, K. D.; Bone, S. E.; Bargar, J. R.; Refson, K.; Sposito, G.; Peña, J. Probing the sorption reactivity of the edge surfaces in birnessite nanoparticles using nickel(II). *Geochim. Cosmochim. Acta* **2015**.
- (156) Kohler, T.; Armbruster, T.; Libowitzky, E. Hydrogen Bonding and Jahn – Teller Distortion in Groutite, α -MnOOH, and Manganite, γ -MnOOH, and Their Relations to the Manganese Dioxides Ramsdellite and Pyrolusite. *J. Solid State Chem.* **1997**, *500*, 486–500.
- (157) Hem, J. D., Lind, C. J., and Roberson, C. E. Coprecipitation and redox reactions of manganese oxides with copper and nickel. *Geochim. Cosmochim. Acta* **1989**, *53*, 2811–2822.
- (158) Middag, R.; de Baar, H. J. W.; Laan, P.; Cai, P. H.; van Ooijen, J. C. Dissolved manganese in the Atlantic sector of the Southern Ocean. *Deep Sea Res. Part II Top. Stud. Oceanogr.* **2011**, *58*, 2661–2677.
- (159) Konovalov, S. K.; Luther, G. W.; Yücel, M. Porewater redox species and processes in the Black Sea sediments. *Chem. Geol.* **2007**, *245*, 254–274.
- (160) Hem, J. D. Study and Interpretation of the Chemical Characteristics of Natural Water. *USGS Water Supply Pap.* **1985**, 2254.
- (161) Fuller, C. C.; Harvey, J. W. Reactive Uptake of Trace Metals in the Hyporheic Zone of a Mining-Contaminated Stream, Pinal Creek, Arizona. *Environ. Sci. Technol.* **2000**, *34*, 1150–1155.
- (162) Murray, J. W. The interaction of metal ions at the manganese dioxide-solution interface. *Geochemistry Int.* **1975**, *30*, 505–519.
- (163) Wang, Y.; Feng, X.; Villalobos, M.; Tan, W.; Liu, F. Sorption behavior of heavy metals on birnessite: Relationship with its Mn average oxidation state and implications for types of sorption sites. *Chem. Geol.* **2012**, *292-293*, 25–34.
- (164) Rad, S.; Chemic, P.; Ressler, T. WinXAS: a program for X-ray absorption spectroscopy data analysis under MS-Windows. *J. Synchrotron Radiat.* **1998**, *5*, 118–122.
- (165) Fendorf, S. E., Sparks, D. L, Lambe, G. M, Kelley, M. J. Applications of x-ray

- absorption fine-structure spectroscopy to soils. *Soil Sci. Soc. Am. J.* **1994**, 58, 1583–1595.
- (166) Ostergren, J. D.; Brown, G. E.; Parks, G. A.; Tingle, T. N. Quantitative Speciation of Lead in Selected Mine Tailings from Leadville, CO. *Environ. Sci. Technol.* **1999**, 33, 1627–1636.
- (167) Hansel, C. M.; Benner, S. G.; Neiss, J.; Dohnalkova, A.; Kukkadapu, R. K.; Fendorf, S. Secondary mineralization pathways induced by dissimilatory iron reduction of ferrihydrite under advective flow. *Geochim. Cosmochim. Acta* **2003**, 67, 2977–2992.
- (168) Li, H.; Song, B.; Wang, W. J.; Chen, X. L. Facile synthesis, thermal, magnetic, Raman characterizations of spinel structure ZnMn_2O_4 . *Mater. Chem. Phys.* **2011**, 130, 39–44.
- (169) Liu, Y.; Wang, Y.; Xu, X.; Sun, P.; Chen, T. Facile one-step room-temperature synthesis of Mn-based spinel nanoparticles for electro-catalytic oxygen reduction. *RSC Adv.* **2014**, 4, 4727.
- (170) Ressler, T. (1998). WinXAS: a program for X-ray absorption spectroscopy data analysis under MS-Windows. *J. Synchrotron Radiat.*, 5(Pt 2), 118–22.
- (171) Ravel, B. data analysis : crystallography the X-ray absorption spectroscopist ATOMS : Crystallography for the X-ray. *Synchrotron, J Spectrosc. Absorpt.* **2001**, 2000–2002.
- (172) Elzinga, E. J., and Reeder, R. J. X-ray absorption spectroscopy study of Cu^{2+} and Zn^{2+} adsorption complexes at the calcite surface : Implications for site-specific metal incorporation preferences during calcite crystal growth. **2002**, 66, 3943–3954.
- (173) Elzinga, E. J.; Rouff, A. a.; Reeder, R. J. The long-term fate of Cu^{2+} , Zn^{2+} , and Pb^{2+} adsorption complexes at the calcite surface: An X-ray absorption spectroscopy study. *Geochim. Cosmochim. Acta* **2006**, 70, 2715–2725.
- (174) Lee, Y. J.; Elzinga, E. J.; Reeder, R. J. Sorption mechanisms of zinc on hydroxyapatite: Systematic uptake studies and EXAFS spectroscopy analysis. *Environ. Sci. Technol.* **2005**, 39, 4042–4048.
- (175) Albertson J.; Abrahams, S. C.; Kvik, A. Atomic displacements, anharmonic thermal vibration, expansivity and pyroelectric coefficient thermal dependences in ZnO . *Acta Crystallogogr.* **1989**, B45, 34–40.
- (176) Effenberger H.; Mereiter K.; and Zemann, J. Crystal structure refinements of magnesite, calcite, rhodochrosite, siderite, smithsonite, and dolomite, with discussion of some aspects of the stereochemistry of calcite type carbonates. *Z.*

Krist. **1981**, *156*, 33–243.

- (177) Shannon, R. D. Revised effective ionic radii and systematic studies of interatomic distances in halides and chalcogenides. *Acta Crystallogr.* **1976**, *A32*, 751–767.
- (178) Manceau, A.; Tommaseo, C.; Rihs, S.; Geoffroy, N.; Chateigner, D.; Schlegel, M.; Tisserand, D.; Marcus, M. A.; Tamura, N.; Chen, Z.-S. Natural speciation of Mn, Ni, and Zn at the micrometer scale in a clayey paddy soil using X-ray fluorescence, absorption, and diffraction. *Geochim. Cosmochim. Acta* **2007**, *71*, 526–527.
- (179) Webb, S., M. SIXpack: a graphical user interface for XAS analysis using IFEFFIT. *Phys. Scr.* **2005**, *T115*, 1011–1014.

Appendices

Appendix 1: Supporting Information for Chapter 2

A1.1 Synthesis and characterization of Mn-oxide substrates

Hexagonal birnessite was synthesized by dropwise addition of concentrated hydrochloric acid to a boiling solution of potassium permanganate, as per the method described by McKenzie.¹⁴³ The material was washed by dialysis against doubly deionized (DDI) water (18.2 MΩ cm, Milli-Q, Millipore), and then freeze-dried. The N₂-BET surface area of the substrate was 42 m² g⁻¹, and the Mn content of the material was 48.9 wt% as determined by dissolving a known amount of solid in 12M HCl and analyzing the resulting solute for dissolved Mn. The iodine titration method¹⁶² indicated that the average oxidation state of structural Mn was 4.0, suggesting that structural Mn is predominantly in the +4 oxidation state, which is consistent with previous results for birnessite prepared according to the McKenzie.^{43,163} This protocol produces hexagonal birnessite with a typical molar ratio of K/Mn of ~20%^{43,163} yielding an approximate chemical formula of KMn₅O_{10.5}. Reference feitknechtite (β-MnOOH) material was synthesized by reacting 0.05 g L⁻¹ birnessite with 400 μM Mn(II) at pH 7.5 for 8 days under anoxic conditions. Manganite (γ- MnOOH) was produced by reacting 36 mM Mn(II) with 1 g L⁻¹ birnessite for 3 months under anoxic conditions at pH 7.5, whereas hausmannite (Mn₃O₄) was synthesized using the procedure described by Gibot et al.¹⁴⁵ All Mn-oxide solids were analyzed by X-ray diffraction (XRD) to confirm phase identity and purity.

A1.2 Spectroscopic analyses of Mn-oxide sorption products

X-ray diffraction (XRD) patterns were recorded on a Phillips X-PERT diffractometer with Cu Kα radiation over the range 10-70 2θ using a step size of 0.03 2θ and a counting

time of 4 s per point. Attenuated Total Reflectance Fourier Transform Infrared (ATR-FTIR) data were collected using a Perkin Elmer Spectrum 100 IR spectrometer equipped with a TGS detector and a Balston-Parker dry air purger to eliminate CO₂ and moisture from the optics and sample compartments. Spectra were recorded over the range 600-4000 cm⁻¹ as the average of 100 co-added scans at a spectral resolution of 4 cm⁻¹ with a Perkin Elmer Miracle ATR accessory containing a single reflection ZnSe ATR crystal. X-ray absorption spectroscopy (XAS) spectra were recorded on beamline X11A of the National Synchrotron Light Source at Brookhaven National Laboratory in Upton, NY. The storage ring operated at 2.84 GeV with a maximum current of ~300 mA. XAS samples were prepared by dispersing the Mn-oxide solids into boron nitride through mixing with a mortar and pestle. The samples were loaded into lucite sample holders and sealed with Kapton tape. Spectra were collected in fluorescence mode at the Mn K edge (6539 eV) using a Si(111) monochromator detuned by 35% for harmonic rejection, and a Stern-Heald type Lytle fluorescence detector. Scanning was done at room temperature, with 3-5 scans collected for each sample to improve signal:noise. Scans collected for each sample were calibrated and averaged, and then converted to a χ function in WinXAS 3.1¹⁶⁴ using standard procedures.¹⁶⁵ Sample solids typically consisted of mixtures of various Mn-oxide mineral components (see results section). The mineralogical composition of each sample was estimated based on linear combination fits of the k^3 -weighted χ function, using the spectra of birnessite, feitknechtite, manganite and hausmannite as endmembers. Fitting was done with the least squares fitting module of SixPACK over the k range of 2.8-12.0 Å⁻¹, with no energy shifts allowed during optimization.

A1.3 Protocols to ensure anoxic conditions during the experiments Anoxic

Anoxic experiments were performed using protocols described in Elzinga.^{86,147} The experiments were carried out in a glovebox which contained a 95% N₂-5% H₂ atmosphere, and was equipped with a Palladium catalyst (Coy Laboratories) for removal of trace atmospheric oxygen. An O₂-H₂ meter (Coy Laboratories) continuously monitored the atmospheric O₂ and H₂ levels, with no measurable O₂ observed for the duration of each experiment. Anoxic samples and reagents were prepared with anoxic DDI water, prepared by boiling under an N₂ atmosphere and cooling inside the glovebox. Following cooling, the water was left exposed to the glovebox atmosphere for 24 h to eliminate any remaining dissolved O₂. All labware used for the experiments (containers, centrifuge tubes, pipette tips, filters, etc.) was placed in the glovebox for at least 24 h before use.

A1.4 ATR-FTIR results of anoxic Mn(II)-birnessite isotherm samples

Figure A1.S1 presents the results of ATR-FTIR analyses of Mn(II)-birnessite solids retrieved from the isotherm experiments at pH 7.0, 7.5, 8.0 and 8.5. The spectral range shown contains the bending modes of structural OH in feitknechtite and manganite;¹⁵⁶ birnessite and hausmannite have no IR bands in this spectral region. Feitknechtite forms in samples reacted at low Mn(II) concentrations, whereas manganite appears in samples reacted at intermediate and high Mn(II) concentrations. At pH 8.0 and 8.5, manganite and feitknechtite bands disappear at the highest Mn(II) concentrations due to formation of hausmannite (see Figures 2.2 and 2.3 of the main manuscript, and Figure A1.S3 below).

A1.5. Scanning electron microscopy (SEM) images of reacted Mn-oxide solids.

The morphology of Mn-oxide solids retrieved from the Mn(II)-birnessite isotherm experiments was examined by scanning electron microscopy (SEM) using a Hitachi

S4800 microscope. Imaging was performed at a 0.7-5 kV accelerating voltage. Figure A1.S2 demonstrates that reductive transformation of the original birnessite substrate (image a) into feitknechtite (b), a mixture of feitknechtite and manganite (c) and hausmannite (d) during reaction with Mn(II), as documented by the XRD and XAS analyses presented in Figures A1.2 and A1.3 of the main manuscript, is accompanied by distinct changes in the morphology of the Mn-oxide solids. These morphological changes suggest extensive dissolution and re-precipitation of Mn in systems forming MnOOH and Mn₃O₄.

A1.6. Results from linear combination fits of k^3 -weighted χ data of Mn-oxide solids

The k^3 -weighted χ data of Mn(II) sorption samples are presented in Figure A1.S3 along the linear combination fits of the spectra and the spectra of the Mn-oxide reference compounds. The linear combination fit results are presented in Fig. 3 (main manuscript) and summarized in Table S1. We note that the sum of the fractional contributions is generally smaller than 1.0, in particular for samples reacted at the lower Mn(II) levels. This indicates that the set of reference samples used for the linear combination fits is either incomplete or that individual reference spectra are not entirely representative of the corresponding phase in the experimental samples. We believe that both factors may be in play in the results presented here. First, reaction of birnessite with Mn(II) changes the birnessite structure even when no mineralogical transformation occurs, as indicated by the XRD data in Fig. 2 of the main manuscript indicating disruption of the stacking order for samples reacted at pH 5.5 and 6.0 and the low-Mn(II) pH 7.0 sample. The birnessite spectrum used in the LC fit is that of the original birnessite substrate, and thus is likely to

be not fully representative of the birnessite phase remaining in the low-Mn(II) sorption samples. A further consideration is that sorbed Mn(II) may be a significant Mn species in the experimental samples while it is not represented in the reference spectral dataset. At pH 6.0, and in the low Mn(II) concentration range of the pH 7.0 isotherm, sorbed Mn may represent up to ~20% of total Mn in the sorption samples, based on the sorption plateaus of ~100 μM Mn(II) Mn species, which are not accounted for in the LC fits, may thus well be involved in the observation of fractional contributions summing to values smaller than 1.0. Overall, we consider the LC fit results to represent a semi-quantitative picture of the changes occurring to the solid birnessite substrate upon reaction with aqueous Mn(II). Error estimates of LC fit results are obtained from analyses of mixed standard samples consisting of endmember compounds mixed in known proportions^{166,167} and have been reported as 5-10% for Zn and Fe;^{125,167} however, systematic errors result if a relevant reference is missing in the database used for LC fitting.¹²⁵ The development of additional or more representative Mn reference compounds may be an important consideration in future research involving quantitative analysis of Mn-oxide reaction products.

A1.7. Mn(II)-birnessite kinetic sorption experiments

A kinetic Mn(II)-birnessite sorption experiment was performed at pH 8.5 under anoxic conditions, and involved spiking a 0.05 g L⁻¹ birnessite suspension with aqueous Mn(II) at a level of 1000 μM , and subsequent monitoring of the removal of Mn(II) from solution and concurrent changes in the mineralogy of the Mn-oxide solids during the 10 days immediately following Mn(II) addition. The initial birnessite suspension volume was 500 mL. Sampling involved extraction of 20 mL aliquots at regular time points, followed by

filtration through 0.22 μm filters. Filtered solutes were analyzed for aqueous Mn(II) and sample solids were washed and dried using the procedures described in the main manuscript for the isotherm experiments, and analyzed by ATR-FTIR. Figure A1.S4 presents the removal of aqueous Mn(II) from solution over the 10 day reaction period. The results indicate that sorption is fast, with over 95% of Mn(II) removal occurring within the first day of sorption, and minor additional sorption between 1 and 2 days of reaction; no further Mn(II) removal is observed at sorption times beyond 2 days. ATR-FTIR results of the sample solids are presented in Figure A1.S5, with Figure A1.S5a presenting the spectral region containing the bending modes of structural OH in manganite and feitknechtite, and Figure A1.S5b presenting the frequency region containing the lattice modes (Mn-O vibrations)¹⁶ of Mn-oxide solids. The IR results show no evidence for the formation of feitknechtite at any time point during the 10 day experimental time frame (Figure A1.S5a), whereas lattice vibrations characteristic of hausmannite appear within 30 minutes of reaction (Figure A1.S5b). These results indicate that hausmannite either forms directly without crystallization of intermediate feitknechtite, or that any transient feitknechtite is quickly converted into hausmannite and does not build up to a detectable extent under the conditions of this experiment. Also shown in Figures A1.S5a and A1.S5b is the spectrum obtained for a sample taken following 180 days of reaction in this kinetic experiment. The IR results indicate the persistence of hausmannite and show no indication for the presence of other phases (i.e. manganite or feitknechtite) suggesting that hausmannite is stable with respect to conversion to other Mn-oxide phases under the experimental conditions applied.

A1.8 Supporting Information Figures

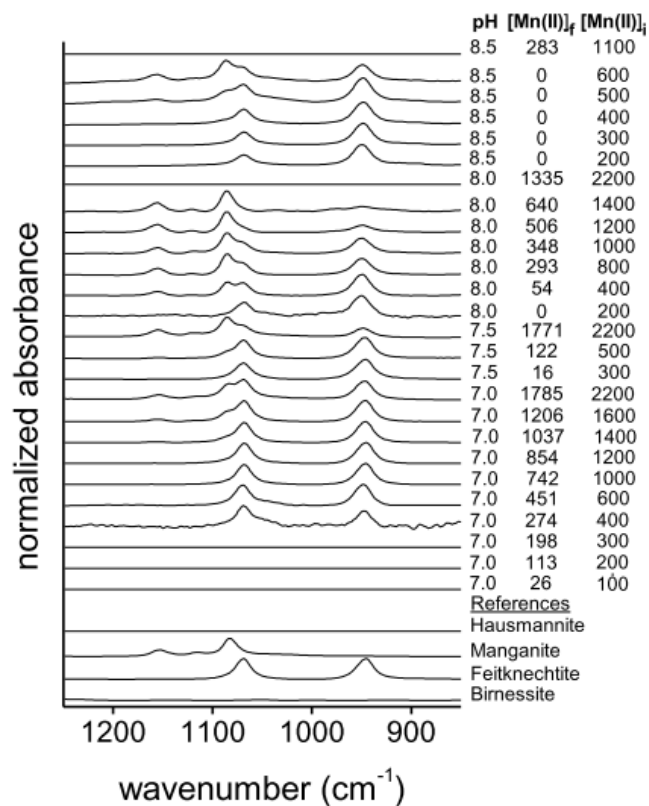


Figure A1.S1. ATR-FTIR spectra of anoxic Mn(II)-birnessite samples at pH 7.0-8.5.

Normalized ATR-FTIR spectra of Mn(II)-birnessite sorption samples prepared under anoxic conditions at pH 7.0-8.5 using a birnessite suspension density of 0.05 g L^{-1} and an 8 day reaction time. Initial and final Mn(II) solution concentrations ($[\text{Mn(II)}]_i$ and $[\text{Mn(II)}]_f$) and sample pH are indicated adjacent to the spectra. Reference spectra are presented at the bottom.

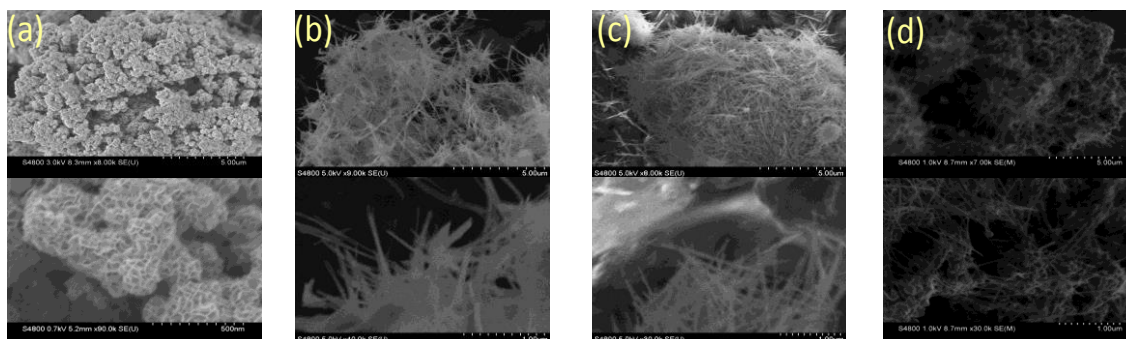


Figure A1.S2. SEM images of selected sorption samples and Mn oxides.

SEM images of (a) the original K-birnessite substrate; (b) feitknechtite, formed as a result of reductive transformation of birnessite (0.05 g L^{-1}) by Mn(II) during reaction (8 days) under anoxic conditions at pH 7.5 and a total Mn(II) concentration of $500 \text{ }\mu\text{M}$; (c) a mixture of feitknechtite and manganite, formed during reaction (8 days) of birnessite (0.05 g L^{-1}) with aqueous Mn(II) under anoxic conditions at pH 7.5 and a total Mn(II) concentration of $2200 \text{ }\mu\text{M}$; and (d) hausmannite following reaction (8 days) of birnessite (0.05 g L^{-1}) with Mn(II) under anoxic conditions at pH 8.5 and a total Mn(II) concentration of $2200 \text{ }\mu\text{M}$. Top and bottom frames represent high and low magnification, respectively.

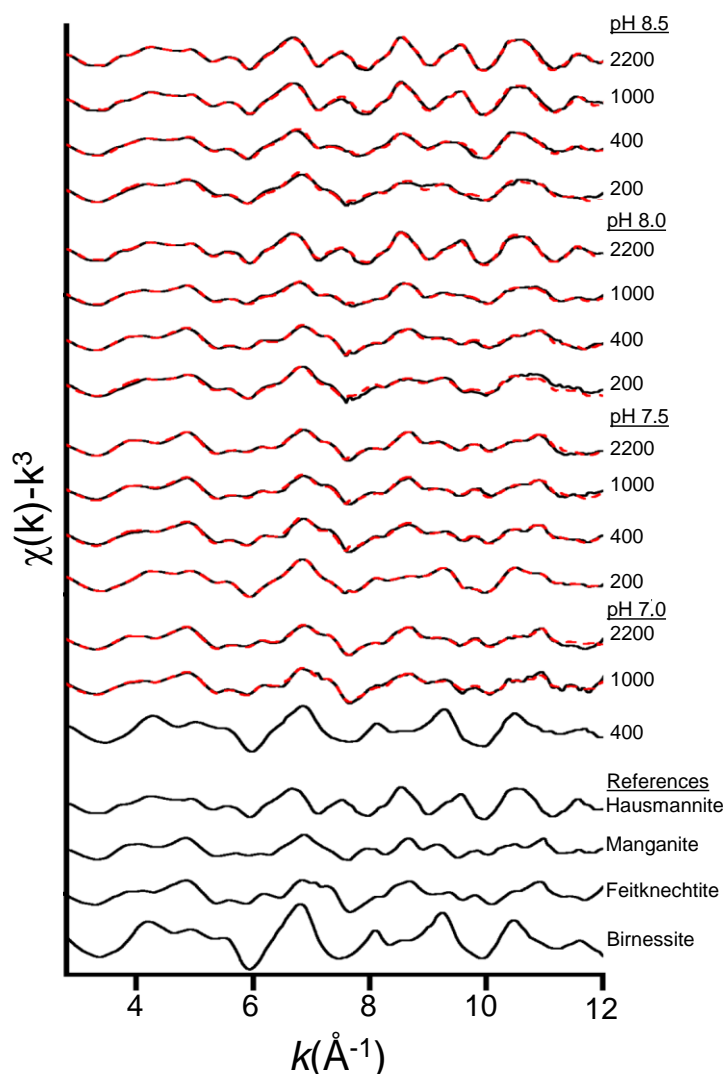


Figure A1.S3. EXAFS data of sorption samples at pH 7-8.

Mn K edge k^3 -weighted χ functions of Mn-oxide reference minerals and Mn(II)-birnessite sorption samples reacted at $\text{pH} \geq 7.0$. Sorption samples were prepared under anoxic conditions at a birnessite suspension density of 0.05 g L^{-1} and a reaction time of 8 days; initial $[\text{Mn(II)}]$ (in μM) is indicated adjacent to each experimental spectrum. The raw spectra are shown in black, and the red lines represent the linear combination (LC) fits of the experimental data using the reference spectra at the bottom of the graph as endmembers. See Table A1.S1 and Figure A1.3 of the main manuscript for LC fit results.

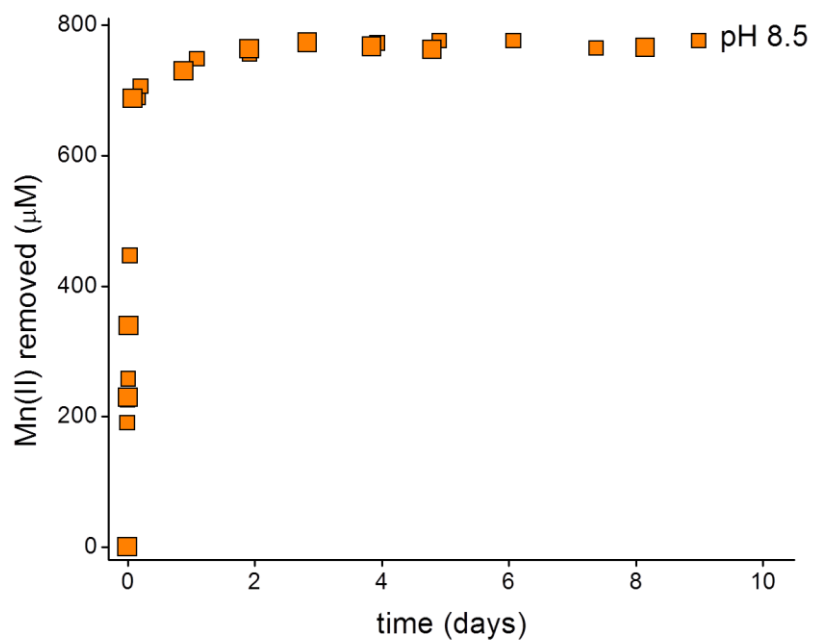


Figure A1.S4. Time-dependent removal of Mn(II) at pH 8.5

Time-dependent removal of aqueous Mn(II) during reaction with 0.05 g L^{-1} birnessite at pH 8.5, and an initial Mn(II) concentration of 1000 μM under anoxic conditions.

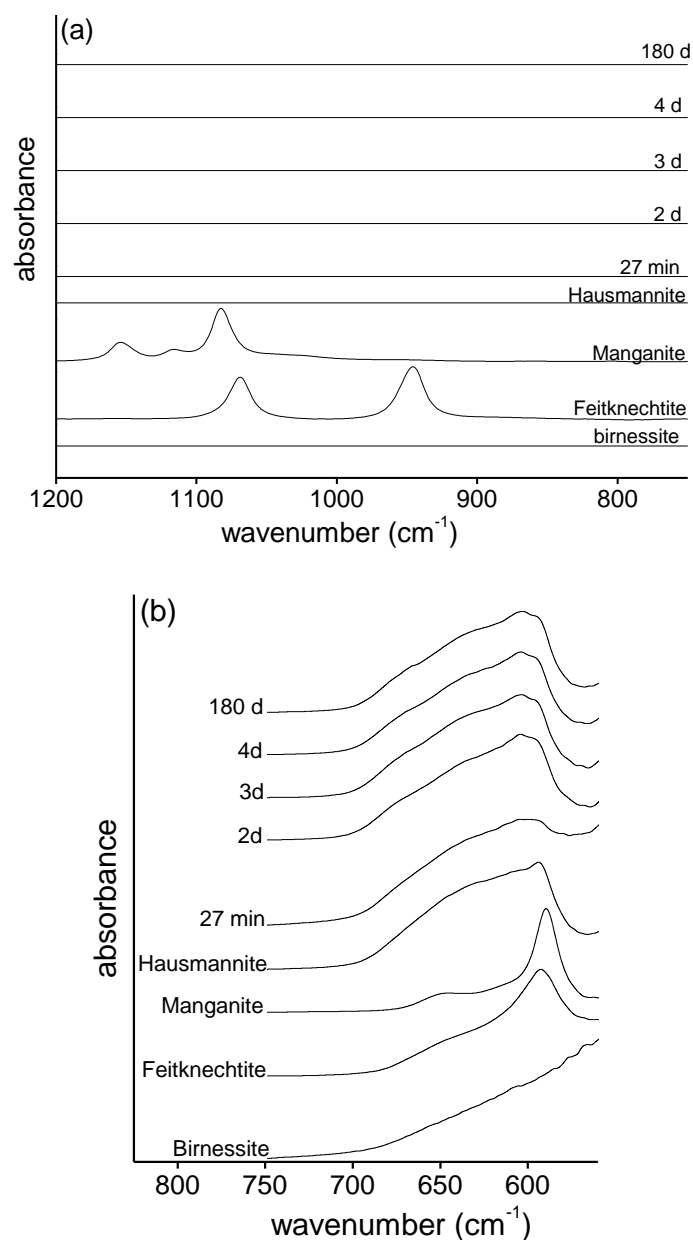


Figure A1.S5. ATR-FTIR data of pH 8.5 sorption samples

ATR-FTIR spectra of sample solids obtained from the kinetic experiment presented in Figure A1.S4, involving reaction of aqueous Mn(II) (1000 μM) with birnessite (0.05 g L⁻¹) under anoxic conditions at pH 8.5: (a) the spectral region containing the bending modes of structural OH in feitknechtite and manganite; and (b) the low frequency spectral region containing the lattice modes (Mn-O vibrations) of Mn-oxides.

A1.9 Tables for Chapter 2

Table A1.S1: Summary of the quantitative LC fit results of the k^3 -weighted χ data.

pH	Mn(II) input (μM)	Fractional Contribution			
		Birnessite	Feitknechtite	Manganite	Hausmannite
7	0	1.00	-	-	-
	400	0.80	-	-	-
	1000	0.09	0.85	-	-
	2200	-	0.56	0.37	-
		Birnessite	Feitknechtite	Manganite	Hausmannite
7.5	0	1.00	-	-	-
	200	0.43	0.41	-	-
	400	0.11	0.80	-	-
	1000	-	0.50	0.39	-
	2200	-	0.43	0.59	-
		Birnessite	Feitknechtite	Manganite	Hausmannite
8	0	1.00	-	-	-
	200	0.28	0.60	-	-
	400	-	0.69	0.20	-
	1000	-	0.32	0.30	0.33
	2200	-	-	-	1.01
		Birnessite	Feitknechtite	Manganite	Hausmannite
8.5	0	1.00	-	-	-
	200	0.28	0.60	-	-
	400	-	0.19	0.23	0.61
	1000	-	-	-	1.01
	2200	-	-	-	1.08

Appendix 2: Supporting Information for Chapter 3

A2.1. Synthesis of Mn-oxide substrates

Hexagonal birnessite was synthesized according to the protocol of McKenzie¹⁴³ wherein concentrated hydrochloric acid is added dropwise to a boiling solution of potassium permanganate. Following dialysis against doubly deionized water (18.2 MΩ cm, Milli-Q, Millipore), the product was freeze-dried. The substrate had an N₂-BET specific surface area of 42 m² g⁻¹, and an Mn content of 48.9 wt% as determined by dissolution of a known amount of the mineral in 12M HCl followed by analysis of the solute for dissolved Mn(II). The average oxidation state of structural Mn in the material was determined to be 4.0 using the iodine titration method of Murray et al.¹⁴⁴

Reference feitknechtite (β-MnOOH) material was synthesized by reacting 400 μM Mn(II) at pH 7.5 for 8 days under anoxic conditions with an equimolar concentration of Mn(IV) present in birnessite (0.05 g L⁻¹). Manganite (γ-MnOOH) was synthesized by reacting 36 mM Mn(II) with 1 g L⁻¹ birnessite under anoxic conditions for 3 months at pH 7. Hausmannite (Mn(II)Mn(III)₂O₄) was synthesized according to the procedure of Gibot et al.¹⁴⁵ wherein an aqueous solution containing 20 mM KMnO₄ was combined with a 200 mM solution of monohydrate hydrazine and reacted for one hour at 70 °C. Zn(II)-substituted hausmannite was synthesized by slight modification of the procedure of Gibot et al.¹⁴⁵ In our synthesis, an aqueous solution containing 20 mM KMnO₄ and 600 μM Zn(II) was combined with a 200 mM solution of monohydrate hydrazine and reacted for one hour at 70 °C to yield a Zn(II)-substituted hausmannite with chemical formula Zn(II)_{0.09}Mn(II)_{0.91}Mn(III)₂O₄. Hetaerolite (Zn(II)Mn(III)₂O₄) was synthesized according to the protocol of Li et al.¹⁶⁸ where Zn(CH₃CO₂)₂ was reacted with MnCl₂ at

600°C. Another hetaerolite reference was synthesized according to the protocol of Liu et al.¹⁶⁹ with $\text{MnCl}_2 \cdot 4\text{H}_2\text{O}$ used in place of $\text{Mn}(\text{Ac})_2 \cdot 4\text{H}_2\text{O}$. In this method, a 0.1 M solution of aqueous Mn^{2+} was added dropwise to 150 mL of 0.25 M NaOH at room temperature. Following 30 minutes of reaction, the resulting precipitate was washed with DDI water and centrifuged for three cycles. Finally, the rinsed precipitate was collected by centrifugation and allowed to dry at 80 °C for 12 hours. X-ray diffraction (XRD) analysis was used to confirm phase identity and purity of the reference materials used in this study.

A2.2. Experimental protocols to ensure anoxic conditions

Anoxic experiments were performed using protocols described in Elzinga⁸⁶ and Lefkowitz et al.¹²⁰ The experiments were carried out in a glovebox which contained a 95% N_2 -5% H_2 atmosphere, and was equipped with a Palladium catalyst (Coy Laboratories) for removal of trace atmospheric oxygen. An O_2 - H_2 meter (Coy Laboratories) continuously monitored the atmospheric O_2 and H_2 levels, with no measurable O_2 observed for the duration of each experiment. Anoxic samples and reagents were prepared with anoxic DDI water, prepared by boiling under an N_2 atmosphere and cooling inside the glovebox. Following cooling, the water was left exposed to the glovebox atmosphere for 24 h to eliminate any remaining dissolved O_2 . All labware used for the experiments (containers, centrifuge tubes, pipette tips, filters, etc.) was placed in the glovebox for at least 24 h before use.

A2.3. XAS data analyses

EXAFS data processing and fitting were performed using the program WinXAS.¹⁷⁰ A linear function for the pre-edge region and a second-order polynomial in the post-edge

region were used for normalization. The $\chi(k)$ functions were extracted using a cubic spline and were Fourier transformed with k^3 weighting over the approximate k range 2.1-11.5 \AA^{-1} .

Data fitting of the sorption samples involved both shell-by-shell fits and linear combination (LC) fits. Shell-by-shell fits were performed on the data obtained for the binary Zn(II)-birnessite sorption samples, where Zn(II) is present exclusively as adsorption complexes coordinated to the birnessite surface. LC fits were applied to the ternary samples reacted at pH 7.5 and 8.5, where Zn(II) was present as a mixture of surface complexes and precipitate phases. The ternary sorption sample reacted at pH 6.5 was dominated by Zn(II) surface complexes and therefore analyzed with shell-by-shell fits. The fitting procedures and results are described in the next sections.

A2.4. Shell-by-shell fits of Zn K-edge EXAFS data

Shell-by-shell fits were performed in R-space for the binary Zn(II)-birnessite sorption samples (reacted at pH 6.5, 7.5, and 8.5), one ternary sample (pH 6.5) and the Zn(II)Mn(III)₂O₄ and Zn(II)_{0.09}Mn(II)_{0.91}Mn(III)₂O₄ reference compounds. The programs ATOMS¹⁷¹ and FEFF7¹⁴⁹ were used to calculate theoretical Zn scattering paths based on the crystal structures of chalcophanite¹⁵⁰ and hetaerolite.¹³¹ As in our previous studies,¹⁷²⁻¹⁷⁴ an amplitude reduction factor (S_0^2) of 1.0 was used for fitting. This value was determined from fits of the reference compounds ZnO and ZnCO₃ (Table A2.S1), which have uniform and distinct shells of Zn(II) in tetrahedral and octahedral coordination with first shell O, respectively.^{175,176}

Fourier transformation of the experimental χ data of the binary sorption samples (Figure 3.4 of the main manuscript) revealed the presence of three main shells

surrounding central Zn, as found in previous studies of Zn(II) surface complexes on hexagonal birnessite.^{59,89,98} The first shell, centered near 1.5 Å (uncorrected for phase shift) is Zn-O, whereas the shells near 3.0 and 5.0 Å (uncorrected for phase shift) are Zn-Mn shells.^{59,89,98} The presence of these two Zn-Mn shells is qualitatively consistent with Zn coordination at Mn vacancy sites in the birnessite sheets.⁸⁹ Two different shell-by-shell fitting strategies were applied to derive quantitative information on the coordination environment of the Zn(II) surface complexes. These are presented next.

A2.5. Single-shell fits

We started data analysis by fitting the shells visible in the RSF with a single Zn-O and two single Zn-Mn correlations, with no constraints placed on the fitting parameters (i.e. coordination number, radial distance and Debye-Waller factor). This yielded consistent and physically realistic results for the Zn-O and the first Zn-Mn shell. However, the coordination numbers of the second Zn-Mn shell were unrealistically high (>15) for several samples, although the radial distances consistently were in the range 5.35-5.45 Å. Because of the large errors associated with the fitting results of the second Zn-Mn shell, and its relatively small contribution to the XAS spectra (compared to the other two correlations), it was omitted from the fitting procedure.

The fit results obtained with this strategy are presented in Table S1. For Zn K-edge EXAFS data, the radial distance of first shell Zn-O can be used to deduce the O coordination around central Zn, with distances of 2.10 ± 0.03 Å indicating octahedral coordination, and distances of 1.97 ± 0.03 Å indicating tetrahedral coordination¹⁷⁷. This is well demonstrated by the fit results of zincite (ZnO) and smithsonite (ZnCO₃) reference compounds, which have Zn(II) in tetrahedral and octahedral coordination,

respectively,^{175,176} yielding interatomic Zn-O distances of 1.96 and 2.11 Å (Table S1). The Zn(II)-birnessite sorption samples have first-shell Zn-O radial distances of 2.00-2.02 Å (Table S1). These distances are intermediate between those expected for octahedral and tetrahedral coordination, and thus suggest a mixture of octahedral and tetrahedral Zn(II) surface complexes in these samples. This is corroborated by the relatively high Debye-Waller factors of the Zn-O shells ($> 0.01 \text{ Å}^2$ in all samples; Table S1), which indicate a high degree of disorder in Zn-O distances as would be expected for a mixed population of octahedral and tetrahedral Zn(II). These findings agree with the results from previous XAS studies which have similarly shown a mixture of tetrahedrally and octahedrally coordinated Zn(II) at the surface of natural and synthetic hexagonal birnessite and vernadite, with the importance of octahedral complexes increasing with Zn(II) surface loading.^{59,92,126,129,178}

The second shell Zn-Mn distance of 3.40-3.44 Å and the large CN values of this shell (5.4-6.5; Table A2.S1) are consistent with coordination of Zn(II) as triple-corner-sharing inner-sphere complexes over Mn vacancies in the octahedral birnessite sheets.^{59,89,98,126} This configuration involves coordination of Zn(II) to three structural O atoms at the Mn vacancy that are shared with 6 Mn atoms surrounding the vacancy, as occurs in chalcophanite.^{59,89,98,126} The relatively high Debye-Waller factors of the second shell Zn-Mn correlation ($\sim 0.015 \text{ Å}^2$; Table S1) indicates substantial variation in the interatomic Zn-Mn distances. This may be attributed at least in part to the mixed presence of octahedral and tetrahedral Zn(II), which have different $R_{\text{Zn-Mn}}$ ^{59,89}. Formation of bidentate corner-sharing Zn(II) complexes at birnessite edges sites also yields Zn-Mn distances of 3.4-3.5 Å. However, this coordination would result in CN values of ~ 2 , and

cannot account for the presence of the Mn neighbors observed at $R \sim 5.4 \text{ \AA}$ (represented by the Zn-Mn shell visible at 5 \AA (uncorrected for phase-shift) in the RSF of Figure 3.4b of the main manuscript).⁸⁹ We can additionally exclude formation of edge-sharing surface Zn(II) complexes at birnessite sheet edges and Zn(II) incorporation into the octahedral birnessite sheets as major retention mechanisms, because both of these coordination modes would result in Mn neighbors at radial distances $< 3.3 \text{ \AA}$,⁸⁹ which are not observed. Overall, the XAS data demonstrate the importance of the layer vacancy sites in Zn(II) retention at the birnessite surface, and indicate that Zn(II) sorption occurs primarily through the formation of Zn(II) tridentate complexes over these sites.

A2.6. Two-shell fits

To further refine the Zn(II) coordination on the birnessite surface, we employed a second fitting strategy where the Zn XAS data were fitted with two sets of Zn-O and Zn-Mn shells, one corresponding to octahedral Zn ($^{\text{VI}}\text{Zn-O}$ and $^{\text{VI}}\text{Zn-Mn}$) and the other to tetrahedral Zn ($^{\text{IV}}\text{Zn-O}$ and $^{\text{IV}}\text{Zn-Mn}$). Such a two-shell fitting approach has been successfully used by Toner et al.⁵⁹ and Fuller and Bargar⁸⁹ for shell-by-shell fits of Zn(II) sorbed to biogenic birnessite containing both octahedral and tetrahedral Zn(II) surface complexes. We allowed coordination numbers to float during optimization, as done in the study of Toner et al.⁵⁹ Because of the strong overlap of the octahedral and tetrahedral subshells, this fitting strategy required substantial constraints to yield consistent results. The following constraints were imposed:

- (1) The Debye-Waller factors of first-shell $^{\text{VI}}\text{Zn-O}$ and $^{\text{IV}}\text{Zn-O}$ were fixed at the values obtained for smithsonite (0.007 \AA^2) and zincite (0.006 \AA^2), respectively.

(2) The coordination numbers (CN) of second-shell Zn-Mn were correlated to that of first shell Zn-O based on the assumption that the Zn(II) is sorbed as triple corner sharing complexes at birnessite layer vacancy sites. The CN of second-shell Zn-Mn for this configuration is 6.^{59,89,98,126} Accordingly, the CN values of ^{VI}Zn-O and ^{VI}Zn-Mn were constrained to be equal, while the CN of ^{IV}Zn-Mn was set to 1.5 the value of CN of ^{IV}Zn-O.

The accuracy of each of the optimized fitting parameters obtained from this fitting procedure (which attempts to resolve the individual coordination environments of the octahedral and tetrahedral Zn(II) surface species) were difficult to estimate. Fits of the reference compounds suggest an uncertainty of approximately $\pm 15\%$ and ± 0.03 Å for the CN and R values of the first ligand O shell, respectively, and $\pm 30\%$ and $> \pm 0.05$ Å for the CN and R values of shells located beyond the first coordination shell (Table S1). Errors in the Debye-Waller factor, which is linearly correlated to CN, are estimated as ± 0.002 - 0.004 Å². These uncertainties will be higher for the sorption samples due to overlapping subshells.

The fit results of the two-shell fitting approach are presented in Table S1. The radial distances of ^{IV}Zn-O span the range 1.97-1.99 Å, while those of ^{VI}Zn-O are in the range 2.12-2.16 Å. These values bookend the Zn-O distances of the single shell fits described in the previous section (Table S1). This is consistent with interpretation of the single shell fit results as the (weighted) average values of those of the tetrahedral and octahedral Zn species. The two-shell fit results resemble those of Fuller and Bargar,⁸⁹ who reported radial distances for ^{IV}Zn-O in the range 1.99-2.02 Å, and for ^{VI}Zn-O in the

range 2.16-2.21 Å. Similarly, Manceau et al.⁹⁸ reported R ranges for ^{IV}Zn-O and d^{VI}Zn-O of 1.97-2.02 Å and 2.15-2.20 Å, respectively.

For the second shell, we find radial distances for ^{IV}Zn-Mn in the range 3.36-3.39 Å, and for ^{VI}Zn-Mn in the range 3.47-3.51 Å (Table S1). These values again bound the values of the single shell fits (Table S1), and compare favorably to those of Fuller and Bargar,⁸⁹ who report radial distances of 3.36-3.43 Å for ^{IV}Zn-Mn, and 3.52-3.60 Å for ^{VI}Zn-Mn. The results are also similar to those of Manceau et al.,⁹⁸ who reported radial distances of 3.35 Å and 3.50 Å for ^{IV}Zn-Mn and ^{VI}Zn-Mn, respectively, and to those of Toner et al.,⁵⁹ who reported values of 3.39 Å and 3.53 Å. These results provide further evidence for the presence of tetrahedral and octahedral Zn(II) that form tridentate corner-sharing complexes above and below Mn layer vacancies.

A2.7. Linear combination fits

Linear combination (LC) fits were applied to estimate Zn(II) speciation in the ternary sorption samples reacted at pH 7.0-8.5. Fitting was done on the k^3 -weighted χ functions, using the spectra of heteroerolite (Zn(II)Mn(III)₂O₄) and of binary Zn(II)-sorbed birnessite (representing Zn(II) surface complexes) as endmembers. The fits were performed with the least squares fitting module of SixPACK¹⁷⁹ over the k range of 2.4-11.5 Å⁻¹, with no energy shifts allowed during optimization, and with the sum of the components allowed to vary. Uncertainties of the LC fit results are estimated at 5-10%, in line with estimates of previous studies.^{120,125,167}

A2.8. Linear combination fits for the pH 7.5 ternary kinetic experiment

Figure S1 shows the results of the linear combination fits of the XAS data obtained for the kinetic series obtained for the ternary experiment conducted at pH 7.5, where an

anoxic birnessite suspension (0.1 g L^{-1}) was first reacted for two days with $200 \text{ }\mu\text{M}$ Zn(II), and then spiked with $1000 \text{ }\mu\text{M}$ Mn(II). The LC fit results are additionally summarized in Table S2. The overlays of the raw and fitted spectra are presented in Figure 4 of the main manuscript.

The LC fit results demonstrate that Mn(II) addition to the Zn(II)-equilibrated birnessite suspension triggers rapid formation of a spinel Zn(II)-Mn(III) phase resembling hetaerolite ($\text{Zn(II)Mn(III)}_2\text{O}_4$), which accounts for $\sim 25\%$ of total Zn(II) 30 minutes after the addition of Mn(II) (the earliest sampling time point), and for 85% after 6 days (Figure A2.S1, Table A2.S2). We note that the fractional component sums are close to one for all samples (Table A2.S2), which suggests that the two endmembers used are an adequate representation of the Zn(II) species present in these samples.

A2.9 XAS data of samples reacted at various values of pH, [Mn(II)] and [Zn(II)]

Figure S2 shows the Zn K-edge EXAFS data obtained for sorption samples where anoxic birnessite suspensions (0.1 g L^{-1}) were reacted at variable pH and Zn(II) and Mn(II) concentrations. These samples were first reacted with Zn(II) for 2 days, and subsequently with Mn(II) for an additional 6 days. The results demonstrate that precipitation of Zn(II)-Mn(III) spinels resembling hetaerolite occurs in all ternary samples reacted at pH values ≥ 7 , based on the signature features indicated in panel (a). Precipitation of these phases occurs in addition to formation of Zn(II) surface complexes. Nucleation of Zn(II)-Mn(III) spinels even at low inputs of Zn(II) and Mn(II) suggest that these phases may represent a significant sink for Zn(II) in systems where active redox cycling of manganese occurs.

To quantify the Zn speciation in the ternary sorption samples (spectra b, c, f-n and p in Figure A2.S2), LC fits were performed using hetaerolite and Zn(II)-sorbed birnessite

as endmembers. The binary Zn(II)-birnessite spectrum used as an LC endmember for each ternary sample had the same pH and Zn(II) concentration as the ternary system. The two exceptions were the ternary sample reacted at pH 7 (spectrum c in Figure A2.S2), and the sample with a high Zn(II) input (spectrum n in Figure A2.S2) for which the spectrum of the pH 7.5 binary sorption sample reacted with 200 μM Zn(II) was used. The LC fit results of these samples are summarized in Table A2.S3 and Figures A2.S3 and A2.S4; the raw and fitted spectra are overlain in Figure A2.S2.

Figure A2.S3 plots the LC fit estimates of the fractional contributions of hetaerolite and adsorbed Zn(II) in the pH 7.5 samples as a function of the initial Mn(II) concentration, at Zn(II) concentration of 50 μM (panel a) and 200 μM (panel b). The results show that formation of the hetaerolite-like phases increases with increasing Mn(II) at a given concentration of Zn(II). Figure A2.S4 displays the pH dependence of the fractional contributions of hetaerolite and adsorbed Zn(II) in the ternary samples with 200 μM Zn(II) and 1000 μM Mn(II). The results show that the importance of Zn(II)-Mn(III) spinel precipitation increases with pH.

Figure A2.S5 shows the ATR-FTIR spectra of sample solids from the binary isotherm experiment (panel a), and from the binary and ternary kinetic experiments (panels b and c, respectively). All experiments were carried out under anoxic conditions at pH 6.5 and 7.5 and utilized a 0.1 g L^{-1} suspension density of birnessite. In the isotherm experiment, variable inputs of Mn(II) (50-2000 μM) were reacted with birnessite for 8 days. In the binary kinetic experiment, 1000 μM Mn(II) was reacted with the birnessite substrate, whereas in the ternary kinetic experiment, birnessite was first equilibrated with 200 μM Zn(II) for 2 days and subsequently reacted with 1000 μM Mn(II). For the

isotherm experiment (Figure A2.S5a), the concentration of Mn(II) added to the reaction system is indicated next to each spectrum. For the kinetic experiments (Figures A2.S5b and c); time points next to each spectrum refer to the reaction time of birnessite with Mn(II). The spectra displayed at the bottom of each figure are of the reference compounds feitknechtite and manganite, which are the main transformation products formed during reductive transformation of birnessite by aqueous Mn(II) at pH 7 and 7.5. Both compounds contain distinct OH bending modes in the spectral region shown (1200-850 cm^{-1}),¹⁵⁶ whereas neither birnessite nor hetaerolite contain IR bands in this region. Although experiments were run at both pH 6.5 and 7.5, only the pH 7.5 results are shown. This is because the spectra of the pH 6.5 experiments are indistinguishable from those of the starting substrate, which is due to the lack of mineralogical transformation of birnessite during reaction with Mn(II) at this pH. The spectra have no distinctive features in the 1200-850 cm^{-1} spectral range, and are therefore not displayed.

The isotherm data presented in Figure A2.S5 (panel a) are consistent with our previous results.^{86,120} At relatively low inputs of Mn(II), the dominant transformation product is feitknechtite, whereas at higher Mn(II) inputs a mixture of feitknechtite and manganite is observed. Results of the binary kinetic experiment (Figure A2.S5b) are consistent with our previous findings⁸⁶ wherein Mn(II) initially induces transformation of birnessite into feitknechtite (β -MnOOH), which starts forming within the first day of reaction (Figure A2.S5b). Feitknechtite is metastable and converts into the more stable manganite (γ -MnOOH) polymorph, which starts growing in after 6 days (Figure A2.S5b). Elzinga⁸⁶ demonstrated that the conversion of feitknechtite into manganite is catalyzed by aqueous Mn(II).

In the ternary experiment (Figure A2.S5c), formation of feitknechtite is not evident until two days of reaction with Mn(II). The delayed formation of feitknechtite is attributed to the competing pathway of Zn(II) precipitation with Mn(III) surface species to produce the hetaerolite-like phase discussed in the main manuscript. In addition, the ternary experiment shows no evidence for conversion of feitknechtite into manganite (Figure A2.S5c). This is attributed to the depletion of Mn(II) from solution which would otherwise catalyze conversion of metastable feitknechtite⁸⁶. The relatively high concentration of Mn(II) in the binary experiment compared to the ternary experiment (Figure 3.2c of the main manuscript) enhances conversion of metastable feitknechtite into manganite in the binary system, whereas this catalytic effect is less pronounced in the ternary experiment where Mn(II) solution levels are lower.

A2.10. Supporting Information Figures

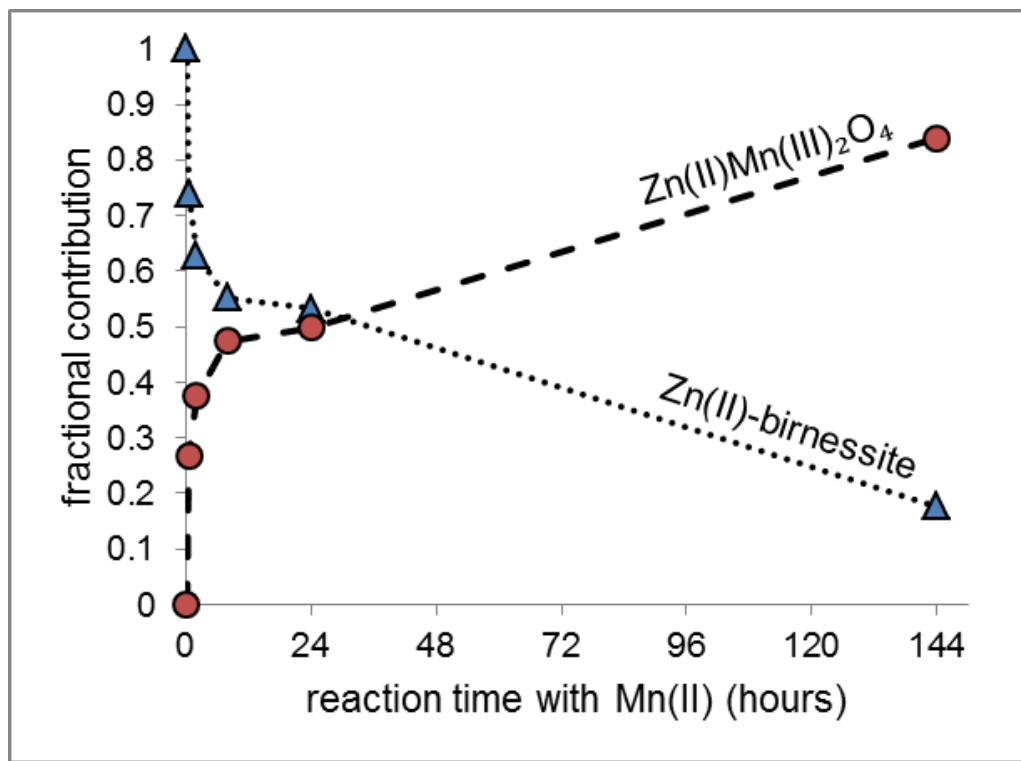


Figure A2.S1. Linear combination fit results.

Linear combination fit results for the kinetic sorption experiment where anoxic 0.1 g L^{-1} birnessite was reacted with $200 \text{ }\mu\text{M}$ of Zn(II) for two days, and then reacted with $1000 \text{ }\mu\text{M}$ Mn(II) for an additional six days at a constant pH of 7.5. The reaction time plotted on the x-axis is with respect to the time point of Mn(II) addition at $t=0$. The fractional contributions of the Zn(II)-birnessite surface complexes and Zn(II)Mn(III)₂O₄ are summarized in Table A2.S2.

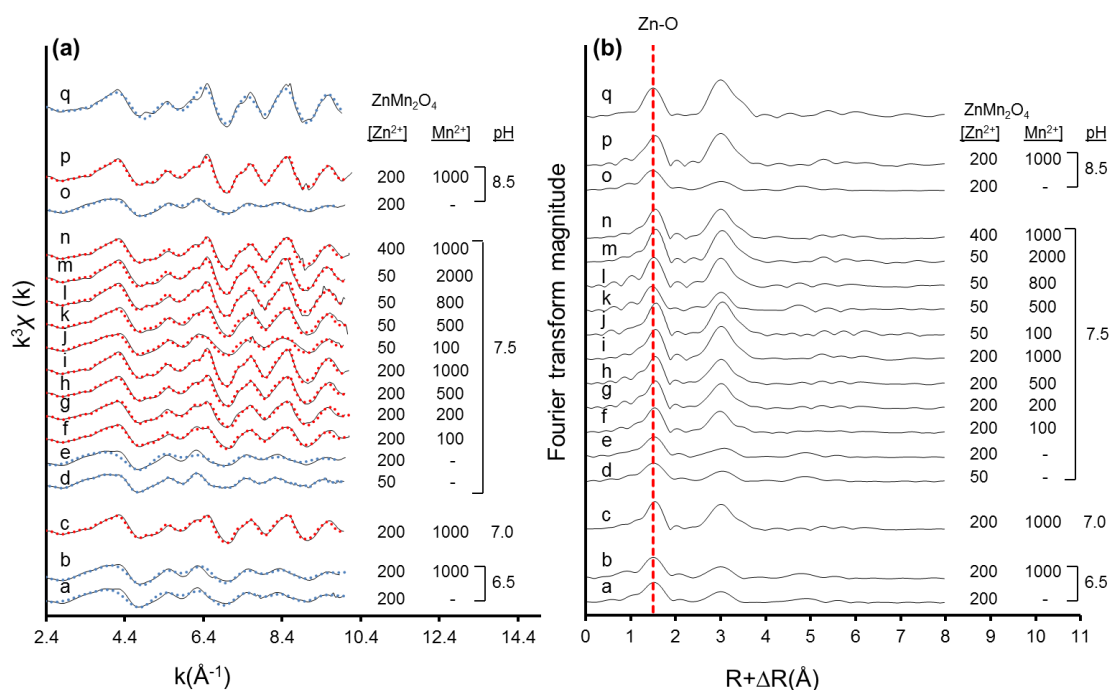


Figure A2.S2. Zn K edge EXAFS data.

Zn K edge EXAFS data of anoxic birnessite (0.1 g L⁻¹) sorption samples reacted at pH 6.5–8.5 under binary and ternary conditions: (a) k^3 -weighted χ functions. Shell fits are represented by blue dotted lines whereas LC fits are represented by red dotted lines. (b) corresponding radial distribution functions. All samples were reacted with Zn(II) for two days. Ternary samples were reacted with Mn(II) for six days following the two day equilibration time with Zn(II). In panel (a), the raw spectra are shown in black, while the LC fits are shown in red; LC fit results are summarized in Table A2.S3 and Figures A2.S3 and A2.S4. The blue spectra in panel a are the theoretical spectra obtained from the two-shell fitting strategy described in section 3.1.2; the corresponding fit parameters are presented under the “Fit 2” results in Table A2.S1.

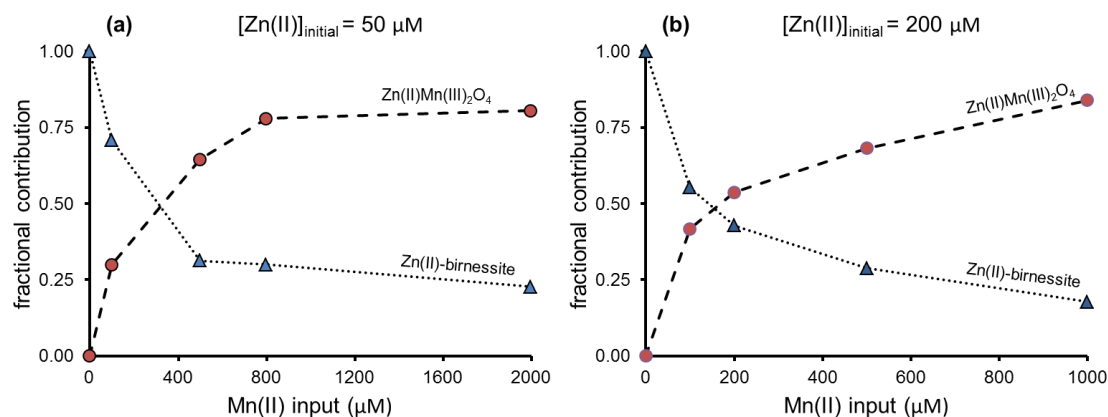


Figure A2.S3. Linear combination fit estimates

LC fit estimates (presented in Table S3) of the fractional contributions of hetaerolite and adsorbed Zn(II) in the pH 7.5 ternary samples plotted as a function of the initial Mn(II) concentration, at Zn(II) concentrations of (a) 50 μM , and (b) 200 μM . Sample preparation involved reaction of an anoxic 0.1 g L⁻¹ birnessite suspension with 50 μM (panel a) or 200 μM (panel b) of Zn(II) for two days, followed by reaction with 1000 μM Mn(II) for six days.

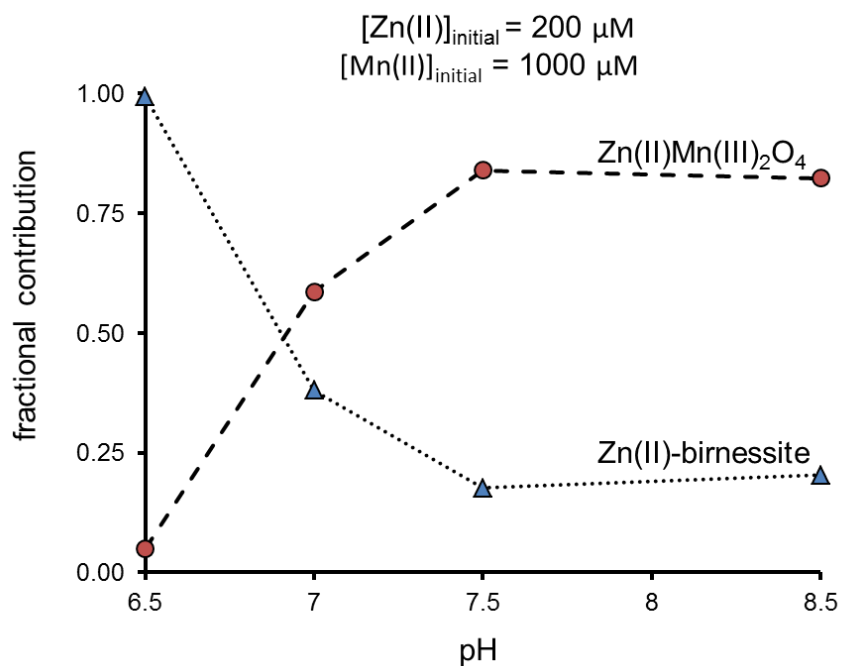


Figure A2.S4. Linear combination fit results

LC fit results for ternary sorption samples reacted with 200 μM $Zn(II)$ and 1000 μM $Mn(II)$, plotted as a function of pH. The values contained in this plot are listed in Table A2.S3. Sample preparation involved reaction of an anoxic 0.1 g L^{-1} birnessite suspension with 200 μM $Zn(II)$ for two days, followed by reaction with 1000 μM $Mn(II)$ for six days.

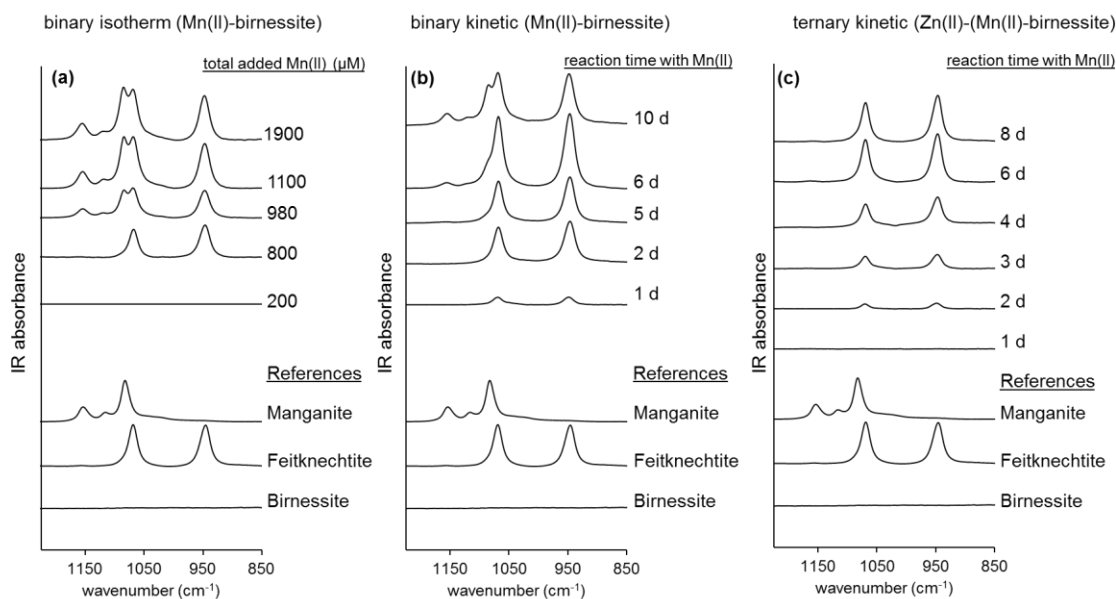


Figure A2.S5. ATR-FTIR data

ATR-FTIR data of the Mn-oxide solids obtained from the binary Mn(II)-birnessite and ternary Zn(II)-Mn(II)-birnessite sorption experiments. Because of the lack of mineralogical transformation at pH 6.5 (see text), only the results of the pH 7.5 experiments are shown. In the binary isotherm experiment (panel a), anoxic birnessite suspensions buffered at pH 7.5 were spiked with Mn(II) at initial concentrations between 50 and 2000 μM Mn(II), and allowed to react for 8 days. The total Mn(II) input is indicated along each spectrum. In the binary kinetic experiment (panel b), 1000 μM Mn(II) was reacted with birnessite in the absence of Zn(II). Changes in Mn-oxide solids were monitored by retrieval of samples at the time points indicated along the spectra. In the ternary kinetic experiment (panel c), 200 μM Zn(II) was reacted with the birnessite substrate for 2 days prior to addition of 1000 μM Mn(II). Sorption times indicated along the spectra represent the time elapsed since addition of Mn(II) at time $t=0$.

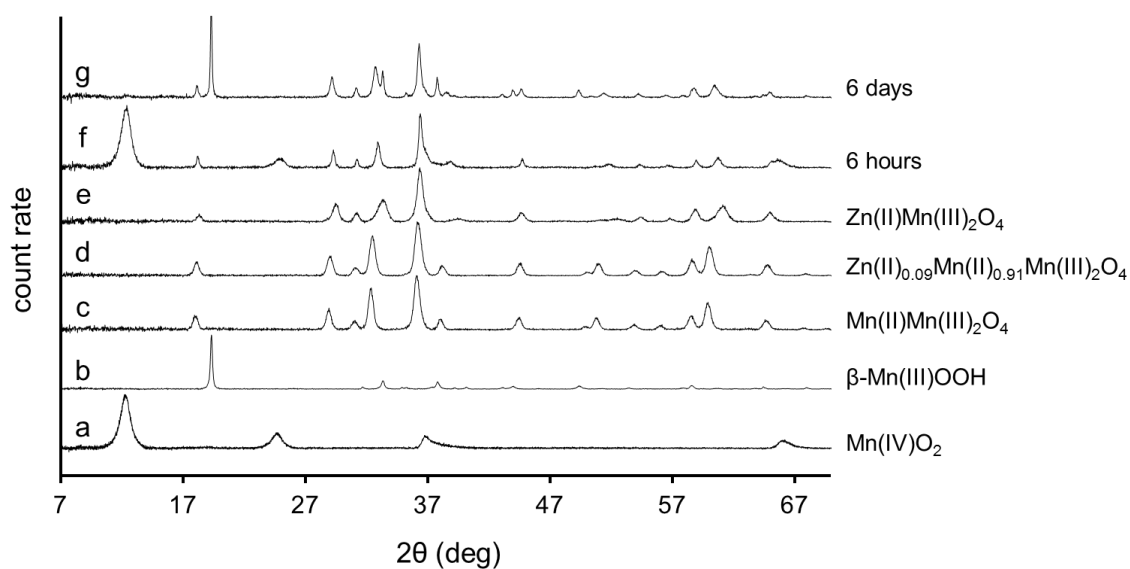


Figure A2.S6. X-ray diffraction data of sorption samples.

Powder XRD patterns of reference Mn oxide samples (a-e) and two ternary pH 7.5 sorption samples that were reacted with $1000\ \mu\text{M Mn(II)}$ for 6 hours (pattern f) and 6 days (pattern g) following initial 2 day equilibration with $200\ \mu\text{M Zn(II)}$.

A2.11. Supporting Information Tables

Table A2.S1: Shell-by-shell fits of Zn XAS data.

Sample ⁱ	Fit 1 (single shells) ^a					Fit 2 (two subshells) ^a				
	atom pair	N ^b	R(Å) ^c	σ ² (Å ²) ^d	χ ² (10 ⁴) ^e	atom pair	N	R (Å)	σ ² (Å ²)	χ ² (10 ⁴)
(a) pH 6.5 200 μM Zn(II)	Zn-O	4.9	2.01	0.012	0.55	^{IV} Zn-O	2.9	1.98	0.006	0.53
						^{VI} Zn-O	1.7	2.12	0.007	
	Zn-Mn	5.8	3.42	0.015		^{IV} Zn-Mn	4.3	3.39	0.013	
						^{VI} Zn-Mn	1.7	3.47	0.010	
(b) pH 6.5 200 μM Zn(II) 1000 μM Mn(II)	Zn-O	4.8	2.01	0.011	2.89	^{IV} Zn-O	3.4	1.99	0.006	1.77
						^{VI} Zn-O	1.7	2.16	0.007	
	Zn-Mn	6.1	3.40	0.015		^{IV} Zn-Mn	5.0	3.39	0.013	
						^{VI} Zn-Mn	1.7	3.49	0.010	
(d) pH 7.5 50 μM Zn(II)	Zn-O	4.8	2.02	0.013	0.20	^{IV} Zn-O	2.7	1.98	0.006	0.12
						^{VI} Zn-O	1.8	2.13	0.007	
	Zn-Mn	5.4	3.44	0.014		^{IV} Zn-Mn	4.1	3.39	0.012	
						^{VI} Zn-Mn	1.8	3.49	0.008	
(e) pH 7.5 200 μM Zn(II)	Zn-O	4.5	2.01	0.011	4.49	^{IV} Zn-O	3.2	1.99	0.006	1.31
						^{VI} Zn-O	1.6	2.16	0.007	
	Zn-Mn	6.5	3.43	0.016		^{IV} Zn-Mn	4.9	3.38	0.013	
						^{VI} Zn-Mn	1.5	3.51	0.006	
(o) pH 8.5 200 μM Zn(II)	Zn-O	4.6	2.00	0.011	2.48	^{IV} Zn-O	3.1	1.97	0.006	1.17
						^{VI} Zn-O	1.6	2.13	0.007	
	Zn-Mn	5.3	3.40	0.015		^{IV} Zn-Mn	4.6	3.36	0.013	
						^{VI} Zn-Mn	1.6	3.47	0.008	
Reference	atom pair	N		R(Å)		σ ² (Å ²)				
ZnMn ₂ O ₄	Zn-O	4.0 (4) ^f		1.97 (2.004) ^f		0.004				
	Zn-Mn	5.6 (6) ^f		3.40 (3.516) ^f		0.004				
Zn(II) in hausmannite ^j	Zn-O	3.8		1.99		0.004				
	Zn-Mn	6.1		3.43		0.004				
ZnO (zincite)	Zn-O	4.3 (4) ^g		1.96 (1.981) ^g		0.006				
ZnCO ₃ (smithsonite)	Zn-O	6.7 (6) ^h		2.09 (2.111) ^h		0.007				

^aFit 1 refers to the single-shell fits described in section 3.1.1, while Fit 2 represents the double-shell fits described in section 3.1.2; ^bN is coordination number, with estimated uncertainty of $\pm 15\%$ for the first shell and $\pm 30\%$ for second shells; ^cR is interatomic distance with estimated uncertainty of ± 0.02 Å for the first shell, and $>\pm 0.05$ Å for longer correlations; ^d σ^2 is the Debye-Waller factor, with estimated uncertainty of ± 0.002 - 0.004 Å²; ^e χ^2 goodness-of-fit parameter, defined in Ressler;¹⁷⁰ ^fCrystallographic data from Nogues and Poix¹³¹ in parentheses; ^gCrystallographic data from Albertson et al.;¹⁷⁵ ^hCrystallographic data from Effenberger et al.¹⁷⁶ in parentheses; ⁱletters in parentheses indicate the corresponding spectrum from Figure S3; ^j The chemical formula of this compound is Zn(II)_{0.09}Mn(II)_{0.91}Mn(III)₂O₄.

Table A2.S2. Numerical results of LC fits from Figure 3.4.

Numerical results of the LC fit results of the pH 7.5 kinetic experiment of the ternary sorption system. The same results are graphed in Figure A2.S2. The fit quality is demonstrated by the overlay of the raw and fitted spectra in Figure 3.4 of the main manuscript.

Time (hours)	Zn(II)-birnessite; endmember (A)	ZnMn ₂ O ₄ ; endmember (B)	Sum of Components (A) + (B)	χ^{2*}
0	1.00	0.00	1.00	-
0.5	0.74	0.27	1.01	68
1.0	0.75	0.28	1.02	55
2.0	0.63	0.37	1.00	56
4.0	0.60	0.47	1.07	102
8.0	0.55	0.47	1.03	62
24	0.53	0.50	1.03	91
144	0.16	0.85	1.01	62

* χ^2 goodness-of-fit parameter, defined in Ressler¹⁷⁰.

Table A2.S3. Numerical results from LC fits presented in Figure A2.S2

binary and ternary sorption samples (0.1 g L ⁻¹ birnessite)				fractional contribution of endmembers			χ^2 *
Corresponding Spectrum (Figure S2)	pH	[Zn(II)] _{initial} (μ M)	[Mn(II)] _{initial} (μ M)	Zn-MnO ₂ endmember (A)	ZnMn ₂ O ₄ endmember (B)	sum (A) + (B)	
A	6.5	200	-	1.00	-	1.00	-
B		200	1000	0.96	0.05	1.01	29
C	7.0	200	1000	0.36	0.60	0.96	100
D	7.5	50	-	1.00	-	1.00	-
E		200	-	1.00	-	1.00	-
F		200	100	0.55	0.42	0.97	72
G		200	200	0.43	0.54	0.97	97
H		200	500	0.29	0.68	0.97	99
I		200	1000	0.16	0.85	1.01	62
J		50	100	0.71	0.30	1.01	142
K		50	500	0.31	0.65	0.96	228
L		50	800	0.30	0.78	1.08	154
M		50	2000	0.23	0.81	1.03	136
N		400	1000	0.26	0.70	0.96	118
O	8.5	200	-	1.00	-	1.00	-
P		200	1000	0.24	0.81	1.05	55

* χ^2 goodness-of-fit parameter, defined in Ressler¹⁷⁰.

Appendix 3

A3.1 Powder XRD of samples obtained from binary and ternary experiments

In Figure A3.S1, powder XRD patterns of reference Mn oxides (patterns a-e), and sorption samples (patterns f-m) obtained from a Ni(II)-Mn(II)-birnessite kinetic experiment (patterns f-j), an Mn(II)-Ni(birnessite) sample (pattern k) and Mn(II)-birnessite samples (patterns l and m) are presented. The sorption samples were derived from experiments conducted at pH 7.5. The kinetic experiment involved 200 μM Ni(II) which was equilibrated with 0.1 g L⁻¹ prior to addition of 1000 μM Mn(II); sorption sample k was obtained by reacting birnessite with 1000 μM Mn(II) for five days prior to exposure to 200 μM Ni(II) for an additional two days.. The final two sorption samples l and m were obtained by reacting 1000 μM Mn(II) with birnessite (in the absence of Ni(II)). Essential differences are evident when examining the Ni(II)-Mn(II)-birnessite kinetic series (Figure A3.S1, patterns f-j) in comparison to the Mn(II)-Ni(II) sample (pattern k) and the Mn(II)-birnessite samples (patterns l and m). As discussed in the main article, addition of Ni(II) does not induce bulk structural change to birnessite (pattern f). Bulk structural change is not evident until one day of reaction with Mn(II) (pattern h), where the signature XRD peak for feitknechtite (between 15 and 25 2θ) is apparent. Comparison of pattern i with pattern l demonstrates the inhibitory effect of Ni(II), where residual birnessite is apparent, indicated by the peak at 12.3 2θ following five days of reaction with Mn(II) in the former as compared to the latter where there are no peaks present that would signify that any of the initial substrate remains after the same amount of reaction time. This inhibitory effect is further demonstrated by comparing pattern j with pattern m, where the former shows evidence for feitknechtite and the latter clearly

demonstrates the presence of manganite (with the major signifying peak just above 25 2θ). Comparison of patterns b, i, j, k and l shows another important difference that is highlighted in Figure A3.S2 and further discussed below.

Figure A3.S2 presents a select portion of samples from those described above with respect to Figure A3.S1. Here we focus on the reference sample feitknechtite (pattern a), the Mn(II)-birnessite sample (pattern b), the Mn(II)-Ni(II)-birnessite sample (pattern c), and the two Ni(II)-Mn(II)-birnessite samples procured from 5 days of reaction Mn(II) (pattern d) and 18 days of reaction with Mn(II) (pattern e). To highlight the differences in these patterns, we have focused on the window above 25 2θ . Comparison of the Mn(II) and Mn(II)-Ni(II)-birnessite samples with the reference feitknechtite shows very similar XRD patterns, whereas the Ni(II)-Mn(II)-birnessite samples exhibit major disruptions, strongly suggesting that Ni(II) has been incorporated into the mineral structure.

A3.2. Time dependent formation of Ni(II) substituted feitknechtite by XAS

The reaction time with Mn(II) is indicated to the right of each spectrum. The XAS data shown in Figure A3.S3 contains the same ternary kinetic series presented in Figure A3.S1, where 200 μM Ni(II) was reacted with 0.1 g L^{-1} birnessite for two days prior to addition of 1000 μM Mn(II). Panel (a) shows the k^3 -weighted χ functions, whereas (b) shows the corresponding radial distribution functions. Shell fits are represented by red dotted lines. Evident in the χ spectra, the initial Ni(II) speciation generated prior to addition of Mn(II) is consistent with sorption complexes at vacancy sites and particle edges as discussed in the main manuscript. Following 10 minutes of reaction with Mn(II), the χ spectrum does not show significant change. Following one day of reaction,

significant changes are apparent in the χ spectrum which continues to evolve over the 18 day timecourse of the experiment.

Examination of the corresponding radial structure functions (RSFs) shows how the Ni(II) speciation changes. Unlike the Ni(II)-birnessite sample presented in the main manuscript (Figure 6, sample g) the EXAFS data in Figure A3.S3 was derived from a sample that included HEPES buffer in the solution matrix. The peak at 2.5 Å present in the RSF for this sample (Figure A3.S3b, spectrum a) shows a difference from the unbuffered sample (Figure 6b, spectrum g); this issue is examined further below (Figure A3.S4). For the kinetic series presented here, peaks present at 1.6 Å, 2.5 Å, and 3.1 Å (each uncorrected for phase shift) are consistent with a mixture of Ni complexes, including ^{TCS}Ni, ^{DES}Ni and ^{DES}Ni; the peak at 3.1 Å may also indicate ^{INC}Ni, but the results for shell fits suggests this complex is not present (further discussed below with respect to Figure 4).

Other than the artefact introduced by the HEPES buffer in the binary sample of Figure A3.S3, the RSF of spectrum a is consistent with Ni sorption to birnessite at vacancies and particle edges. Introduction of Mn(II) does not immediately introduce change to the speciation of Ni, but is evident following one day of reaction (spectrum c). The change in speciation coincides with the formation of a feitknechtite-like phase (Figure A3.S1, pattern h) as discussed above. The RSF shows the evolution of a single peak at a radial distance of ~3.0 Å over the timecourse of the experiment. As discussed in the main text, the results of shell fits (presented in Table S1) points to incorporation of Ni(II).

As mentioned above, Ni(II)-birnessite samples exposed to buffer exhibit differences in the EXAFS data compared to unbuffered experiments. To probe these differences, we compare in Figure A3.S4 Ni(II)-birnessite (spectra a) and Ni(II)-Mn(II)-birnessite (spectra b) in the presence and absence of MES buffer. At pH 7.5, we compare Ni(II)-birnessite (spectra c) in the presence and absence of HEPES buffer. For spectra a-c, the samples were reacted with 200 μM Ni(II) for two days. For spectra b, 1000 μM Mn(II) was subsequently added. An additional sample (d), which was prepared by reacting 0.1 g L⁻¹ birnessite with 200 μM Ni(II) for 20 days and maintained at pH 7.5 with HEPES allowed for direct comparison with long term ternary samples. For samples containing buffer, 20 mM of MES or HEPES was used.

Evident in Figure A3.S4 is that both MES and HEPES have some influence on Ni(II) speciation in these systems. Examination of the Ni(II)-birnessite samples at pH 6.5 and 7.5 shows that, in the absence of buffer, only one Ni-Mn peak (at 3.1 Å uncorrected for phase shift) appears in the RSF which is associated with both ^{DES}Ni (at particle edges) and ^{TCS}Ni (at vacancy sites), but, as discussed in the main text, points to the latter species. In the presence of buffer, a shorter peak appears (at 2.5 Å uncorrected for phase shifts) which most likely corresponds to the “flipped” ^{DES}Ni (at particle edges) observed by Simanova et al.¹⁵⁵ Previous work has shown that the piperazine-ring in HEPES can react with birnessite to generate Mn(III) which, in turn, can influence the architecture of Ni(II) coordination.¹⁵⁵ MES buffer, evidently, has the same effect and may react with birnessite through the morpholino ring. The ternary sorption sample at pH 6.5, however, demonstrates that, in the absence of buffer, Mn(II) influences the speciation of Ni(II) on birnessite. At pH 7.5, comparison of the 2 day and 20 day binary samples shows that the

influence of the buffer is limited over the timecourse of these experiments, with no transformation towards Ni(II)-substituted feiknechtite observed. XRD data (not shown for the 20 day sample) confirms that without Mn(II), no transformation of the substrate occurs (Figures 4 and S1).

A3.3 Supporting Information Figures

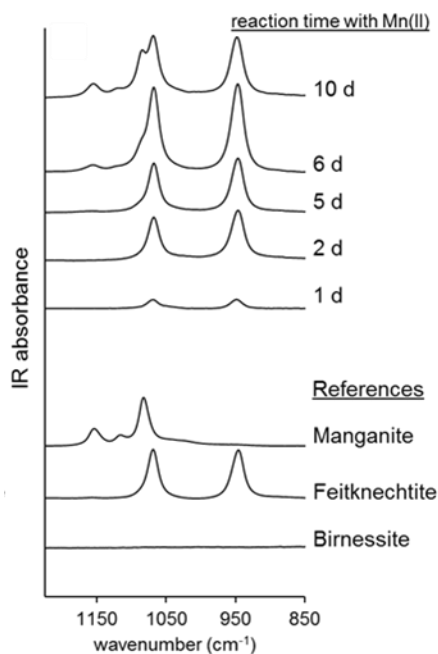


Figure A3.S1. ATR-FTIR data of the Mn-oxide solids procured from the binary Mn(II)-birnessite kinetic experiment at pH 7.5 were 1000 μM Mn(II) was reacted with 0.1 g L⁻¹ birnessite (in the absence of Ni(II)). As mineralogical transformation at pH 6.5 is not observed, the results from that experiment are not shown. The time points to the right of each spectrum indicates the reaction of birnessite with Mn(II).

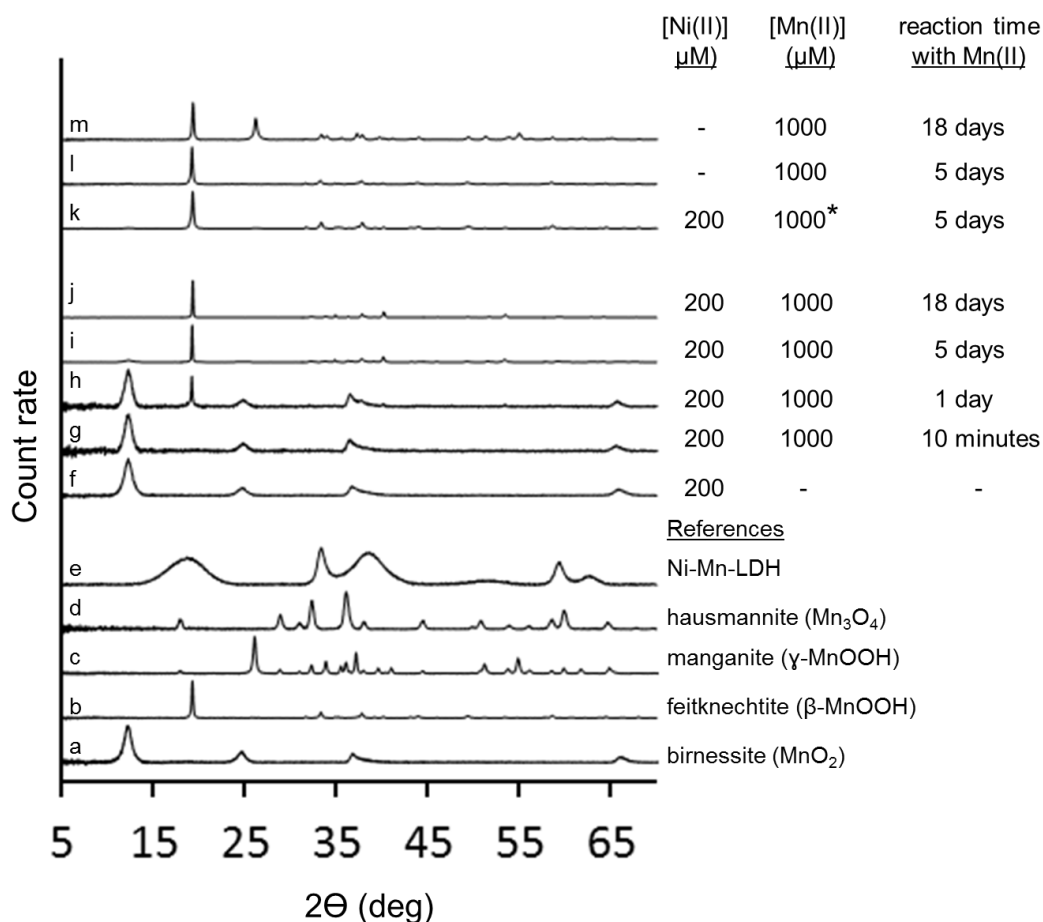


Figure A3.S2. XRD patterns from ternary sorption samples as a function of time.

XRD patterns of metal-oxide reference samples (patterns a-e and sorption samples from kinetic experiments (patterns f-m) reacted under anoxic conditions at pH 7.5. The patterns f-j were derived from a kinetic experiment where 200 μM N(II) was reacted with birnessite for two days followed by reaction with 1000 μM Mn(II) for an additional 18 days. For pattern k, the sample reacted with 1000 μM Mn(II) for five days followed by 200 μM Ni(II) for an additional two days. Patterns l and m were derived from sorption samples reacted with 1000 μM Mn(II) (no Ni(II) present). The reaction conditions are summarized to the right of each pattern, where the asterisk (*) in pattern k indicates that Mn(II) was added first.

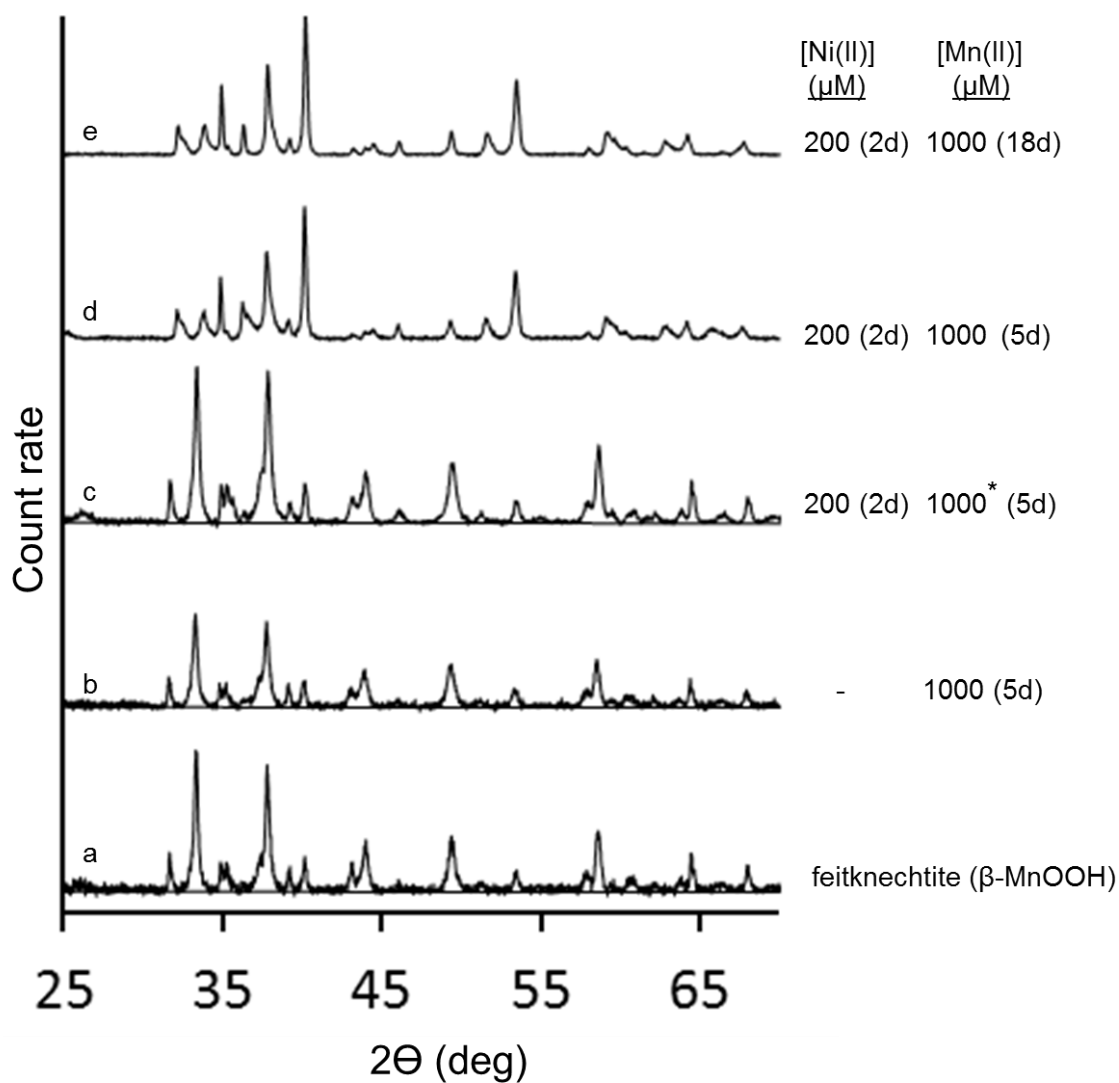


Figure A3.S3. XRD comparison of feitknechtite and Ni(II) substituted feitknechtite.

Zoom-in of select XRD patterns presented in Figures 4.4 and A3.S2 showing the disruption to peaks above 25 2θ for Ni(II)-Mn(II)-birnessite (patterns d and e) compared to reference feitknechtite (pattern a), Mn(II)-birnessite (pattern b) and Mn(II)-Ni(II)-birnessite (pattern c). The reaction conditions are summarized to the right of each pattern, where the asterisk (*) in pattern k indicates that Mn(II) was added first.

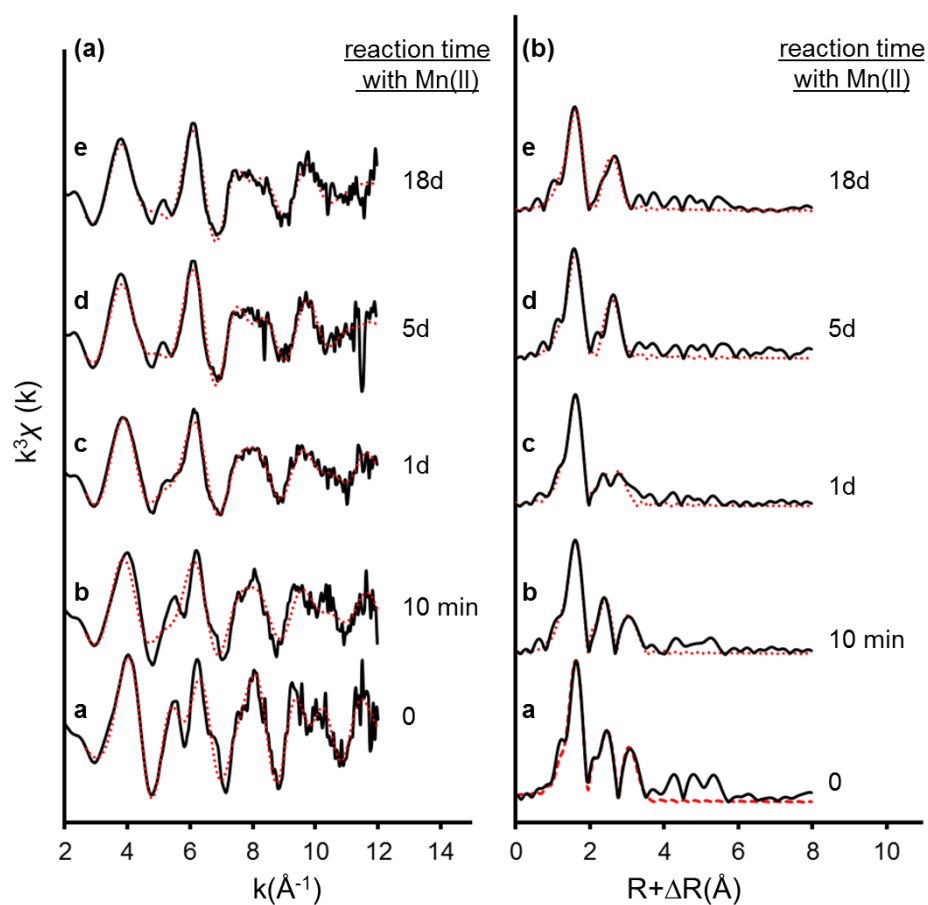


Figure A3.S4. EXAFS data showing evolution of Ni(II) substituted feitknechtite.

Ni K edge EXAFS data of anoxic birnessite (0.1 g L^{-1}) sorption samples reacted at pH 7.5 with $200 \text{ }\mu\text{M}$ Ni(II) and $1000 \text{ }\mu\text{M}$ Mn(II) for up to 18 days. (a) k^3 -weighted χ functions.

Raw spectra are shown in black, whereas shell fits—further described in the text—are represented by red dotted lines. (b) Corresponding radial distribution functions.

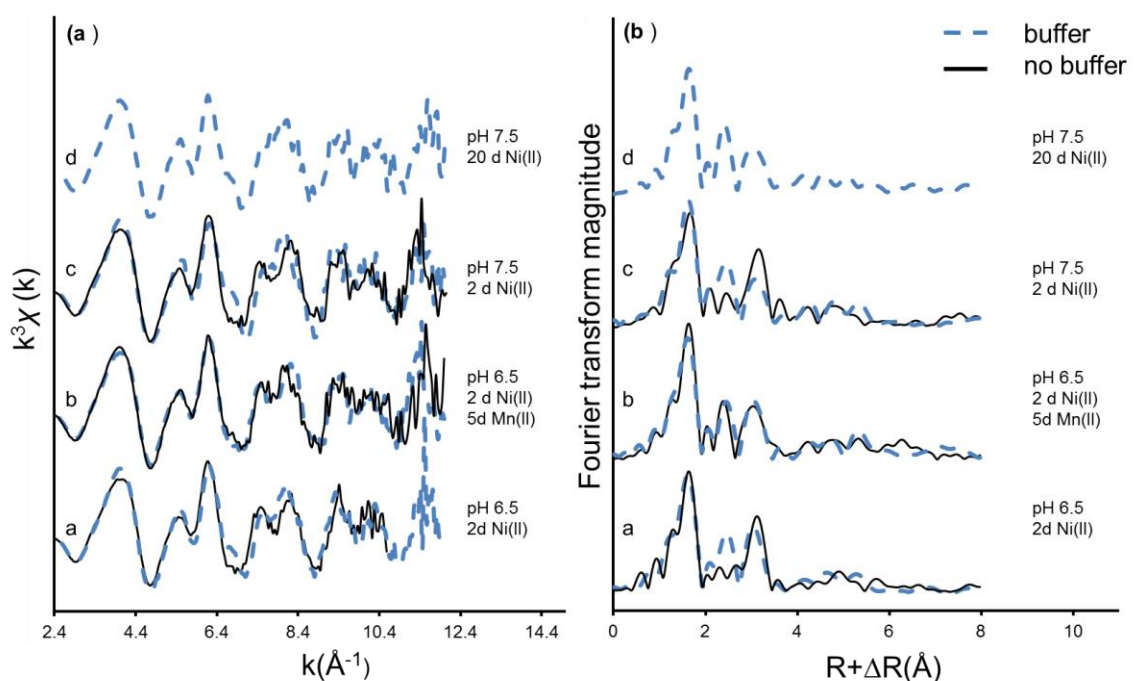


Figure A3.S5. EXAFS data showing impact of buffer in these systems.

Ni K edge EXAFS data of anoxic birnessite (0.1 g L^{-1}) sorption samples reacted at pH 6.5, spectra a, and 7.5, spectra c and d, with $200 \text{ }\mu\text{M}$ Ni(II) in the presence (black lines) and absence (blue dashed line) of buffer for 2 or 20 days. Additional ternary samples at pH 6.5, spectra b were reacted with $200 \text{ }\mu\text{M}$ for two days followed by reaction with $1000 \text{ }\mu\text{M}$ Mn(II) for five more days. (a) k^3 -weighted χ functions. (b) Corresponding radial distribution functions. Reaction conditions are summarized to the right of each spectra.

For pH 6.5 and pH 7.5 the buffers MES and HEPES were used, respectively.

A3.4 Supporting Information Tables

Table A3.S1: Shell fit results of Ni XAS data from sorption products and references.

sample ^a					atom pair	N ^b	R(Å) ^c	σ ² (Å)	χ ² (10 ⁴) ^e
pH	[Ni] (μM)	[Mn] (μM)	Δt	buffer					
6.5	200	-	-	-	Ni-O	6.0	2.06	0.006	0.33
					Ni-Mn _A	-	-	-	
					Ni-Mn _B	6.0	3.49	0.009	
6.5	200	-	-	MES	Ni-O	6.0	2.04	0.006	5.05
					Ni-Mn _A	2.3	2.87	0.007	
					Ni-Mn _B	5.3	3.47	0.008	
6.5	200	1000	5 d	-	Ni-O	6.0	2.04	0.005	3.60
					Ni-Mn _A	2.0	2.85	0.007	
					Ni-Mn _B	6.0	3.46	0.009	
6.5	200	1000	5 d	MES	Ni-O	6.0	2.04	0.005	0.34
					Ni-Mn _A	2.0	2.87	0.005	
					Ni-Mn _B	5.0	3.47	0.008	
6.5	200	1000	18 d	MES	Ni-O	6.0	2.04	0.005	0.63
					Ni-Mn _A	2.0	2.86	0.006	
					Ni-Mn _B	4.2	3.46	0.007	
7.5	200	-	-	-	Ni-O	6.0	2.06	0.006	8.84
					Ni-Mn _A	-	-	-	
					Ni-Mn _B	5.5	3.49	0.007	
7.5	200	-	-	HEPES	Ni-O	6.0	2.05	0.005	1.72
					Ni-Mn _A	4.6	2.87	0.011	
					Ni-Mn _B	5.0	3.49	0.009	
7.5	200 (20 d)	-	-	HEPES	Ni-O	6.0	2.04	0.005	0.26
					Ni-Mn _A	2.0	2.86	0.005	
					Ni-Mn _B	6.0	3.46	0.010	
7.5	200	1000	10 min	HEPES	Ni-O	6.0	2.04	0.007	2.54
					Ni-Mn _A	2.0	2.85	0.008	
					Ni-Mn _B	5.6	3.47	0.012	
7.5	200	1000	1 d	HEPES	Ni-O	6.0	2.05	0.007	2.82
					Ni-Mn _A	5.4	2.94	0.016	
					Ni-Mn _B	-	-	-	
					Ni-Mn _C	2	3.11	0.006	
7.5	200	1000	5 d	HEPES	Ni-O	6.0	2.05	0.007	4.30
					Ni-Mn _A	-	-	-	
					Ni-Mn _B	-	-	-	
					Ni-Mn _C	4.6	3.04	0.011	
7.5	200	1000	18 d	HEPES	Ni-O	6.0	2.05	0.008	1.72
					Ni-Mn _A	-	-	-	
					Ni-Mn _B	-	-	-	
					Ni-Mn _C	6.0	3.04	0.014	
7.5	200	1000 [*]	5 d	HEPES	Ni-O	6	2.06	0.005	2.54
					Ni-Mn _A	-	-	-	
					Ni-Mn _B	-	-	-	
					Ni-Mn _C	6	3.05	0.013	
reference ^f									
α-Ni(OH) ₂			Ni-O 5.8 2.04 0.006 7.17						

^aFitting routine is further described in the Materials and Methods section of the main article. In brief, the amplitude reduction factor was fixed to 0.8 (determined from the fit of Ni-O in α -Ni(OH)₂), the coordination number (N) was fixed to 6 for all sorption samples, and constrained between 2 and 6 for all Ni-Mn shells.

^bN is coordination number, with estimated uncertainty of $\pm 20\%$ for the first shell and $\pm 30\%$ for second shells; ^cR is interatomic distance with estimated uncertainty of $\pm 0.01 \text{ \AA}$ for the first shell, and $> \pm 0.02 \text{ \AA}$ for longer correlations.

^d σ^2 is the Debye-Waller factor, with estimated uncertainty of $\pm 0.003 \text{ \AA}^2$ for Ni(II)-birnessite and pH 6.5 ternary samples. The estimated uncertainty is $\pm 0.006 \text{ \AA}^2$ for pH 7.5 ternary sorption samples reacted for 1 - 18 days.

^ereduced χ^2 goodness-of-fit parameter, defined in Ressler¹⁷⁰

^freference XAS spectrum generously provided by Scheinost and Sparks¹⁵¹.